Eur. Phys. J. C manuscript No.
(will be inserted by the editor)

Towards an Understanding of the Correlations in Jet Substructure

Report of BOOST2013, hosted by the University of Arizona, 12^{th}-16^{th} of August 2013.

D. Adams[1], A. Arce[2], L. Asquith[3], M. Backovic[4], T. Barillari[5], P. Berta[6], D. Bertolini[2], A. Buckley[8], J. Butterworth[9], R. C. Camacho Toro[10], J. Caudron[9], Y.-T. Chien[11], J. Cogan[12], B. Cooper[9], D. Curtin[17], C. Debenedetti[18], J. Dolen[9], M. Eklund[22], S. El Hedri[22], S. D. Ellis[22], T. Embry[22], D. Ferencek[23], J. Ferrando[24], S. Fleischmann[16], M. Freytsis[25], M. Giulini[21], Z. Han[27], D. Hare[4], P. Harris[4], A. Hinzmann[4], R. Hoing[4], A. Hornig[22], M. Jankowiak[4], K. Johns[28], G. Kasieczka[23], T. Knight[24], G. Kasieczka[29], R. Kogler[30], W. Lampl[4], A. J. Larkoski[4], C. Lee[31], R. Leone[31], P. Loch[31], D. Lopez Mateos[27], H. K. Lou[27], M. Low[27], P. Maksimovic[32], I. Marchesini[32], S. Marzani[32], L. Masetti[33], R. McCarthy[32], S. Menke[32], D. W. Miller[35], K. Mishra[36], B. Nachman[32], P. Nef[4], F. T. O'Grady[24], A. Ovcharova[23], A. Picazio[37], C. Pollard[38], B. Potter Landua[29], C. Potter[29], S. Rappoccio[39], J. Rojo[48], J. Rutherfoord[40], G. P. Salam[10,11], J. Schabinger[23], A. Schwartzman[4], M. D. Schwartz[27], B. Shuve[43], P. Sinervo[44], D. Soper[45], D. E. Sosa Corral[45], M. Spannowsky[32], E. Strauss[34], M. Swiatlowski[4], J. Thaler[34], C. Thomas[34], E. Thompson[1], N. V. Tran[36], J. Tseng[36], E. Usai[36], L. Valery[36], J. Veatch[23], M. Vos[23], W. Waalewijn[4], and C. Young[47]

[1] *Columbia University, Nevis Laboratory, Irvington, NY 10533, USA*
[2] *Duke University, Durham, NC 27708, USA*
[3] *Argonne National Laboratory, Lemont, IL 60439, USA*
[4] *SLAC National Accelerator Laboratory, Menlo Park, CA 94025, USA*
[5] *Deutsches Elektronen-Synchrotron, DESY, D-15738 Zeuthen, Germany*
[6] *Cornell University, Ithaca, NY 14853, USA*
[7] *Lund University, Lund, SE 22100, Sweden*
[8] *University of Edinburgh, EH9 3JZ, UK*
[9] *University College London, WC1E 6BT, UK*
[10] *LPTHE, UPMC Univ. Paris 6 and CNRS UMR 7589, Paris, France*
[11] *CERN, CH-1211 Geneva 23, Switzerland*
[12] *CAFPE and U. of Granada, Granada, E-18071, Spain*
[13] *McGill University, Montreal, Quebec H3A 2T8, Canada*
[14] *Iowa State University, Ames, Iowa 50011, USA*
[15] *Rutgers University, Piscataway, NJ 08854, USA*
[16] *Bergische Universitaet Wuppertal, Wuppertal, D-42097, Germany*
[17] *YITP, Stony Brook University, Stony Brook, NY 11794-3840, USA*
[18] *University of Manchester, Manchester, M13 9PL, UK*
[19] *UNESP - Universidade Estadual Paulista, Sao Paulo, 01140-070, Brazil*
[20] *INFN and University of Naples, IT80216, Italy*
[21] *University of Geneva, CH-1211 Geneva 4, Switzerland*
[22] *University of Washington, Seattle, WA 98195, USA*
[23] *Instituto de Física Corpuscular, IFIC/CSIC-UVEG, E-46071 Valencia, Spain*
[24] *University of Glasgow, Glasgow, G12 8QQ, UK*
[25] *Berkeley National Laboratory, University of California, Berkeley, CA 94720, USA*
[26] *Universidad de Buenos Aires, AR-1428, Argentina*
[27] *Harvard University, Cambridge, MA 02138, USA*
[28] *Weizmann Institute, 76100 Rehovot, Israel*
[29] *Universitaet Hamburg, DE-22761, Germany*
[30] *Universitaet Heidelberg, DE-69117, Germany*
[31] *University of Arizona, Tucson, AZ 85719, USA*
[32] *IPPP, University of Durham, Durham, DH1 3LE, UK*
[33] *Universitaet Mainz, DE 55099, Germany*
[34] *MIT, Cambridge, MA 02139, USA*
[35] *University of Chicago, IL 60637, USA*
[36] *Fermi National Accelerator Laboratory, Batavia, IL 60510, USA*
[37] *Indiana University, Bloomington, IN 47405, USA*
[38] *University of California, Davis, CA 95616, USA*
[39] *Johns Hopkins University, Baltimore, MD 21218, USA*
[40] *INFN and University of Pisa, Pisa, IT-56127, Italy*
[41] *Texas A & M University, College Station, TX 77843, USA*
[42] *INFN and University of Calabria, Rende, IT-87036, Italy*
[43] *Brown University, Richmond, RI 02912, USA*
[44] *Yale University, New Haven, CT 06511, USA*
[45] *CEA Saclay, Gif-sur-Yvette, FR-91191, France*
[46] *University of Illinois, Chicago, IL 60607, USA*
[47] *University of California, Berkeley, CA 94720, USA*

Abstract Abstract for BOOST2013 report

Keywords boosted objects · jet substructure · beyond-the-Standard-Model physics searches · Large Hadron Collider

1 Introduction

The characteristic feature of collisions at the LHC is a center-of-mass energy, 7 TeV in 2010 and 2011, of 8 TeV in 2012, and near 14 TeV with the start of the second phase of operation in 2015, that is large compared to even the heaviest of the known particles. Thus these particles (and also previously unknown ones) will often be produced at the LHC with substantial boosts. As a result, when decaying hadronically, these particles will not be observed as multiple jets in the detector, but rather as a single hadronic jet with distinctive internal substructure. This realization has led to a new era of sophistication in our understanding of both standard QCD jets and jets containing the decay of a heavy particle, with an array of new jet observables and detection techniques introduced and studies. To allow the efficient sharing of results from these jet substructure studies a series of BOOST Workshops have been held on a yearly basis: SLAC (2009, [?]), Oxford University (2010, [?]), Princeton University University (2011, [?]), IFIC Valencia (2012 [?]), University of Arizona (2013 [?]), and, most recently, University College London (2014 [?]). After each of these meetings Working Groups have functioned during the following year to generate reports highlighting the most interesting new results, including studies of ever maturing details. Previous BOOST reports can be found at [?,?,?].

The following report from BOOST 2013 thus views the study and implementation of jet substructure techniques as a fairly mature field. The report attempts to focus on the question of the correlations between the plethora of observables that have been developed and employed, and their dependence on the underlying jet parameters, especially the jet radius R and jet p_T. The report is organized as follows: NEED TO GENERATE AN OUTLINE OF THE REPORT - ESPECIALLY AS I UNDERSTAND IT MYSELF.

2 Monte Carlo Samples and Event Selection

2.1 Quark/gluon and W tagging

Samples were generated at $\sqrt{s} = 8$ TeV for QCD dijets, and for W^+W^- pairs produced in the decay of a (pseudo) scalar resonance and decaying hadronically. The QCD events were split into subsamples of gg and $q\bar{q}$ events, allowing for tests of discrimination of hadronic W bosons, quarks, and gluons.

Individual gg and $q\bar{q}$ samples were produced at leading order (LO) using MadGraph5, while W^+W^- samples were generated using the JHU Generator to allow for separation of longitudinal and transverse polarizations. Both were generated using CTEQ6L1 PDFs[**REF**]. The samples were produced in exclusive p_T bins of width 100 GeV, with the slicing parameter chosen to be the p_T of any final state parton or W at LO. At the parton-level the p_T bins investigated were 300-400 GeV, 500-600 GeV and 1.0-1.1 TeV. Since no matching was performed, a cut on any parton was equivalent. The samples were then all showered through Pythia8 (version 8.176) using the default tune 4C.

2.2 Top tagging

Samples were generated at $\sqrt{s} = 14$ TeV. Standard Model dijet and top pair samples were produced with Sherpa 2.0.0[**REF**], with matrix elements of up to two extra partons matched to the shower. The top samples included only hadronic decays and were generated in exclusive p_T bins of width 100 GeV, taking as slicing parameter the maximum of the top/anti-top p_T. The QCD samples were generated with a cut on the leading parton-level jet p_T, where parton-level jets are clustered with the anti-k_t algorithm and jet radii of $R = 0.4$, 0.8, 1.2. The matching scale is selected to be $Q_{\text{cut}} = 40, 60, 80$ GeV for the $p_{T\,\text{min}} = 600, 1000$, and 1500 GeV bins, respectively.

The analysis again relies on FastJet 3.0.3 for jet clustering and calculation of jet substructure observables, and an upper and lower p_T cut are applied to each sample to ensure similar p_T spectra in each bin. The bins in leading jet p_T that are investigated for top tagging are 600-700 GeV, 1-1.1 TeV, and 1.5-1.6 TeV. **ED: What jet algorithm is used to define the p_T bins?**

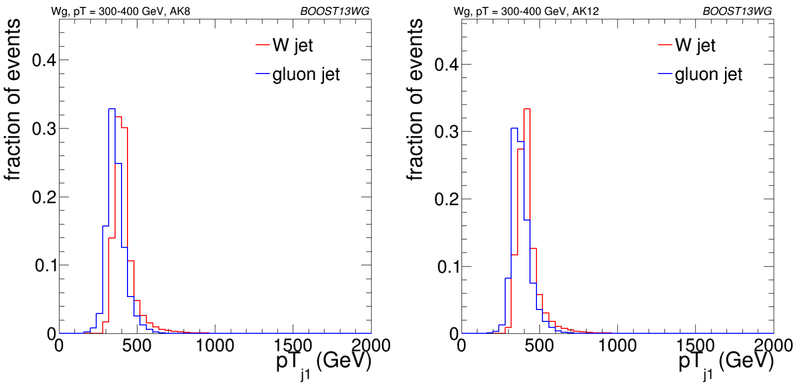

(a) anti-k_{T} R=0.8 (b) anti-k_{T} R=1.2

Fig. 1 Comparisons of the leading jet p_T spectrum of the gg background to the WW signal in the p_T 300-400 GeV parton p_T slice using the different anti-k_{T} jet distance parameters explored in this p_T bin. These distributions are formed prior to the 300-400 GeV leading jet p_T requirement.

3 Jet Algorithms and Substructure Observables

In this section, we define the jet algorithms and observables used in our analysis. Over the course of our study, we considered a larger set of observables, but for the final analysis, we eliminated redundant observables for presentation purposes. In Sections 3.1, 3.2, 3.3 and 3.4 we first describe the various jet algorithms, groomers, taggers and other substructure variables used in these studies, and then in Section 3.5 list which observables are considered in each section of this report, and the exact settings of the parameters used.

3.1 Jet Clustering Algorithms

Jet clustering: Jets were clustered using sequential jet clustering algorithms[**REF**]. Final state particles i, j are assigned a mutual distance d_{ij} and a distance to the beam, $d_{i\mathrm{B}}$. The particle pair with smallest d_{ij} are recombined and the algorithm repeated until the smallest distance is instead the distance to the beam, $d_{i\mathrm{B}}$, in which case i is set aside and labelled as a jet. The distance metrics are defined as

$$d_{ij} = \min(p_{Ti}^{2\gamma}, p_{Tj}^{2\gamma})\,\frac{\Delta R_{ij}^2}{R^2}, \qquad (1)$$

$$d_{i\mathrm{B}} = p_{Ti}^{2\gamma}, \qquad (2)$$

where $\Delta R_{ij}^2 = (\Delta\eta)^2 + (\Delta\phi)^2$. In this analysis, we use the anti-k_t algorithm ($\gamma = -1$), the Cambridge/Aachen (C/A) algorithm ($\gamma = 0$)[**REF**], and the k_t algorithm ($\gamma = 1$)[**REF**], each of which has varying sensitivity to soft radiation in defining the jet.

Qjets: We also perform non-deterministic jet clustering[**REF**]. Instead of always clustering the particle pair with smallest distance d_{ij}, the pair selected for combination is chosen probabilistically according to a measure

$$P_{ij} \propto e^{-\alpha\,(d_{ij} - d_{\min})/d_{\min}}, \qquad (3)$$

where $d_{\min}$ is the minimum distance for the usual jet clustering algorithm at a particular step. This leads to a different cluster sequence for the jet each time the Qjet algorithm is used, and consequently different substructure properties. The parameter α is called the rigidity and is used to control how sharply peaked the probability distribution is around the usual, deterministic value. The Qjets method uses statistical analysis of the resulting distributions to extract more information from the jet than can be found in the usual cluster sequence. We use $\alpha = 0.1$ and 25 trees per event for all the studies presented here.

3.2 Jet Grooming Algorithms

Pruning: Given a jet, re-cluster the constituents using the C/A algorithm. At each step, proceed with the merger as usual unless both

$$\frac{\min(p_{Ti}, p_{Tj})}{p_{Tij}} < z_{\mathrm{cut}} \text{ and } \Delta R_{ij} > \frac{2m_j}{p_{Tj}} R_{\mathrm{cut}}, \qquad (4)$$

in which case the merger is vetoed and the softer branch discarded. The default parameters used for pruning[**REF**]in this study are $z_{\mathrm{cut}} = 0.1$ and $R_{\mathrm{cut}} = 0.5$. One advantage of pruning is that the thresholds used to veto soft, wide-angle radiation scale with the jet kinematics, and so the algorithm is expected to perform comparably over a wide range of momenta.

Trimming: Given a jet, re-cluster the constituents into subjets of radius $R_{\rm trim}$ with the k_t algorithm. Discard all subjets i with

$$p_{Ti} < f_{\rm cut}\, p_{TJ}. \tag{5}$$

The default parameters used for trimming[**REF**]in this study are $R_{\rm trim} = 0.2$ and $f_{\rm cut} = 0.03$.

Filtering:[**REF**] Given a jet, re-cluster the constituents into subjets of radius $R_{\rm filt}$ with the C/A algorithm. Redefine the jet to consist of only the hardest N subjets, where N is determined by the final state topology and is typically one more than the number of hard prongs in the resonance decay (to include the leading final-state gluon emission). **ED: Do we actually use filtering as described here anywhere?**

Soft drop: Given a jet, re-cluster all of the constituents using the C/A algorithm. Iteratively undo the last stage of the C/A clustering from j into subjets j_1, j_2. If

$$\frac{\min(p_{T1}, p_{T2})}{p_{T1} + p_{T2}} < z_{\rm cut} \left(\frac{\Delta R_{12}}{R} \right)^{\beta}, \tag{6}$$

discard the softer subjet and repeat. Otherwise, take j to be the final soft-drop jet[**REF**]. Soft drop has two input parameters, the angular exponent β and the soft-drop scale $z_{\rm cut}$, with default value $z_{\rm cut} = 0.1$. **ED: Soft-drop actually functions as a tagger when $\beta = -1$**

3.3 Jet Tagging Algorithms

Modified Mass Drop Tagger: Given a jet, re-cluster all of the constituents using the C/A algorithm. Iteratively undo the last stage of the C/A clustering from j into subjets j_1, j_2 with $m_{j_1} > m_{j_2}$. If either

$$m_{j_1} > \mu\, m_j \;\; \text{or} \;\; \frac{\min(p_{T1}^2, p_{T2}^2)}{m_j^2}\, \Delta R_{12}^2 < y_{\rm cut}, \tag{7}$$

then discard the branch with the smaller transverse mass $m_T = \sqrt{m_i^2 + p_{Ti}^2}$, and re-define j as the branch with the larger transverse mass. Otherwise, the jet is tagged. If de-clustering continues until only one branch remains, the jet is untagged. In this study we use by default $\mu = 1.0$ and $y_{\rm cut} = 0.1$.

Johns Hopkins Tagger: Re-cluster the jet using the C/A algorithm. The jet is iteratively de-clustered, and at each step the softer prong is discarded if its $p_{\rm T}$ is less than $\delta_p\, p_{\rm T\,jet}$. This continues until both prongs are harder than the $p_{\rm T}$ threshold, both prongs are softer than the $p_{\rm T}$ threshold, or if they are too close ($|\Delta\eta_{ij}| + |\Delta\phi_{ij}| < \delta_R$); the jet is rejected if either of the latter conditions apply. If both are harder than the $p_{\rm T}$ threshold, the same procedure is applied to each: this results in 2, 3, or 4 subjets. If there exist 3 or 4 subjets, then the jet is accepted: the top candidate is the sum of the subjets, and W candidate is the pair of subjets closest to the W mass. The output of the tagger is m_t, m_W, and $\theta_{\rm h}$, a helicity angle defined as the angle, measured in the rest frame of the W candidate, between the top direction and one of the W decay products. The two free input parameters of the John Hopkins tagger in this study are δ_p and δ_R, defined above.

HEPTopTagger: Re-cluster the jet using the C/A algorithm. The jet is iteratively de-clustered, and at each step the softer prong is discarded if $m_1/m_{12} > \mu$ (there is not a significant mass drop). Otherwise, both prongs are kept. This continues until a prong has a mass $m_i < m$, at which point it is added to the list of subjets. Filter the jet using $R_{\rm filt} = \min(0.3, \Delta R_{ij})$, keeping the five hardest subjets (where ΔR_{ij} is the distance between the two hardest subjets). Select the three subjets whose invariant mass is closest to m_t. The output of the tagger is m_t, m_W, and $\theta_{\rm h}$, a helicity angle defined as the angle, measured in the rest frame of the W candidate, between the top direction and one of the W decay products. The two free input parameters of the HEPTopTagger in this study are m and μ, defined above.

Top Tagging with Pruning: For comparison with the other top taggers, we add a W reconstruction step to the trimming algorithm described above. A W candidate is found as follows: if there are two subjets, the highest-mass subjet is the W candidate (because the W prongs end up clustered in the same subjet); if there are three subjets, the two subjets with the smallest invariant mass comprise the W candidate. In the case of only one subjet, no W is reconstructed.

Top Tagging with Trimming: For comparison with the other top taggers, we add a W reconstruction step to the trimming algorithm described above. A W candidate is found as follows: if there are two subjets, the highest-mass subjet is the W candidate (because the W prongs end up clustered in the same subjet); if there are three subjets, the two subjets with the smallest invariant mass comprise the W candidate. In the case of only one subjet, no W is reconstructed.

3.4 Other Jet Substructure Observables

Qjet mass volatility: As described above, Qjet algorithms re-cluster the same jet non-deterministically to obtain a collection of interpretations of the jet. For each jet interpretation, the pruned jet mass is computed with the default pruning parameters. The mass volatility, Γ_{Qjet}, is defined as

$$\Gamma_{\text{Qjet}} = \frac{\sqrt{\langle m_J^2\rangle - \langle m_J\rangle^2}}{\langle m_J\rangle}, \tag{8}$$

where averages are computed over the Qjet interpretations.

N-subjettiness: N-subjettiness[**REF**]quantifies how well the radiation in the jet is aligned along N directions. To compute N-subjettiness, $\tau_N^{(\beta)}$, one must first identify N axes within the jet. Then,

$$\tau_N = \frac{1}{d_0}\sum_i p_{Ti}\min\left(\Delta R_{1i}^{\beta},\ldots,\Delta R_{Ni}^{\beta}\right), \tag{9}$$

where distances are between particles i in the jet and the axes,

$$d_0 = \sum_i p_{Ti}\, R^{\beta} \tag{10}$$

and R is the jet clustering radius. The exponent β is a free parameter. There is also some choice in how the axes used to compute N-subjettiness are determined. The optimal configuration of axes is the one that minimizes N-subjettiness; recently, it was shown that the "winner-takes-all" axes can be easily computed and have superior performance compared to other minimization techniques[**REF**]. **ED: Do we use WTA? Otherwise why do we mention this?**

A more powerful discriminant is often the ratio,

$$\tau_{N,N-1} \equiv \frac{\tau_N}{\tau_{N-1}}. \tag{11}$$

While this is not an infrared-collinear (IRC) safe observable, it is calculable[**REF**]and can be made IRC safe with a loose lower cut on τ_{N-1}.

Energy correlation functions: The transverse momentum version of the energy correlation functions are defined as[**REF**]:

$$\text{ECF}(N,\beta) = \sum_{i_1<i_2<\ldots<i_N\in j}\left(\prod_{a=1}^{N} p_{Ti_a}\right)\left(\prod_{b=1}^{N-1}\prod_{c=b+1}^{N}\Delta R_{i_b i_c}\right)^{\beta} \tag{12}$$

where i is a particle inside the jet. It is preferable to work in terms of dimensionless quantities, particularly the energy correlation function double ratio:

$$C_N^{(\beta)} = \frac{\text{ECF}(N+1,\beta)\,\text{ECF}(N-1,\beta)}{\text{ECF}(N,\beta)^2}. \tag{13}$$

This observable measures higher-order radiation from leading-order substructure.

3.5 Observables for Each Analysis

Quark/gluon discrimination:

- The ungroomed jet mass, m.
- 1-subjettiness, τ_1^{β} with $\beta = 1$, 2. The N-subjettiness axes are computed using one-pass k_t axis optimization.
- 1-point energy correlation functions, $C_1^{(\beta)}$ with $\beta = 1$, 2.
- The pruned Qjet mass volatility, Γ_{Qjet}.
- The number of constituents (N_{constits}).

W vs. gluon discrimination:

- The ungroomed, trimmed (m_{trim}), and pruned (m_{prun}) jet masses.
- The mass output from the modified mass drop tagger (m_{mmdt}).
- The soft drop mass with $\beta = -1$, 2 (m_{sd}).
- 2-point energy correlation function ratio $C_2^{\beta=1}$ (we also studied $\beta = 2$ but did not show its results because it showed poor discrimination power).
- N-subjettiness ratio τ_2/τ_1 with $\beta = 1$ ($\tau_{21}^{\beta=1}$) and with axes computed using one-pass k_t axis optimization (we also studied $\beta = 2$ but did not show its results because it showed poor discrimination power).
- The pruned Qjet mass volatility.

Top vs. QCD discrimination:

- The ungroomed jet mass.
- The HEPTopTagger and the Johns Hopkins tagger.
- Trimming and grooming supplemented with W candidate identification.
- N-subjettiness ratios τ_2/τ_1 and τ_3/τ_2 with $\beta = 1$ and the "winner-takes-all" axes.
- 2-point energy correlation function ratios $C_2^{\beta=1}$ and $C_3^{\beta=1}$.
- The pruned Qjet mass volatility, Γ_{Qjet}.

4 Multivariate Analysis Techniques

Multivariate techniques are used to combine variables into an optimal discriminant. In all cases variables are combined using a boosted decision tree (BDT) as implemented in the TMVA package [**?**]. We use the BDT implementation including gradient boost. An example of the BDT settings are as follows:

- NTrees=1000
- BoostType=Grad
- Shrinkage=0.1
- UseBaggedGrad=F
- nCuts=10000
- MaxDepth=3

- UseYesNoLeaf=F
- nEventsMin=200

Exact parameter values are chosen to best reduce the effect of overtraining.

5 Quark-Gluon Discrimination

In this section, we examine the differences between quark- and gluon-initiated jets in terms of substructure variables, and to determine to what extent these variables are correlated. Along the way, we provide some theoretical understanding of these observables and their performance. The motivation for these studies comes not only from the desire to "tag" a jet as originating from a quark or gluon, but also to improve our understanding of the quark and gluon components of the QCD backgrounds relative to boosted resonances. While recent studies have suggested that quark/gluon tagging efficiencies depend highly on the Monte Carlo generator used, we are more interested in understanding the scaling performance with p_T and R, and the correlations between observables, which are expected to be treated consistently within a single shower scheme.

5.1 Methodology

These studies use the qq and gg MC samples, described previously in Section 2. The showered events were clustered with FastJet 3.03[**REF**]using the anti-k_{T} algorithm[**REF**]with jet radii of $R = 0.4$, 0.8, 1.2. In both signal and background, an upper and lower cut on the leading jet p_T is applied after showering/clustering, to ensure similar p_T spectra for signal and background in each p_T bin. The bins in leading jet p_T that are investigated in the W-tagging and q/g tagging studies are 300-400 GeV, 500-600 GeV, 1.0-1.1 TeV. The distribution of the leading jet p_T for the gg and WW samples in the 300-400 GeV parton p_T slice prior to the requirement on the leading jet p_T is shown in Figure 1, for the R=0.8 and R=1.2 anti-k_{T} jet radii considered in this p_T slice. Figures 2 and 3 show the equivalent leading jet p_T distributions for the jet radii considered in the 500-600 GeV and 1.0 - 1.1 TeV slices respectively. Various jet grooming approaches are applied to the jets, as described in Section 3.4. Only leading and subleading jets in each sample are used.

Figure 4 shows a comparison of the p_T and η distributions of the quark and gluon samples with $p_T = 500 - 600$ GeV. The differences in the p_T distributions can be attributed to different out-of-cone radiation patterns for quark and gluons; these differences become smaller as the R parameter is increased. The different η distributions are related to the different parton distribution functions initiating qq and gg production. The qualitative features of the η distributions do not change as the R parameter is changed. As the p_T increases, the η distributions peak more strongly near zero, as the probability peaks for processes initiated by partons of comparable energy. In our analysis, we make a narrow window cut of 100 GeV in p_T after showering, and so the effects of the different q/g p_T spectra on our analysis is suppressed. (**ED: check**)

5.2 Single Variable Discrimination

Figure 5 shows the mass of jets in the quark and gluon samples when using different groomers. Jets built with the anti-k_{T} algorithm with R=0.8 and with $p_T = 500 - 650$ GeV are used (**BS:Check pT bins in this section!**). Qualitatively, the application of grooming shifts the mass distributions towards lower values as expected. No clear gain in discrimination can be seen, and for certain grooming parameters, such as the use of soft drop with $\beta = -1$ a clear loss in discrimination power is observed; this is because the soft-drop condition for $\beta = -1$ discards collinear radiation, and the differences between quarks and gluons are manifest in the collinear structure (spin, splitting functions, etc.).

The performance of different substructure variables is explored in Figure 6. Among those considered, n_{constits} provides the highest separation power, followed by $C_1^{\beta=0}$ and $C_1^{\beta=1}$ as was also found by the CMS and ATLAS Collaborations[**REF**].

To more quantitatively study the power of each observable as a discriminator for quark/gluon tagging, Receiver Operating Characteristic (ROC) curves are built by scanning each distribution and plotting the background efficiency (to select gluon jets) vs. the signal efficiency (to select quark jets). Figure 7 shows these ROC curves for all of the variables shown in Figure 6 and the ungroomed mass, representing the best performing mass variable, for jets of $p_T = 300 - 400$ GeV. In addition, we show the ROC curve for the tagger built from a BDT combining all the variables. The details of how the BDT is constructed are explained in Section 4. Clearly, n_{constits} is the best performing variable for all Rs, even though $C_1^{\beta=0}$ is close, particularly for R=0.8. Most other variables have similar performance, except the Q-jet volatility, which shows significantly worse discrimination (this may be due to our choice of rigidity $\alpha = 0.1$, while other studies suggest that a smaller value, such as $\alpha = 0.01$, produces better results). The combination of all variables shows somewhat better discrimination.

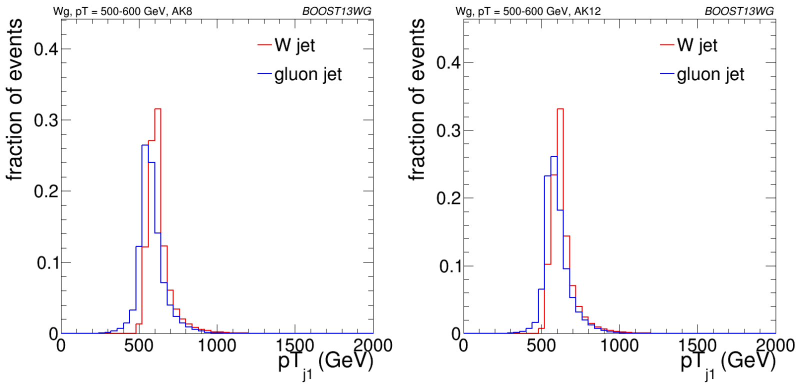

(a) anti-k_{T} R=0.8 (b) anti-k_{T} R=1.2

Fig. 2 Comparisons of the leading jet p_T spectrum of the gg background to the WW signal in the p_T 500-600 GeV parton p_T slice using the different anti-k_{T} jet distance parameters explored in this p_T bin. These distributions are formed prior to the 500-600 GeV leading jet p_T requirement.

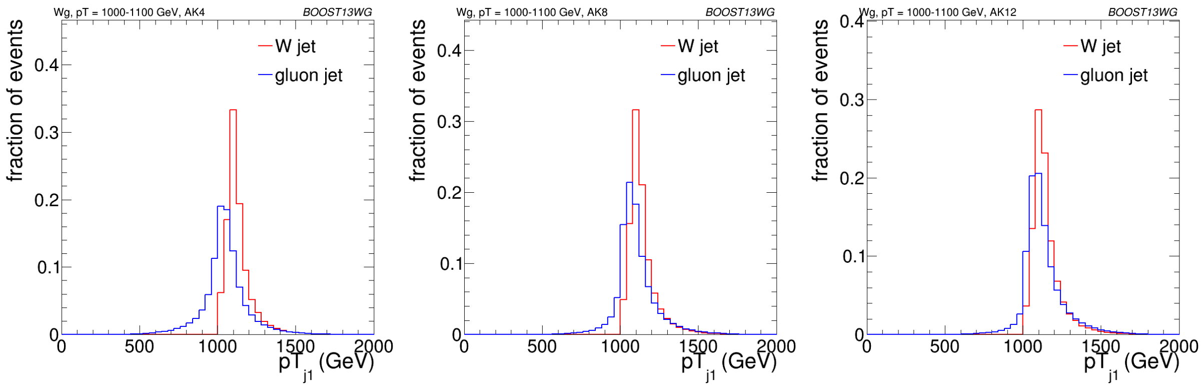

(a) anti-k_{T} R=0.4 (b) anti-k_{T} R=0.8 (c) anti-k_{T} R=1.2

Fig. 3 Comparisons of the leading jet p_T spectrum of the gg background to the WW signal in the p_T 1.0-1.1 TeV parton p_T slice using the different anti-k_{T} jet distance parameters explored in this p_T bin. These distributions are formed prior to the 500-600 GeV leading jet p_T requirement.

We now examine how performance of masses and substructure observables changes with p_T and R. For jet masses, few variations are observed as the radius parameter of the jet reconstruction is increased in the two highest p_T bins; this is because the radiation is more collimated and the dependence on R is consequently smaller. However, for the $300-400$ GeV bin, the use of small-R jets produces a shift in the mass distributions towards lower values, so that large-R jet masses are more stable with p_T and small-R jet masses are smaller at low-p_T as expected from the spatial constraints imposed by the R parameter. These statements are explored more quantitatively later in this section. (**BS: Do we have plots for this?**)

The evolution of some of the substructure variable distributions with p_T and R is less trivial than for the jet masses. In particular, changing the R parameter at high p_T changes significantly the C_a^β for $\beta > 0$ and the n_{constits} distributions, while leaving all other distributions qualitatively unchanged. This is illustrated in Figure 8 for $\beta = 0$ and $\beta = 1$ using $a = 1$ in both cases for jets with $p_T = 1-1.2$ TeV.

The shift towards lower values with changing R is evident for the $C_1^{\beta=1}$ distributions, while the stability of $C_1^{\beta=0}$ can also be observed. These features are present in all p_T bins studied, but are even more pronounced for lower p_T bins. The shape of the Q-jet volatility distribution shows some non-trivial shape that deserves some explanation. Two peaks are observed, one at low volatility values and one at mid-volatility. These peaks are generated by two somewhat distinct populations. The high volatility peak arises from jets that get their mass primarily from soft (and sometimes wide-angle) emissions. The removal of some of the constituents when

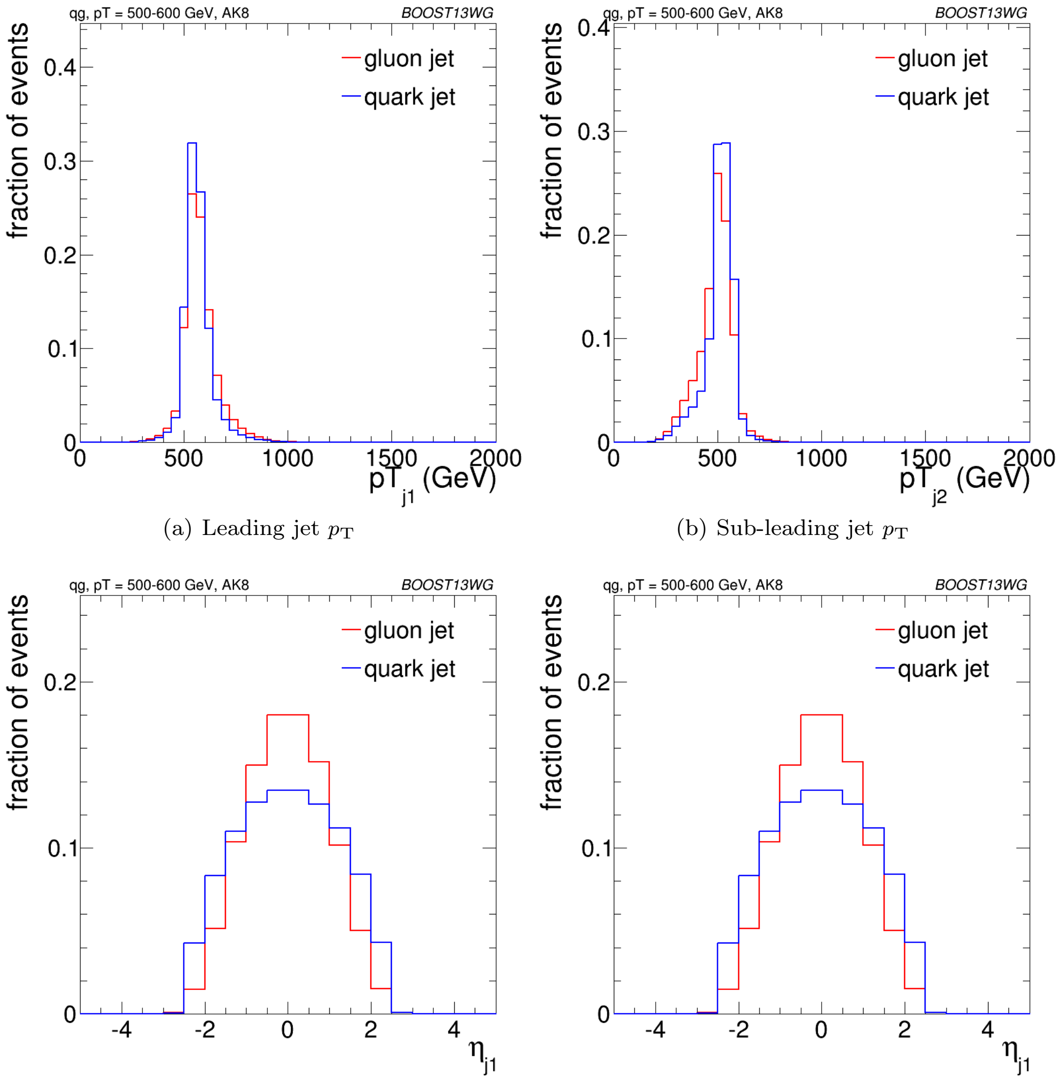

(a) Leading jet p_{T} (b) Sub-leading jet p_{T}

(c) Leading jet η (d) Sub-leading jet η

Fig. 4 Comparisons of quark and gluon p_T and η distributions in the sample used for the jets of $p_T = 500-600$ GeV bin using the anti-k_{T} R=0.8 algorithm.

building Q-jets thus changes the mass significantly, increasing the volatility. The lower volatility peak corresponds to jets for which mass is generated by a hard emission, which makes the fraction of Q-jets that change the mass significantly to be smaller. Since the probability of a hard emission is proportional to the colour charge (squared), the volatility peak is higher for gluon jets by about the colour factor C_A/C_F.

In summary, the overall discriminating power between quarks and gluons decreases with increasing R due to the reduction in the amount of out-of-cone radiation differences and and increased contamination from the underlying event (**BS: is this ok?**). The broad performance features discussed for this p_T bin also apply to the higher p_T bins. These is further quantified in the next section.

5.3 Combined Performance and Correlations

The quark/gluon tagging performance can be further improved over cuts on single observables by combining multiple observables in a BDT; due to the challenging nature of q/g-tagging, any improvement in performance with multivariable techniques could be critical for certain analyses, and the improvement could be more substantial in data than the marginal benefit found in MC and shown in Fig. 7. Furthermore, insight can be gained into the features allowing for quark/gluon

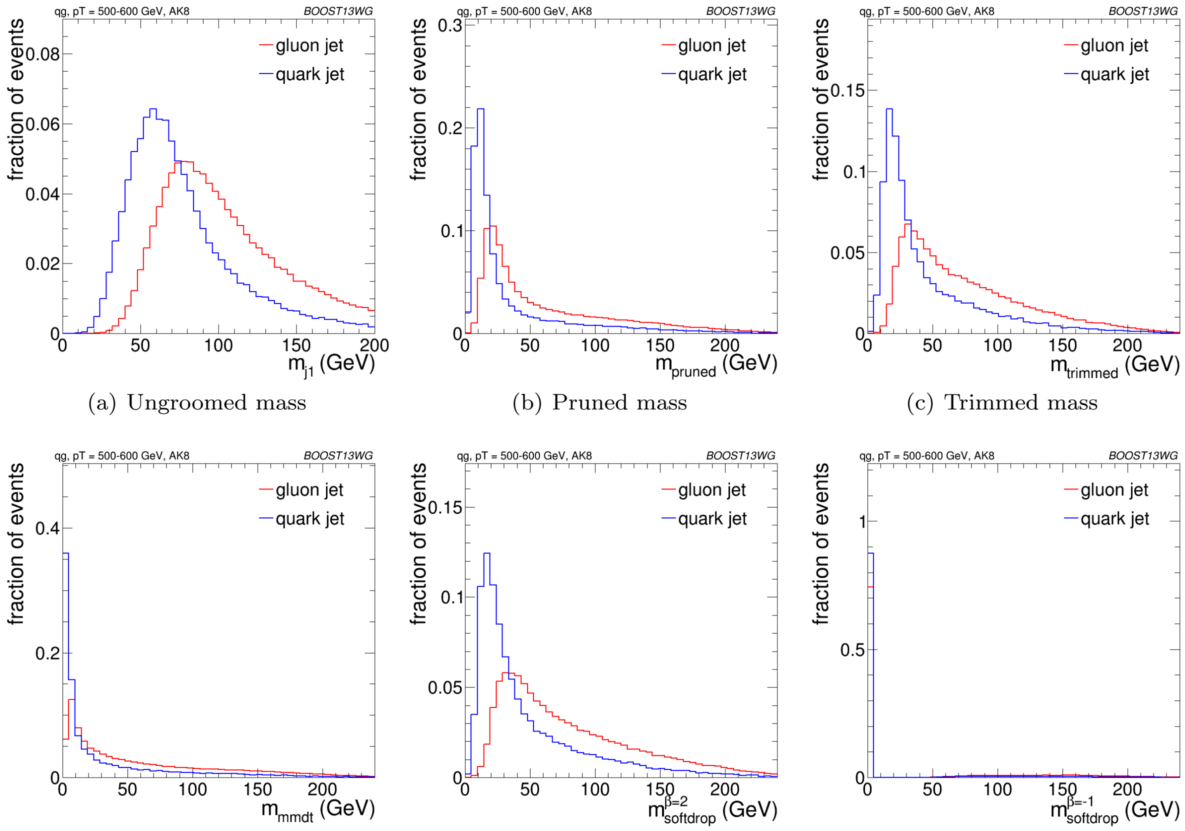

(a) Ungroomed mass (b) Pruned mass (c) Trimmed mass

(d) mMDT mass (e) Soft-drop $\beta = 2$ mass (f) Soft-drop $\beta = -1$ mass

Fig. 5 Comparisons of ungroomed and groomed quark and gluon mass distributions for leading jets in the $p_T = 500-650$ GeV bin using the anti-k_{T} R=0.8 algorithm.

discrimination if the origin of the improvement is understood. To quantitatively study this improvement, we build quark/gluon taggers from every pair-wise combination of variables studied in the previous section for comparison with the all-variable combination.

In order to quantitatively study the value of each variable for quark/gluon tagging, we study the gluon rejection, defined as $1/\epsilon_{\mathrm{gluon}}$, at a fixed quark selection efficiency of 50% using jets with $p_T = 1-1.2$ TeV and for different R parameters. Figure 9 shows the gluon rejection for each pair-wise combination. The pair-wise gluon rejection at 50% quark efficiency can be compared to the single-variable values shown along the diagonal. The gluon rejection for the BDT all-variable combination is also shown on the bottom right of each plot. As already observed in the previous section, n_{constits} is the most powerful single variable and $C_1^{(\beta=0)}$ follows closely. However, the gains are largely correlated; the combined performance of n_{constits} and $C_1^{(\beta=0)}$ is generally poorer than combinations of n_{constits} with other jet substructure observables, such as τ_1. Interestingly, in spite of the high correlation between n_{constits} and $C_1^{(\beta=0)}$, the two-variable combinations of n_{constits} generally fare worse than two-variable combinations with $C_1^{(\beta=0)}$. In particular, the combinations of $\tau_1^{\beta=1}$ or $C_1^{(\beta=1)}$ with n_{constits} are capable of getting very close to the rejection achievable through the use of all variables for $R = 0.4$ and $R = 0.8$.

Tagger performance is generally better at small R. The overall loss in performance with increasing R can be seen in most single variables we study; this is expected, since more of the parton radiation is captured in the jet and more contamination from underlying event occurs, suppressing the differences between q/g jets. The principal exceptions are $C_1^{(\beta=0)}$ and the Q-jet mass volatility, which are both quite resilient to increasing R. For $C_1^{(\beta=0)}$, this is due to the fact that the exponent on ΔR is zero, and so soft radiation at the periphery of the jet does not substantially change the distribution; as a result, the performance is largely independent of R. Similarly, the soft radiation distant from the jet centre will be vetoed during pruning regardless of the cluster sequence, and so the R-dependence of Γ_{Qjet} is not significant. (**BS: Check my logic?**) Their combination,

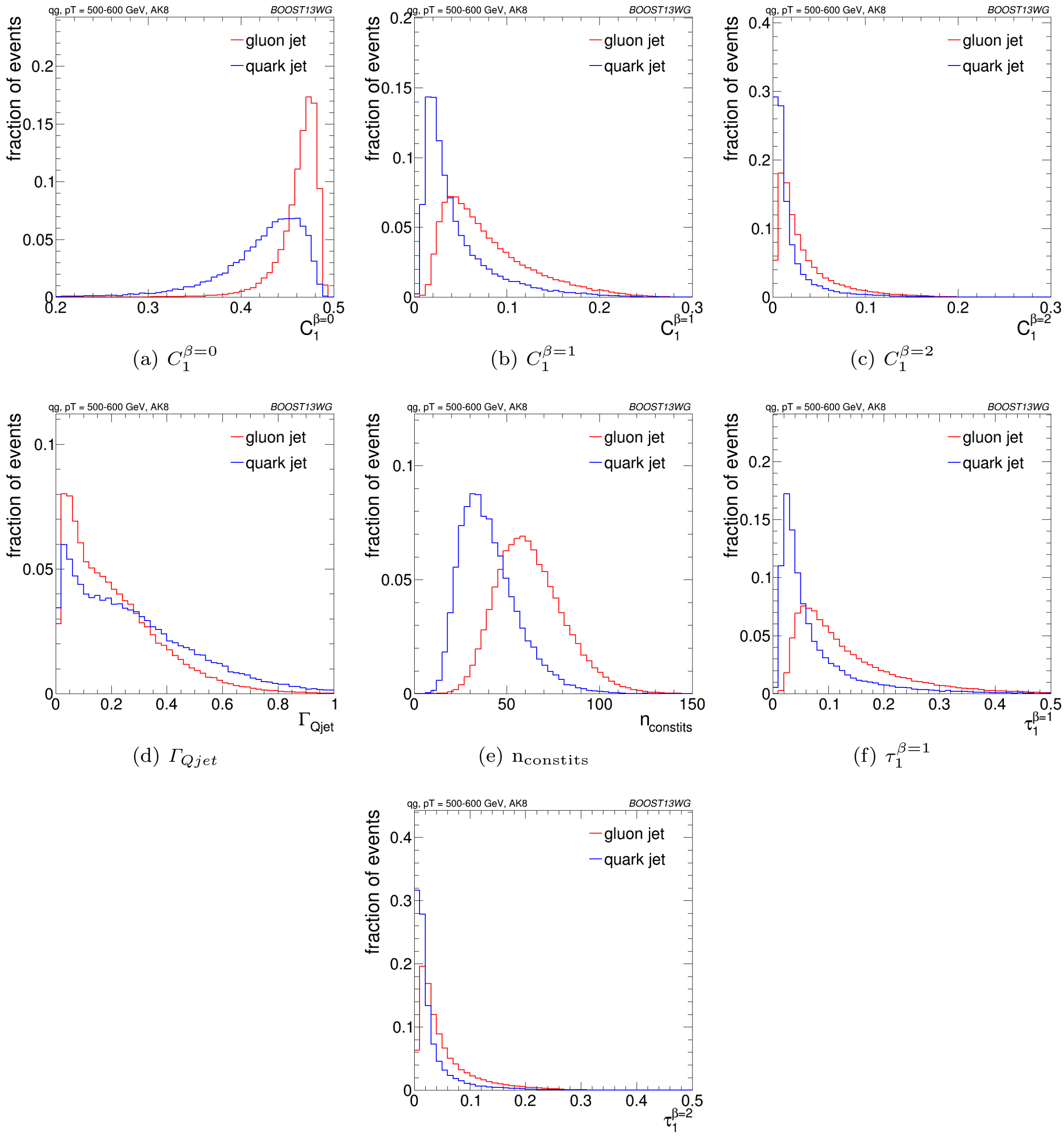

(a) $C_1^{\beta=0}$ (b) $C_1^{\beta=1}$ (c) $C_1^{\beta=2}$

(d) Γ_{Qjet} (e) $\mathrm{n_{constits}}$ (f) $\tau_1^{\beta=1}$

(g) $\tau_1^{\beta=2}$

Fig. 6 Comparisons of quark and gluon distributions of different substructure variables for leading jets in the $p_T = 500 - 650$ GeV bin using the anti-k_{T} R=0.8 algorithm.

however, does perform slightly worse at larger R. (**BS: I don't understand this, but it is a $\sim$ 10% effect, so maybe not too significant?**). By contrast, $\tau_1^{(\beta=2)}$ and $C_1^{(\beta=2)}$ are particularly sensitive to increasing R since, for $\beta = 2$, large-angle emissions are given a larger weight.

These observations are qualitatively similar across all ranges of p_T. Quantitatively, however, there is a loss of rejection power for the taggers made of a combination of variables as the p_T decreases. This can be observed in Fig. 10 for anti-k_{T} R=0.4 jets of different p_Ts. Clearly, most single variables retain their gluon rejection potential at lower p_T. However, when combined with other variables, the highest performing pairwise combinations lose ground with respect to other pairwise combinations. This is also reflected in the rejection of the tagger that uses a combination of all variables,

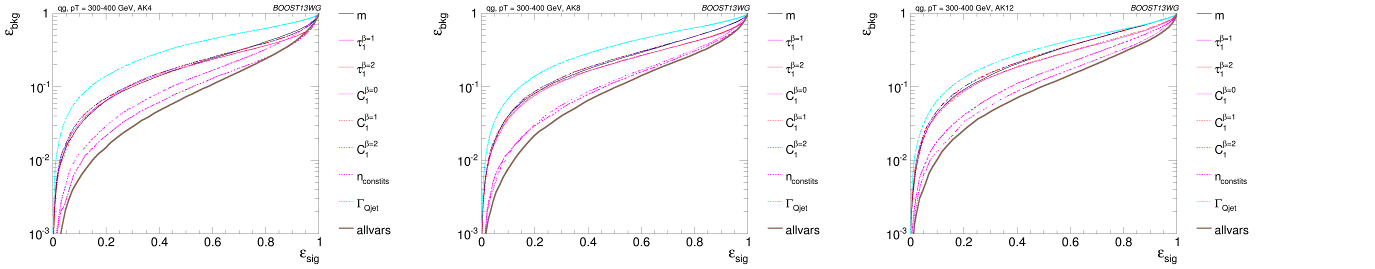

Fig. 7 The ROC curve for all single variables considered for quark-gluon discrimination in the p_T 500 GeV bin using the anti-k_{T} R=0.8 algorithm.

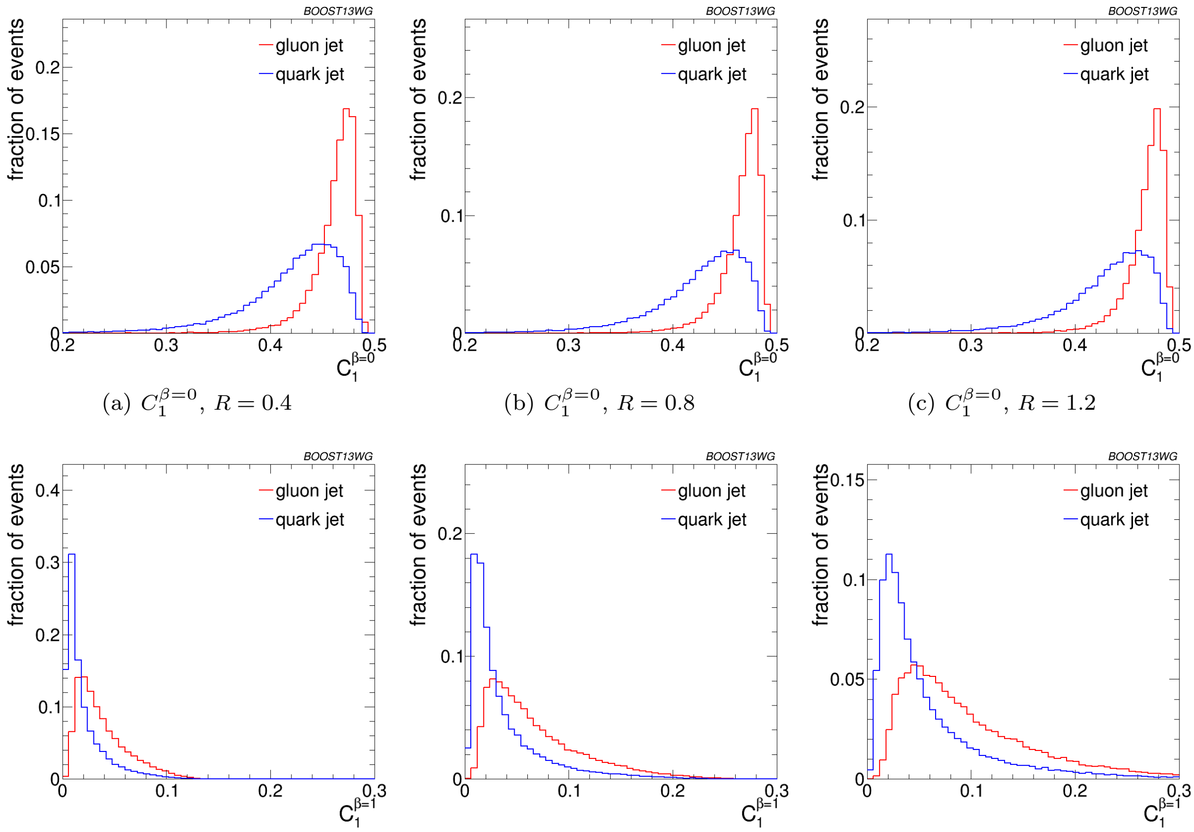

(a) $C_1^{\beta=0}$, $R = 0.4$ (b) $C_1^{\beta=0}$, $R = 0.8$ (c) $C_1^{\beta=0}$, $R = 1.2$

(d) $C_1^{\beta=1}$, $R = 0.4$ (e) $C_1^{\beta=1}$, $R = 0.8$ (f) $C_1^{\beta=1}$, $R = 1.2$

Fig. 8 Comparisons of quark and gluon distributions of $C_1^{\beta=0}$ (top) and $C_1^{\beta=1}$ (bottom) for leading jets in the $p_T = 1-1.2$ TeV bin using the anti-k_{T} algorithm with $R = 0.4$, 0.8 and 1.2.

which is lower at lower p_Ts. **[do we understand this?]** (**BS: This is a bit of a guess, but could it be that there is typically less radiation for low p_T, and so you're more sensitive to fluctuations; since you have less access to information, combinations of observables perform less well than at high p_T.**)

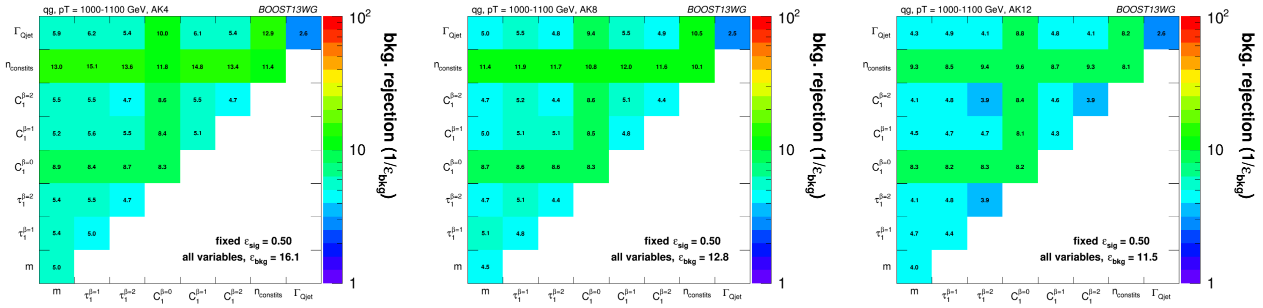

Fig. 9 Gluon rejection defined as $1/\epsilon_{\rm gluon}$ when using each 2-variable combination as a tagger with 50% acceptance for quark jets. Results are shown for jets with $p_T = 1 - 1.2$ TeV and for (left) $R = 0.4$; (centre) $R = 0.8$; (right) $R = 1.2$. The rejection obtained with a tagger that uses all variables is also shown in the plots.

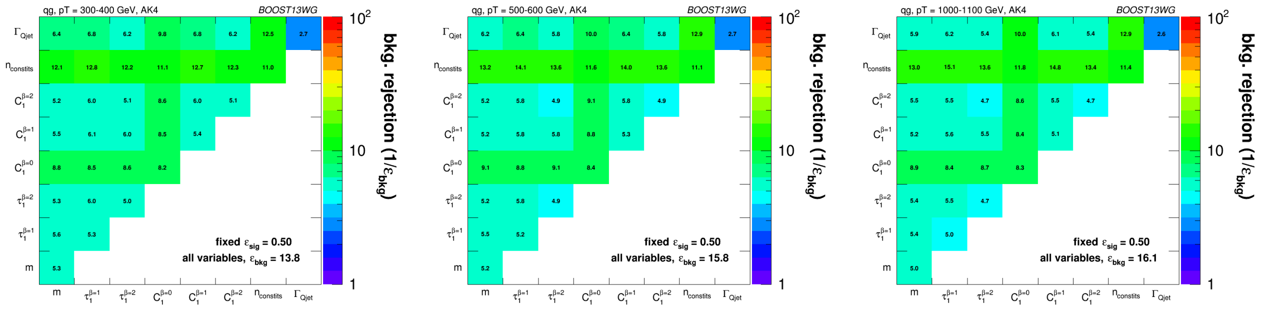

Fig. 10 Gluon rejection defined as $1/\epsilon_{\rm gluon}$ when using each 2-variable combination as a tagger with 50% acceptance for quark jets. Results are shown for R=0.4 jets with $p_T = 300 - 400$ GeV, $p_T = 500 - 600$ GeV and $p_T = 1 - 1.2$ TeV. The rejection obtained with a tagger that uses all variables is also shown in the plots.

6 Boosted *W*-Tagging

In this section, we study the discrimination of a boosted hadronically decaying W signal against a gluon background, comparing the performance of various groomed jet masses, substructure variables, and BDT combinations of groomed mass and substructure. We produce ROC curves that elucidate the performance of the various groomed mass and substructure variables. A range of different distance parameters R for the anti-$k_{\rm T}$ jet algorithm are explored, as well as a variety of kinematic regimes (lead jet p_T 300-400 GeV, 500-600 GeV, 1.0-1.1 TeV). This allows us to determine the performance of observables as a function of jet radius and jet boost, and to see where different approaches may break down. The groomed mass and substructure variables are then combined in a BDT as described in Section 4, and the performance of the resulting BDT discriminant explored through ROC curves to understand the degree to which variables are correlated, and how this changes with jet boost and jet radius.

6.1 Methodology

These studies use the WW samples as signal and the dijet gg samples to model the QCD background, as described previously in Section 2. Whilst only gluonic backgrounds are explored here, the conclusions as to the dependence of the performance and correlations on the jet boost and radius have been verified to hold also for qq backgrounds. **ED: To be checked!**

In each of the three p_T slices considered jets are reconstructed using the anti-$k_{\rm T}$ algorithm with distance parameter R=0.4, 0.8 and 1.2, as described in Section 2. They then have various grooming approaches applied as described in Section 3.5. **(ED: Better if some of the information from Sections 2 and 3.5 is brought into this section to avoid this back-referencing?)**

6.2 Single Variable Performance

In this section we will explore the performance of the various groomed jet mass and substructure variables in terms of discriminating signal and background, and how this performance changes depending on the kinematic bin and jet radius considered.

Figure 11 the compares the signal and background in terms of the different groomed masses explored for the anti-k_T R=0.8 algorithm in the p_T 500-600 bin. One can clearly see that in terms of separating signal and background the groomed masses will be significantly more performant than the ungroomed anti-k_T R=0.8 mass. Figure 12 compares signal and background in the different substructure variables explored for the same jet radius and kinematic bin.

Figures 13, 14 and 15 show the single variable ROC curves compared to the ROC curve for a BDT combination of all the variables (labelled "allvars"), for each of the anti-k_T distance parameters considered in each of the kinematic bins. One can see that, in all cases, the "allvars" option is considerably better performant than any of the individual single variables considered, indicating that there is considerable complementarity between the variables, and this will be explored further in the next section.

Although the ROC curves give all the relevant information, it is hard to compare performance quantitatively. In Figures 16, 17 and 18 are shown matrices which give the background rejection for a signal efficiency of 70% when two variables (that on the x-axis and that on the y-axis) are combined in a BDT. These are shown separately for each p_T bin and jet radius considered. In the final column of these plots are shown the background rejection performance for three-variable BDT combinations of $m_{sd}^{\beta=2} + C_2^{\beta=1} + X$. These results will be discussed later in Section 6.3.3. The diagonal of these plots correspond to the background rejections for a single variable BDT, and can thus be examined to get a quantitative measure of the individual single variable performance, and to study how this changes with jet radius and momenta.

One can see that in general the most performant single variables are the groomed masses. However, in certain kinematic bins and for certain jet radii, $C_2^{\beta=1}$ has a background rejection that is comparable to or better than the groomed masses.

By comparing Figures 16(a), 17(a) and 18(b), we can see how the background rejection performance evolves as we increase momenta whilst keeping the jet radius fixed to R=0.8. Similarly, by comparing Figures 16(b), 17(b) and 18(c) we can see how performance evolves with p_T for R=1.2. For both R=0.8 and R=1.2 the background rejection power of the groomed masses increases with increasing p_T , with a factor 1.5-2.5 increase in rejection in going from the 300-400 GeV to 1.0-1.1 TeV bins. **ED: Add some of the 1-D plots comparing signal and bkgd in the different masses and pT bins here?** However, the $C_2^{\beta=1}$, Γ_{Qjet} and $\tau_{21}^{\beta=1}$ substructure variables behave somewhat differently. The background rejection power of the Γ_{Qjet} and $\tau_{21}^{\beta=1}$ variables both decrease with increasing p_T , by up to a factor two in going from the 300-400 GeV to 1.0-1.1 TeV bins. Conversely the rejection power of $C_2^{\beta=1}$ dramatically increases with increasing p_T for R=0.8, but does not improve with p_T for the larger jet radius R=1.2. **ED: Can we explain this? Again, should we add some of the 1-D plots?**

By comparing the individual sub-figures of Figures 16, 17 and 18 we can see how the background rejection performance depends on jet radius within the same p_T bin. To within $\sim 25\%$, the background rejection power of the groomed masses remains constant with respect to the jet radius. However, we again see rather different behaviour for the substructure variables. In all p_T bins considered the most performant substructure variable, $C_2^{\beta=1}$, performs best for an anti-k_T distance parameter of R=0.8. The performance of this variable is dramatically worse for the larger jet radius of R=1.2 (a factor seven worse background rejection in the 1.0-1.1 TeV bin), and substantially worse for R=0.4. For the other jet substructure variables considered, Γ_{Qjet} and $\tau_{21}^{\beta=1}$, their background rejection power also reduces for larger jet radius, but not to the same extent. **ED: Insert some nice discussion/explanation of why jet substructure power generally gets worse as we go to large jet radius, but groomed mass performance does not. Probably need the 1-D figures for this.**

6.3 Combined Performance

The off-diagonal entries in Figures 16, 17 and 18 can be used to compare the performance of different BDT two-variable combinations, and see how this varies as a function of p_T and R. By comparing the background rejection achieved for the two-variable combinations to the background rejection of the "all variables" BDT, one can understand how much more discrimination is possible by adding further variables to the two-variable BDTs.

One can see that in general the most powerful two-variable combinations involve a groomed mass and a non-mass substructure variable ($C_2^{\beta=1}$, Γ_{Qjet} or $\tau_{21}^{\beta=1}$). Two-variable combinations of the substructure variables are not powerful in comparison. Which particular mass + substructure variable combination is the most powerful depends strongly on the p_T and R of the jet, as discussed in the sections that follow.

There is also modest improvement in the background rejection when different groomed masses are combined, compared to the single variable groomed mass perfor-

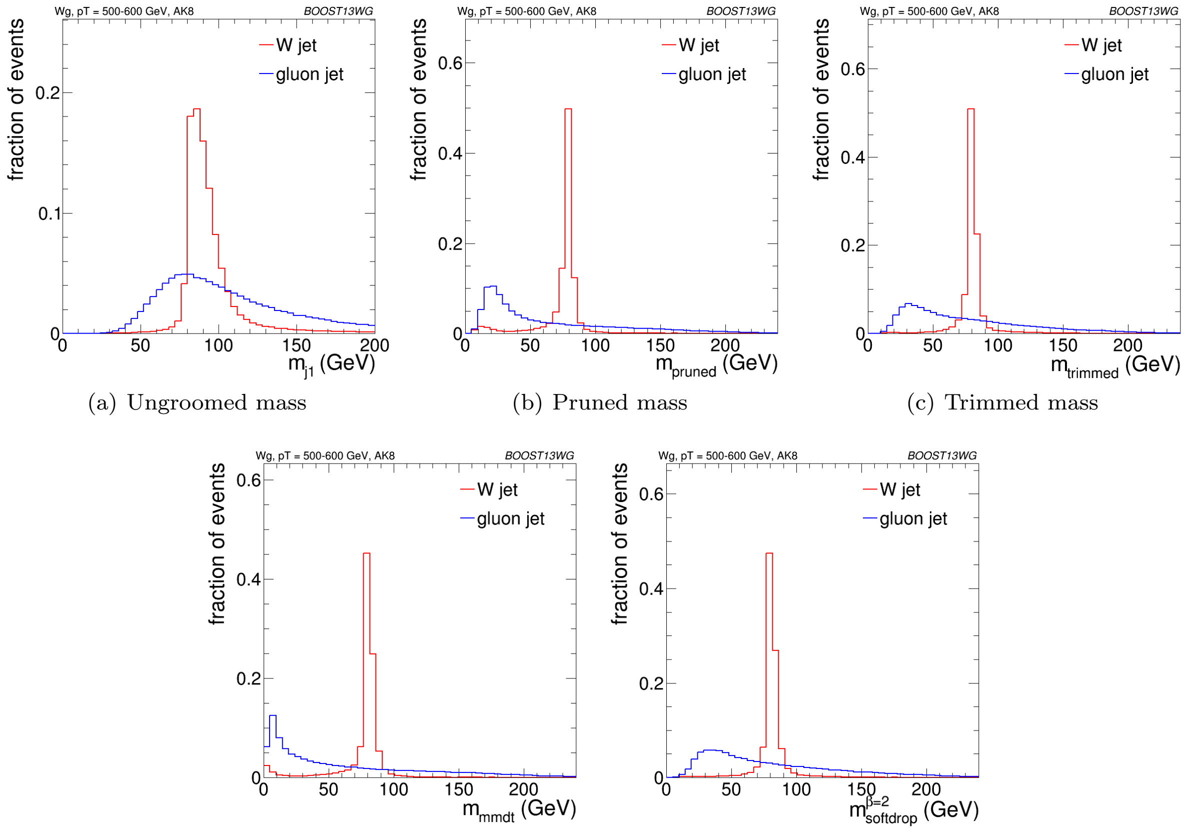

(a) Ungroomed mass (b) Pruned mass (c) Trimmed mass

(d) mMDT mass (e) Soft-drop $\beta = 2$ mass

Fig. 11 Comparisons of the QCD background to the WW signal in the p_T 500-600 GeV bin using the anti-k_{T} R=0.8 algorithm: leading jet mass distributions.

mance, indicating that there is complementary information between the different groomed masses. In addition, there is an improvement in the background rejection when the groomed masses are combined with the ungroomed mass, indicating that grooming removes some useful discriminatory information from the jet. These observations are explored further in the section below.

Generally one can see that the R=0.8 jets offer the best two-variable combined performance in all p_T bins explored here. This is despite the fact that in the highest 1.0-1.1 GeV p_T bin the average separation of the quarks from the W decay is much smaller than 0.8, and well within 0.4. This conclusion could of course be susceptible to pile-up, which is not considered in this study.

6.3.1 Mass + Substructure Performance

As already noted, the largest background rejection at 70% signal efficiency are in general achieved using those two variable BDT combinations which involve a groomed mass and a non-mass substructure variable. For both R=0.8 and R=1.2 jets, the rejection power of these two variable combinations increases substantially with increasing p_T , at least within the p_T range considered here.

For a jet radius of R=0.8, across the full p_T range considered, the groomed mass + substructure variable combinations with the largest background rejection are those which involve $C_2^{\beta=1}$. For example, in combination with $m_{sd}^{\beta=2}$, this produces a five-, eight- and fifteen-fold increase in background rejection compared to using the groomed mass alone. In Figure 19 the low degree of correlation between $m_{sd}^{\beta=2}$ versus $C_2^{\beta=1}$ that leads to these large improvements in background rejection can be seen. One can also see that what little correlation exists is rather non-linear in nature, changing from a negative to a positive correlation as a function of the groomed mass, something which helps to improve the background rejection in the region of the W mass peak.

However, when we switch to a jet radius of R=1.2 the picture for $C_2^{\beta=1}$ combinations changes dramatically. These become significantly less powerful, and the most powerful variable in groomed mass combinations

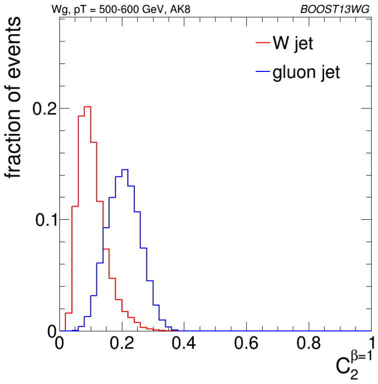

(a) $C_2^{\beta=1}$

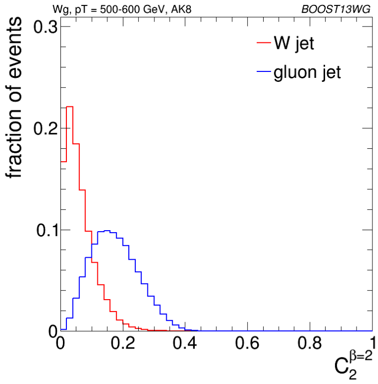

(b) $C_2^{\beta=2}$

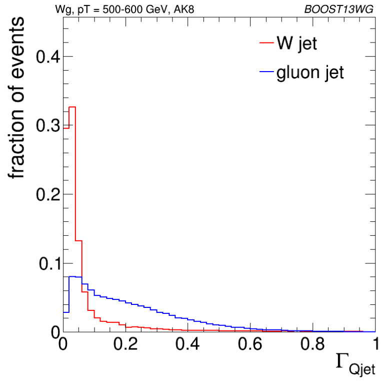

(c) Γ_{Qjet}

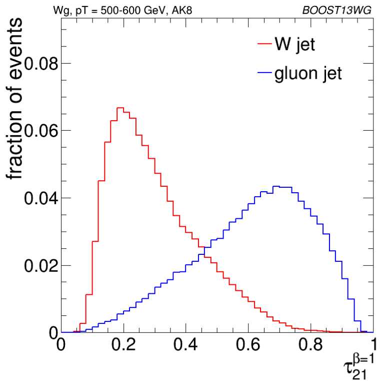

(d) $\tau_{21}^{\beta=1}$

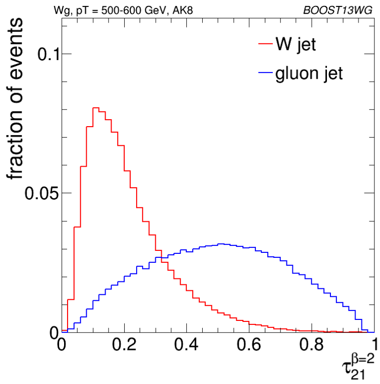

(e) $\tau_{21}^{\beta=2}$

Fig. 12 Comparisons of the QCD background to the WW signal in the p_T 500-600 GeV bin using the anti-k_{T} R=0.8 algorithm: substructure variables.

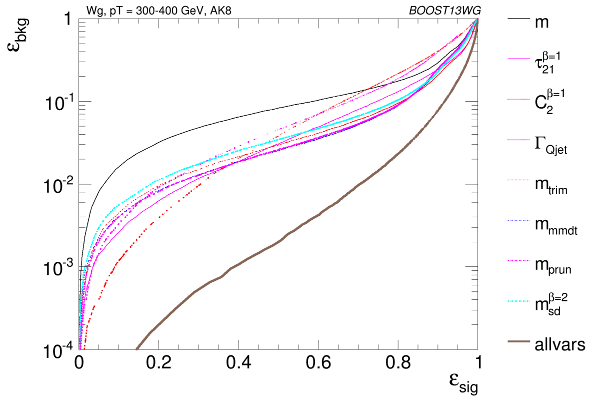

(a) anti-k_{T} R=0.8, p_T 300-400 GeV bin

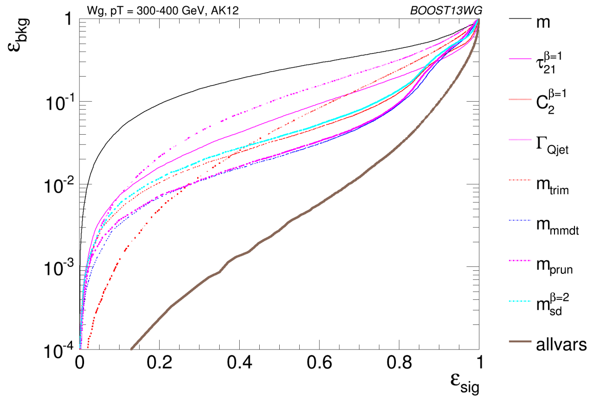

(b) anti-k_{T} R=1.2, p_T 300-400 GeV bin

Fig. 13 The ROC curve for all single variables considered for W tagging in the p_T 300-400 GeV bin using the anti-k_{T} R=0.8 algorithm and R=1.2 algorithm.

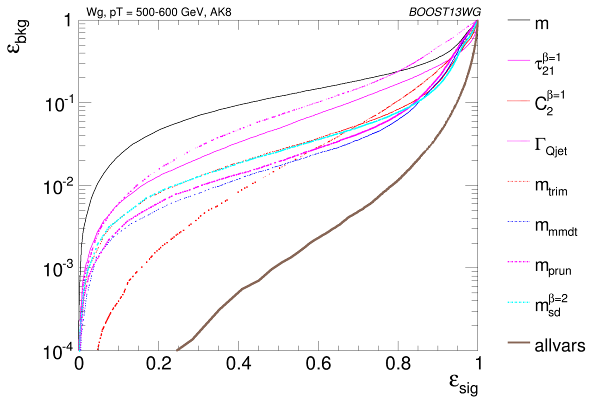

(a) anti-k_T R=0.8, p_T 500-600 GeV bin

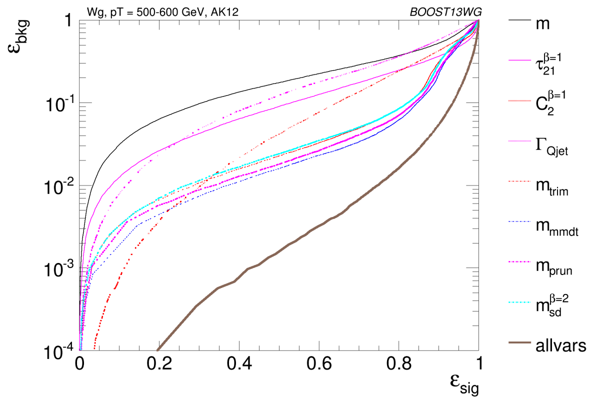

(b) anti-k_T R=1.2, p_T 500-600 GeV bin

Fig. 14 The ROC curve for all single variables considered for W tagging in the p_T 500-600 GeV bin using the anti-k_T R=0.8 algorithm and R=1.2 algorithm.

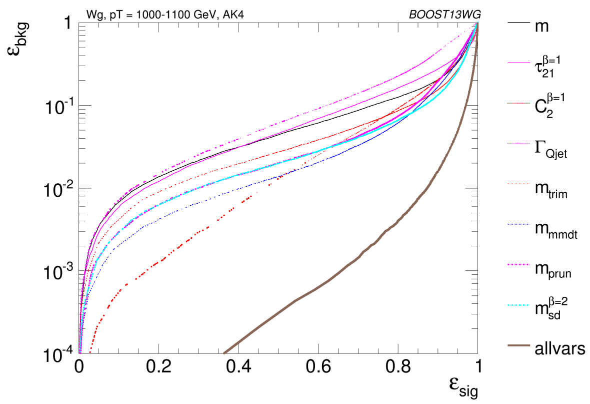

(a) anti-k_T R=0.4, p_T 1.0-1.1 TeV bin

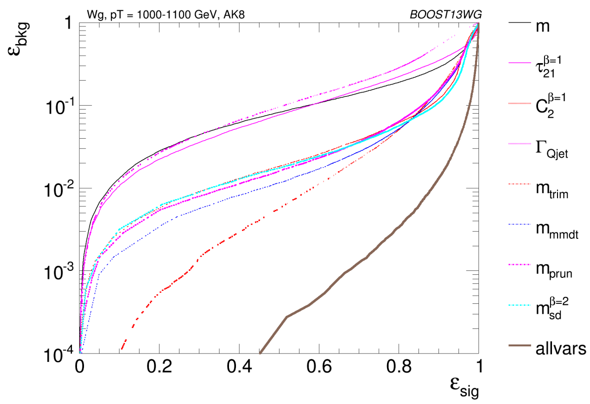

(b) anti-k_T R=0.8, p_T 1.0-1.1 TeV bin

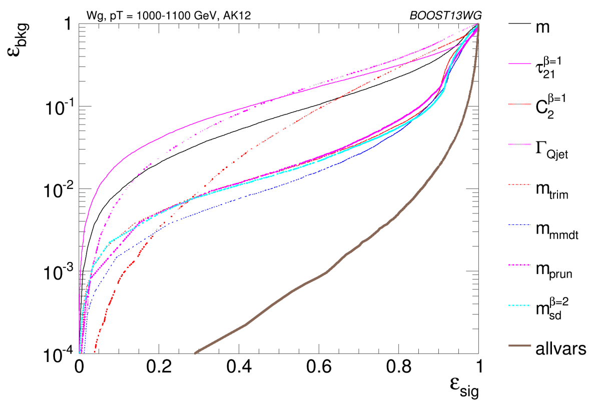

(c) anti-k_T R=1.2, p_T 1.0-1.1 TeV bin

Fig. 15 The ROC curve for all single variables considered for W tagging in the p_T 1.0-1.1 TeV bin using the anti-k_T R=0.4 algorithm, anti-k_T R=0.8 algorithm and R=1.2 algorithm.

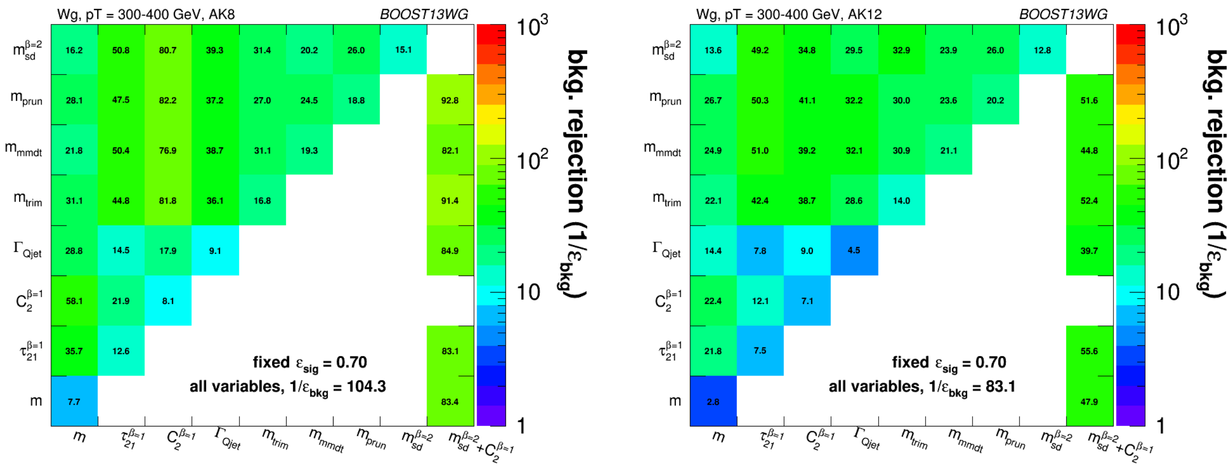

(a) anti-k_T R=0.8, p_T 300-400 GeV bin (b) anti-k_T R=1.2, p_T 300-400 GeV bin

Fig. 16 The background rejection for a fixed signal efficiency (70%) of each BDT combination of each pair of variables considered, in the p_T 300-400 GeV bin using the anti-k_T R=0.8 algorithm and R=1.2 algorithm. Also shown is the background rejection for a BDT combination of all of the variables considered.

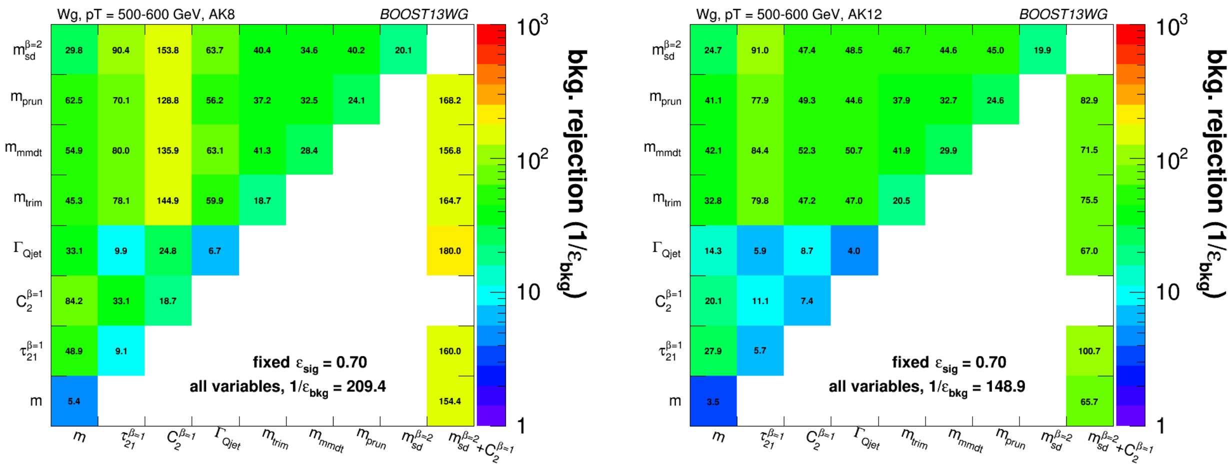

(a) anti-k_T R=0.8, p_T 500-600 GeV bin (b) anti-k_T R=1.2, p_T 500-600 GeV bin

Fig. 17 The background rejection for a fixed signal efficiency (70%) of each BDT combination of each pair of variables considered, in the p_T 500-600 GeV bin using the anti-k_T R=0.8 algorithm and R=1.2 algorithm. Also shown is the background rejection for a BDT combination of all of the variables considered.

becomes $\tau_{21}^{\beta=1}$ for all jet p_T considered. Figure 20 shows the correlation between $m_{sd}^{\beta=2}$ and $C_2^{\beta=1}$ in the p_T 1.0 - 1.2 TeV bin for the various jet radii considered. Figure 21 is the equivalent set of distributions for $m_{sd}^{\beta=2}$ and $\tau_{21}^{\beta=1}$. One can see from Figure 20 that, due to the sensitivity of the observable to to soft, wide-angle radiation, as the jet radius increases $C_2^{\beta=1}$ increases and becomes more and more smeared out for both signal and background, leading to worse discrimination power. This does not happen to the same extent for $\tau_{21}^{\beta=1}$. We can see from Figure 21 that the negative correlation between $m_{sd}^{\beta=2}$ and $\tau_{21}^{\beta=1}$ that is clearly visible for R=0.4 decreases for larger jet radius, such that the groomed mass and substructure variable are far less correlated and $\tau_{21}^{\beta=1}$ offers improved discrimination within a $m_{sd}^{\beta=2}$ mass window.

6.3.2 Mass + Mass Performance

The different groomed masses and the ungroomed mass are of course not fully correlated, and thus one can al-

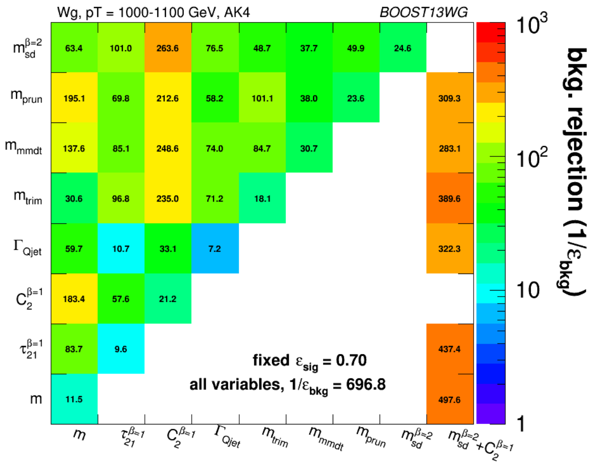

(a) anti-k_T R=0.4, p_T 1.0-1.1 TeV bin

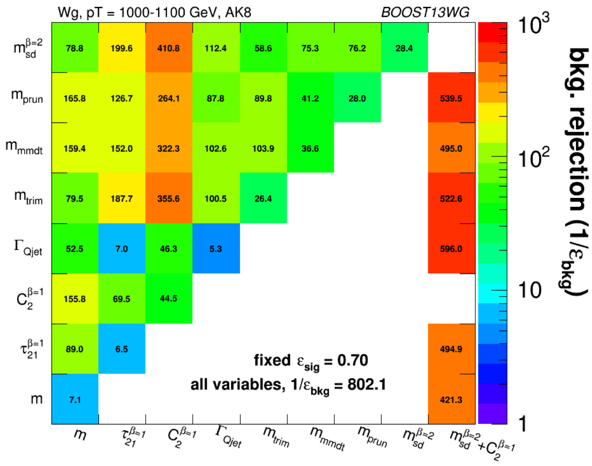

(b) anti-k_T R=0.8, p_T 1.0-1.1 TeV bin

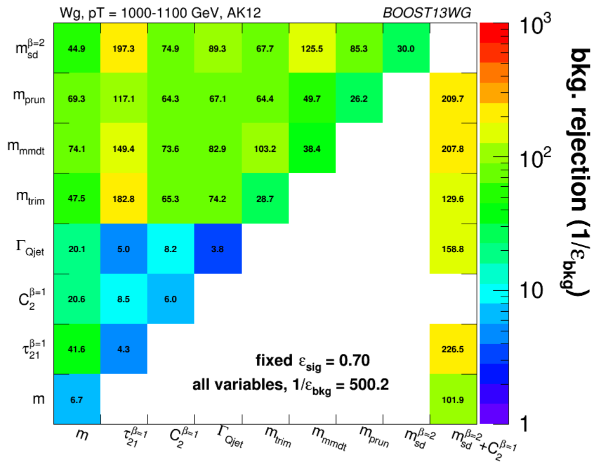

(c) anti-k_T R=1.2, p_T 1.0-1.1 TeV bin

Fig. 18 The background rejection for a fixed signal efficiency (70%) of each BDT combination of each pair of variables considered, in the p_T 1.0-1.1 TeV bin using the anti-k_T R=0.4, R=0.8 and R=1.2 algorithm. Also shown is the background rejection for a BDT combination of all of the variables considered.

ways see some kind of improvement in the background rejection (relative to the single mass performance) when two different mass variables are combined in the BDT. However, in some cases the improvement can be dramatic, particularly at higher p_T , and particularly for combinations with the ungroomed mass. For example, in Figure 18 we can see that in the p_T 1.0-1.1 TeV bin the combination of pruned mass with ungroomed mass produces a greater than eight-fold improvement in the background rejection for R=0.4 jets, a greater than five-fold improvement for R=0.8 jets, and a factor ~two improvement for R=1.2 jets. A similar behaviour can be seen for mMDT mass. In Figures 22, 23 and 24 is shown the 2-D correlation plots of the pruned mass versus the ungroomed mass separately for the WW signal and gg background samples in the p_T 1.0-1.1 TeV bin, for the various jet radii considered. For comparison, the correlation of the trimmed mass with the ungroomed mass, a combination that does not improve on the single mass as dramatically, is shown. In all cases one can see that there is a much smaller degree of correlation between the pruned mass and the ungroomed mass in the backgrounds sample than for the trimmed mass and the ungroomed mass. This is most obvious in Figure 22, where the high degree of correlation between the trimmed and ungroomed mass is expected, since with the parameters used (in particular $R_{trim} = 0.2$) we cannot expect trimming to have a significant impact on an R=0.4 jet. The reduced correlation with ungroomed mass for pruning in the background means that, once we have made the

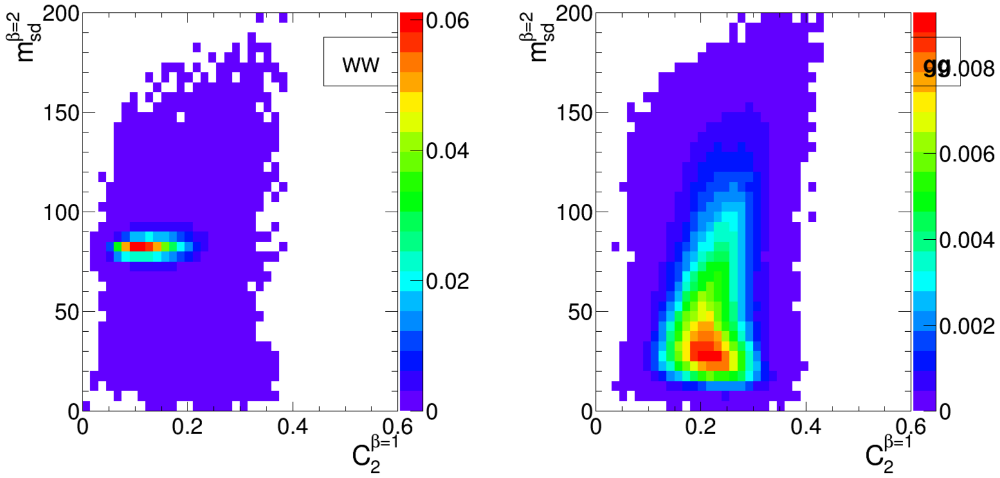

(a) p_T 300-400 GeV

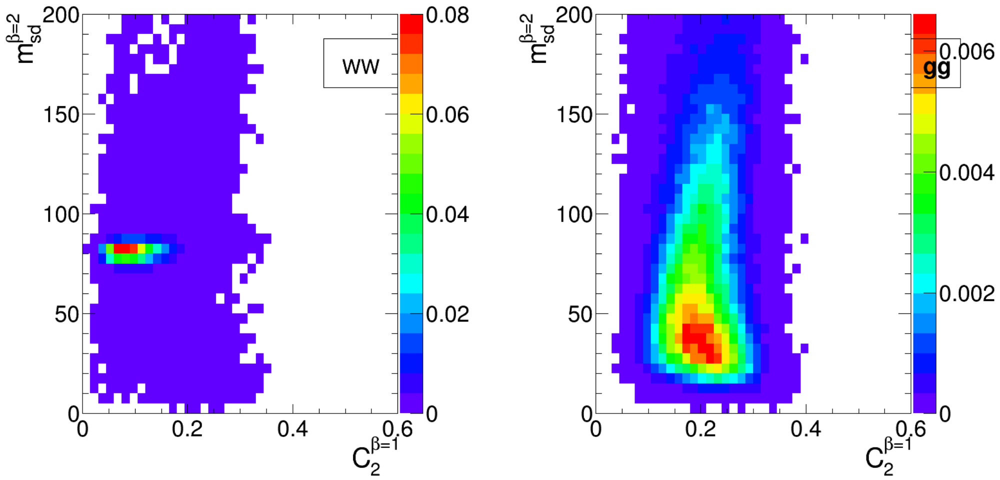

(b) p_T 500-600 GeV

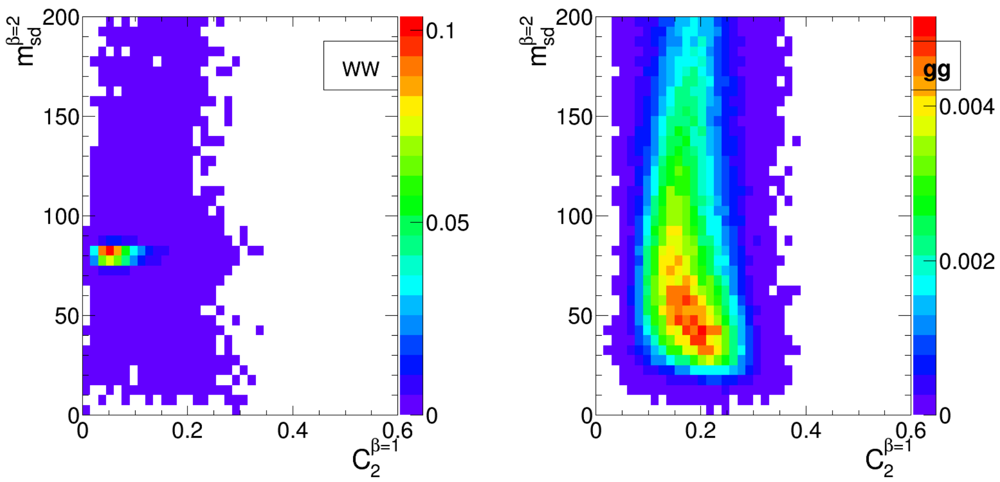

(c) p_T 1.0-1.1 TeV

Fig. 19 2-D plots showing $m_{sd}^{\beta=2}$ versus $C_2^{\beta=1}$ for R=0.8 jets in the various p_T bins considered.

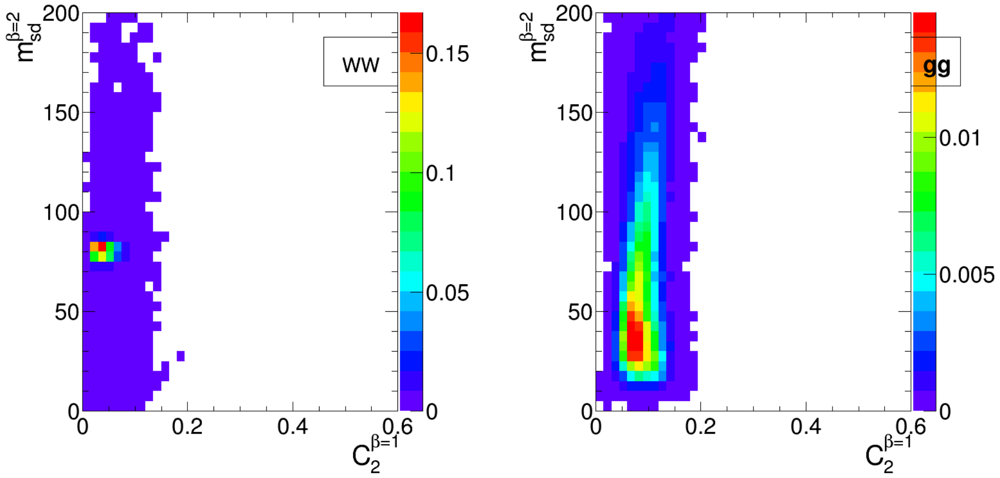

(a) p_T R=0.4

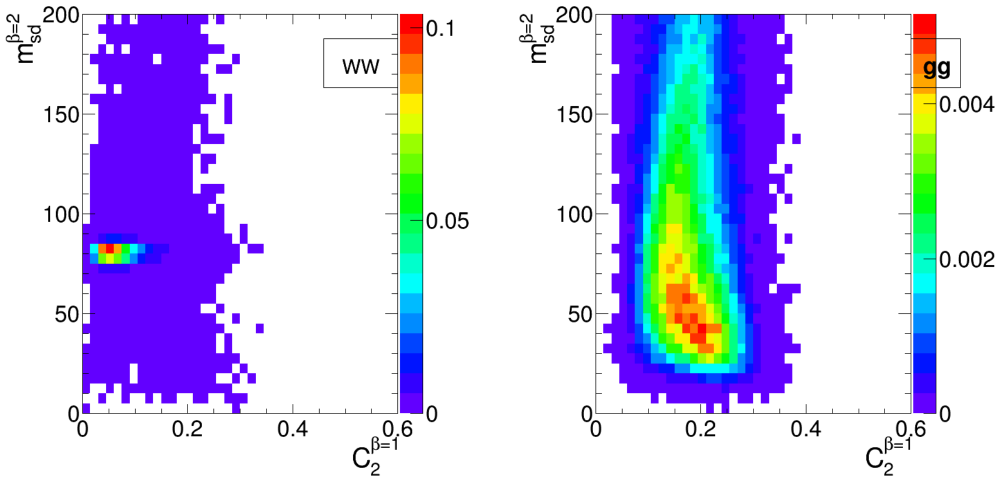

(b) p_T R=0.8

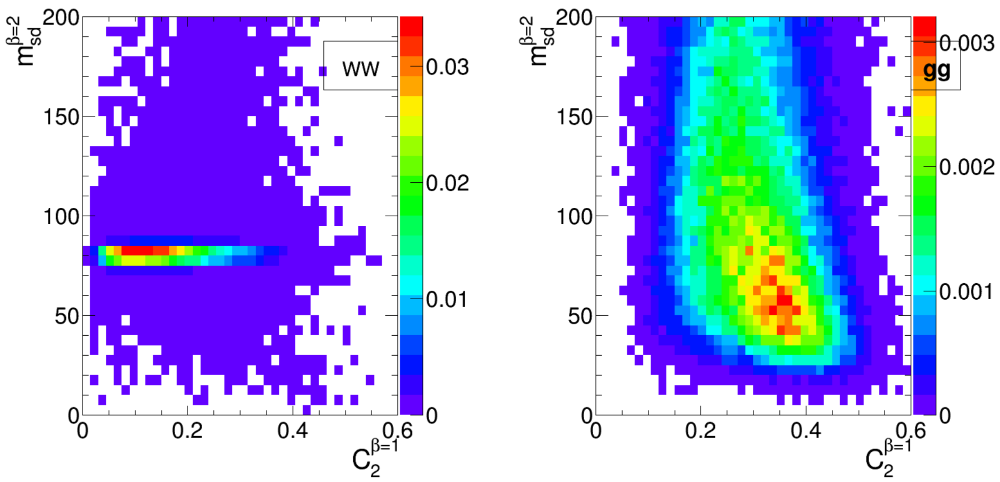

(c) p_T R=1.2

Fig. 20 2-D plots showing $m_{sd}^{\beta=2}$ versus $C_2^{\beta=1}$ for R=0.4, 0.8 and 1.2 jets in the p_T 1.0-1.1 TeV bin.

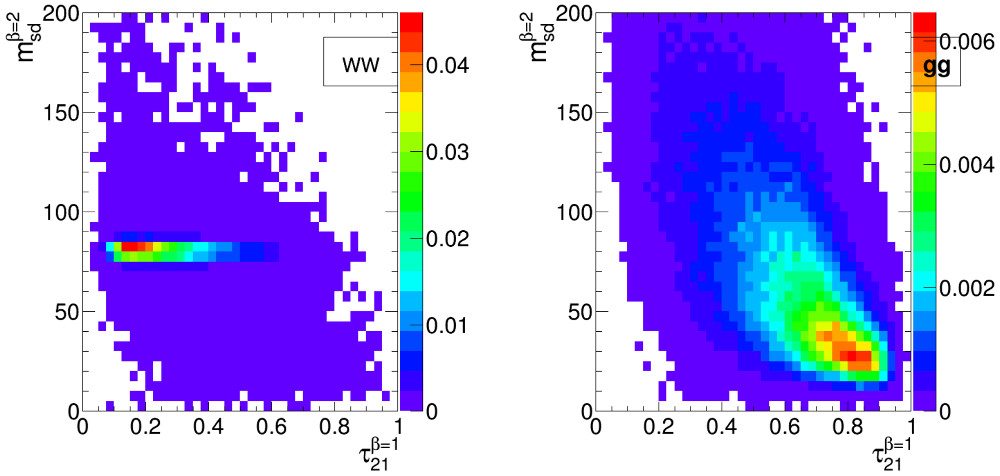

(a) p_T R=0.4

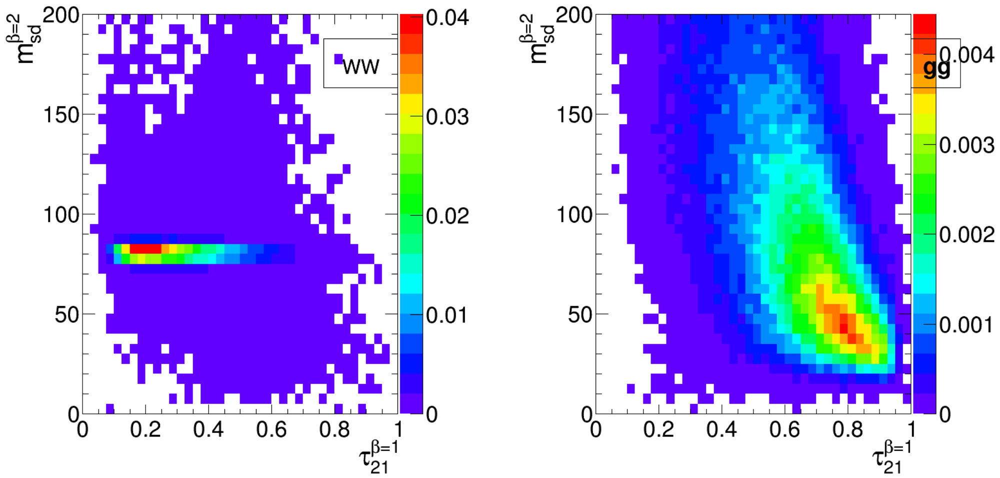

(b) p_T R=0.8

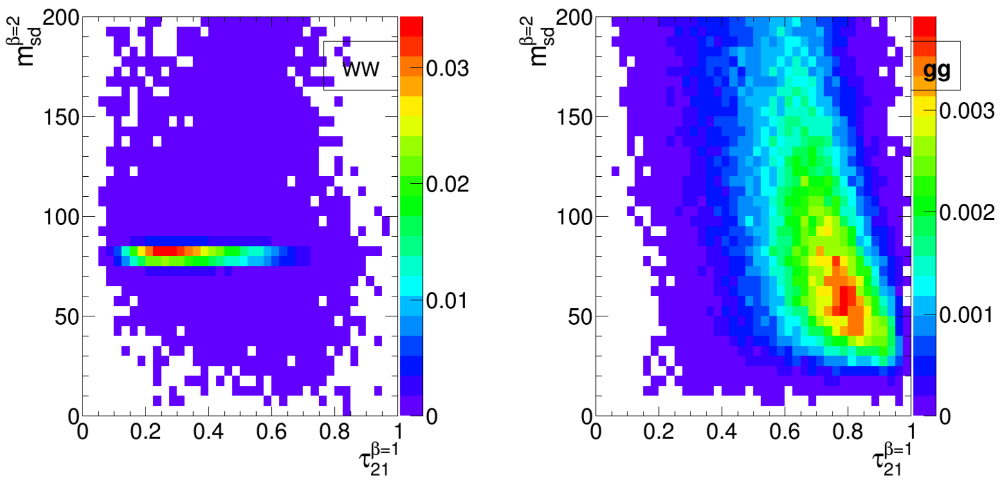

(c) p_T R=1.2

Fig. 21 2-D plots showing $m_{sd}^{\beta=2}$ versus $\tau_{21}^{\beta=1}$ for R=0.4, 0.8 and 1.2 jets in the p_T 1.0-1.1 TeV bin.

requirement that the pruned mass is consistent with a W (i.e. ∼80 GeV), a relatively large difference between signal and background in the ungroomed mass still remains, and can be exploited to improve the background rejection further. In other words, many of the background events which pass the pruned mass requirement do so because they are shifted to lower mass (to be within a signal mass window) by the grooming, but these events still have the property that they look very much like background events before the grooming. A single requirement on the groomed mass only does not exploit this. Of course, the impact of pile-up, not considered in this study, could significantly limit the degree to which the ungroomed mass could be used to improve discrimination in this way.

6.3.3 "All Variables" Performance

As well as the background rejection at a fixed 70% signal efficiency for two-variable combinations, Figures 16, 17 and 18 also report the background rejection achieved by a combination of all the variables considered into a single BDT discriminant. One can see that, in all cases, the rejection power of this "all variables" BDT is significantly larger than the best two-variable combination. This indicates that beyond the best two-variable combination there is still significant complementary information availiable in the remaining variables in order to improve the discrimination of signal and background. How much complementary information is available appears to be p_T dependent. In the lower p_T 300-400 and 500-600 GeV bins the background rejection of the "all variables" combination is a factor $\sim$ 1.5 greater than the best two-variable combination, but in the highest p_T bin it is a factor $\sim$ 2.5 greater.

The final column in Figures 16, 17 and 18 allows us to explore the all variables performance a little further. It shows the background rejection for three variable BDT combinations of $m_{sd}^{\beta=2} + C_2^{\beta=1} + X$, where X is the variable on the y-axis. For jets with R=0.4 and R=0.8, the combination $m_{sd}^{\beta=2} + C_2^{\beta=1}$ is the best performant (or very close to the best performant) two-variable combination in every p_T bin considered. For R=1.2 this is not the case, as $C_2^{\beta=1}$ is superceded by $\tau_{21}^{\beta=1}$ in performance, as discussed earlier. Thus, in considering the three-variable combination results it is best to focus on the R=0.4 and R=0.8 cases. Here we see that, for the lower p_T 300-400 and 500-600 GeV bins, adding the third variable to the best two-variable combination brings us to within $\sim$ 15% of the "all variables" background rejection. However, in the highest p_T 1.0-1.1 TeV bin, whilst adding the third variable does improve the performance considerably, we are still $\sim$ 40% from the observed "all variables" background rejection, and clearly adding a fourth or maybe even fifth variable would bring considerable gains. In terms of which variable offers the best improvement when added to the $m_{sd}^{\beta=2} + C_2^{\beta=1}$ combination, it is hard to see an obvious pattern; the best third variable changes depending on the p_T and R considered.

In conclusion, it appears that there is a rich and complex structure in terms of the degree to which the discriminatory information provided by the set of variables considered overlaps, with the degree of overlap apparently decreasing at higher p_T . This suggests that in all p_T ranges, but especially at higher p_T , there are substantial performance gains to be made by designing a more complex multivariate W tagger.

6.4 Conclusions

We have studied the performance, in terms of the degree to which a hadronically decaying W boson can be separated from a gluonic background, of a number of groomed jet masses, substructure variables, and BDT combinations of the above. We have used this to build a picture of how the discriminatory information contained in the variables overlaps, and how this complementarity between the variables changes with p_T and anti-k_T distance parameter R.

In terms of the performance of individual variables, we find that, in agreement with other studies[**REF**], in general the groomed masses perform best, with a background rejection power that increases with increasing p_T , but which is more constant with respect to changes in R. Conversely, the performance of other substructure variables, such as $C_2^{\beta=1}$ and $\tau_{21}^{\beta=1}$ is more susceptible to changes in radius, with background rejection power decreasing with increasing R.

The best two-variable performance is obtained by combining a groomed mass with a substructure variable. Which particular substructure variable works best in combination is strongly dependent on p_T and R. $C_2^{\beta=1}$ offers significant complimentarity to groomed mass at smaller R, owing to the small degree of correlation between the variables. However, the sensitivity of $C_2^{\beta=1}$ to soft, wide-angle radiation leads to worse discrimination power at large R, where $\tau_{21}^{\beta=1}$ performs better in combination. Our studies also demonstrate the potential for enhanced discrmination by combining groomed and ungroomed mass information, although the use of ungroomed mass in this may in practice be limited by the presence of pile-up that is not considered in these studies.

By examining the performance of a BDT combination of all the variables considered, it is clear that

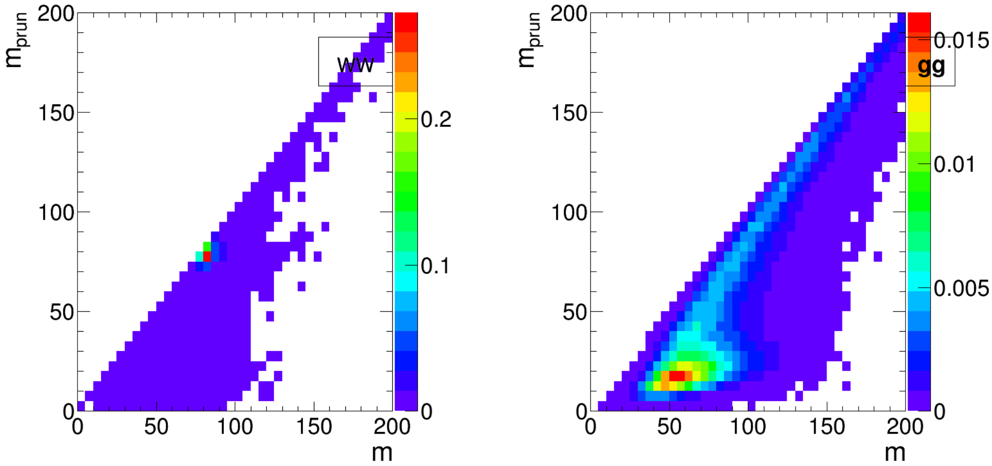

(a) Pruned mass vs ungroomed mass

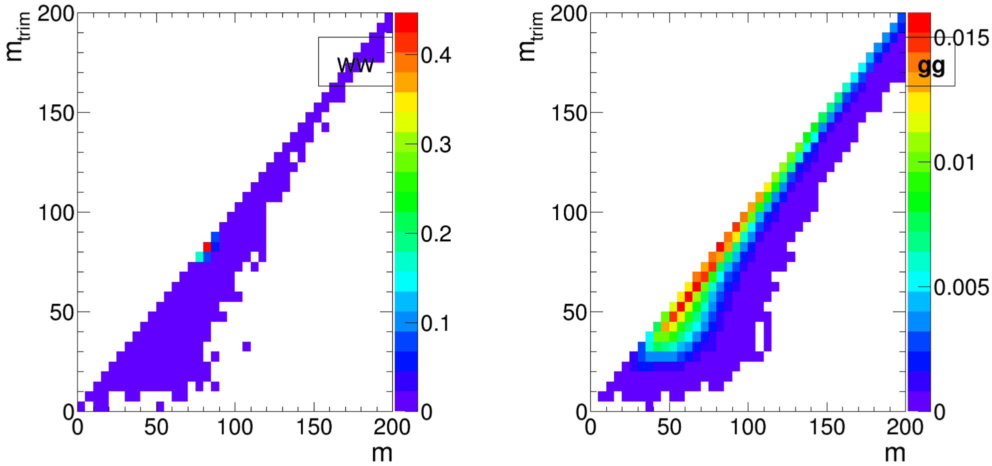

(b) Trimmed mass vs ungroomed mass

Fig. 22 2-D plots showing the correlation between groomed and ungroomed mass for WW and gg events in the p_T 1.0-1.1 TeV bin using the anti-k_T R=0.4 algorithm.

there are potentially substantial performance gains to be made by designing a more complex multivariate W tagger, especially at higher p_T .

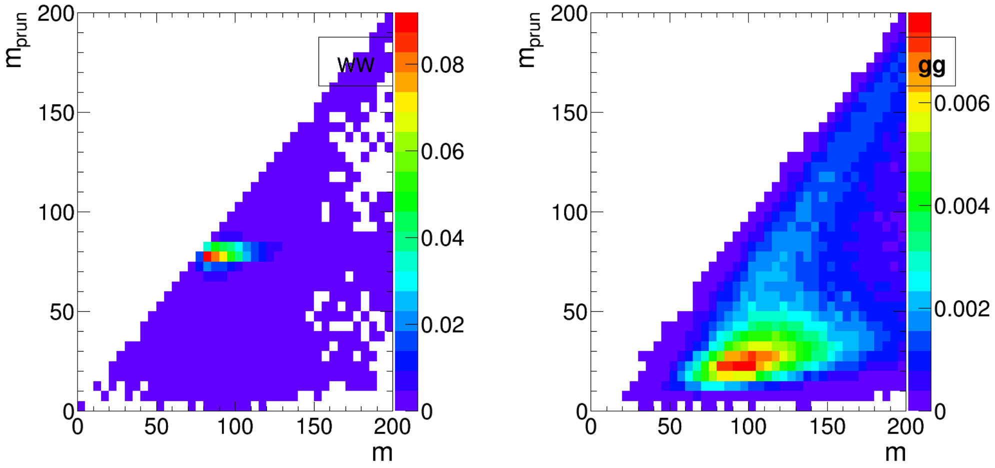

(a) Pruned mass vs ungroomed mass

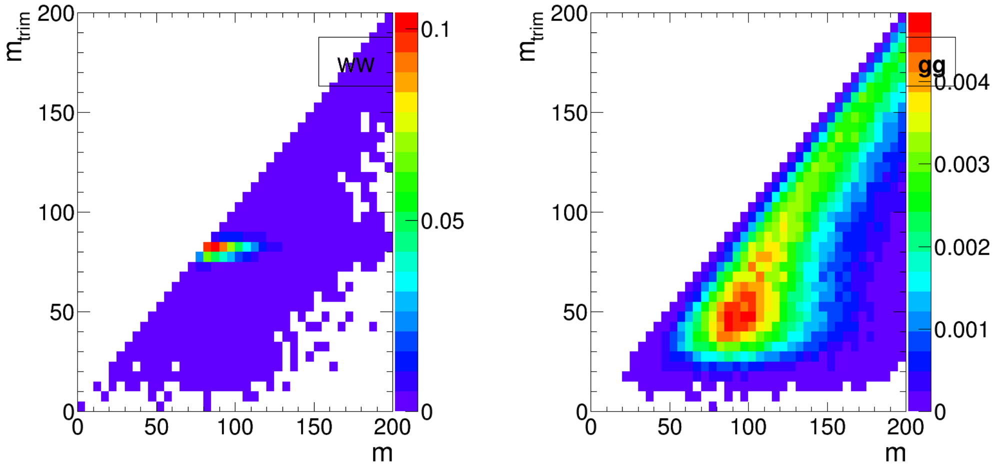

(b) Trimmed mass vs ungroomed mass

Fig. 23 2-D plots showing the correlation between groomed and ungroomed mass for WW and gg events in the p_T 1.0-1.1 TeV bin using the anti-k_{T} R=0.8 algorithm.

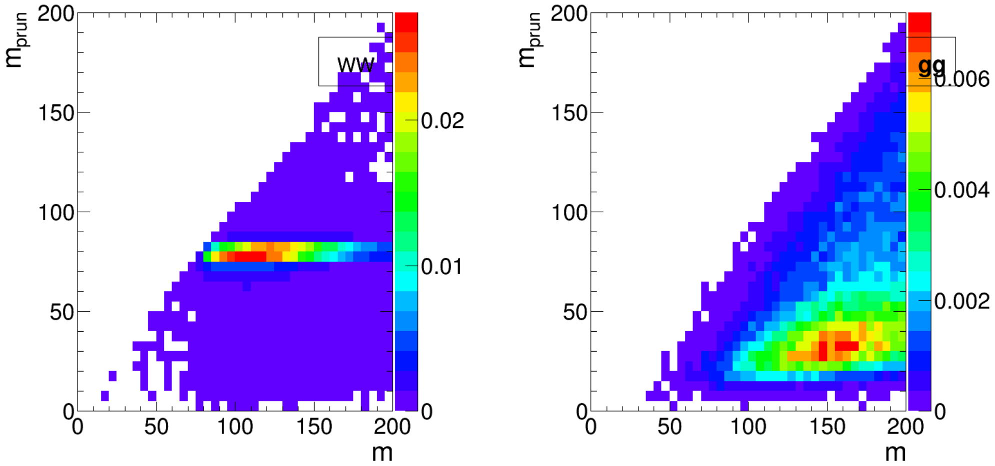

(a) Pruned mass vs ungroomed mass

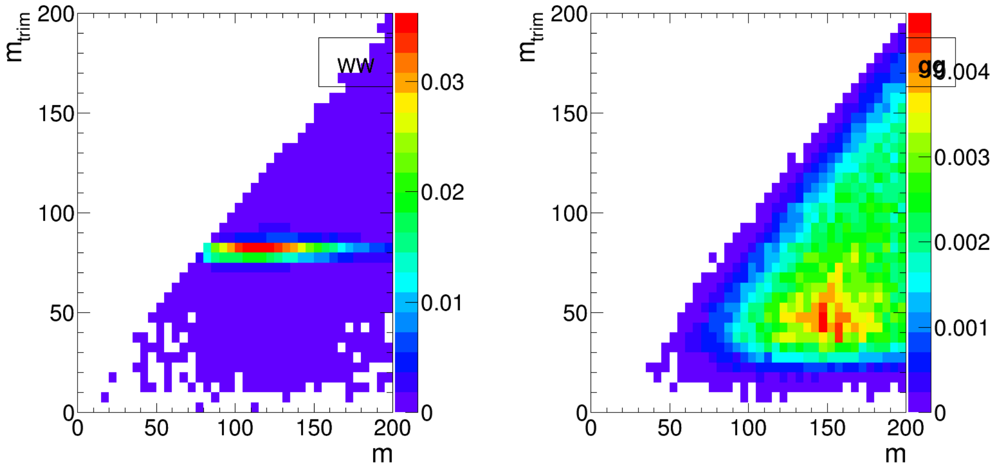

(b) Trimmed mass vs ungroomed mass

Fig. 24 2-D plots showing the correlation between groomed and ungroomed mass for WW and gg events in the p_T 1.0-1.1 TeV bin using the anti-k_{T} R=1.2 algorithm.

7 Top Tagging

In this section, we study the identification of boosted top quarks at Run II of the LHC. Boosted top quarks result in large-radius jets with complex substructure, containing a b-subjet and a boosted W. The additional kinematic handles coming from the reconstruction of the W mass and b-tagging allows a very high degree of discrimination of top quark jets from QCD backgrounds.

We consider top quarks with moderate boost (600-1000 GeV), and perhaps most interestingly, at high boost ($\gtrsim$ 1500 GeV). Top tagging faces several challenges in the high-p_T regime. For such high-p_T jets, the b-tagging efficiencies are no longer reliably known. Also, the top jet can also accompanied by additional radiation with $p_T \sim m_t$, leading to combinatoric ambiguities of reconstructing the top and W, and the possibility that existing taggers or observables shape the background by looking for subjet combinations that reconstruct m_t/m_W. To study this, we examine the performance of both mass-reconstruction variables, as well as shape observables that probe the three-pronged nature of the top jet and the accompanying radiation pattern.

7.1 Methodology

We study a number of top-tagging strategies, in particular:

1. HEPTopTagger
2. Johns Hopkins Tagger (JH)
3. Trimming
4. Pruning

The top taggers have criteria for reconstructing a top and W candidate, and a corresponding top and W mass, as described in Section 3.3, while the grooming algorithms (trimming and pruning) do not incorporate a W-identification step. For a level playing field, where grooming is used we construct a W candidate mass, m_W, from the three leading subjets by taking the mass of the pair of subjets with the smallest invariant mass; in the case that only two subjets are reconstructed, we take the mass of the leading subjet. The top mass, m_t, is the mass of the groomed jet. All of the above taggers and groomers incorporate a step to remove pile-up and other soft radiation.

We also consider the performance of jet shape observables. In particular, we consider the N-subjettiness ratios $\tau_{32}^{\beta=1}$ and $\tau_{21}^{\beta=1}$, energy correlation function ratios $C_3^{\beta=1}$ and $C_2^{\beta=1}$, and the Qjet mass volatility Γ. In addition to the jet shape performance, we combine the jet shapes with the mass-reconstruction methods described above to determine the optimal combined performance.

For determining the performance of multiple variables, we combine the relevant tagger output observables and/or jet shapes into a boosted decision tree (BDT), which determines the optimal cut. Additionally, because each tagger has two input parameters, as described in Section 3.3, we scan over reasonable values of the parameters to determine the optimal value for each top tagging signal efficiency **ED: Optimal value is that which gives largest bkgd rejection?**. This allows a direct comparison of the optimized version of each tagger. The input values scanned for the various algorithms are:

- **HEPTopTagger:** $m \in [30, 100]$ GeV, $\mu \in [0.5, 1]$

- **JH Tagger:** $\delta_p \in [0.02, 0.15]$, $\delta_R \in [0.07, 0.2]$
- **Trimming:** $f_{\rm cut} \in [0.02, 0.14]$, $R_{\rm trim} \in [0.1, 0.5]$
- **Pruning:** $z_{\rm cut} \in [0.02, 0.14]$, $R_{\rm cut} \in [0.1, 0.6]$

7.2 Single-observable performance

We start by investigating the behaviour of individual jet substructure observables. Because of the rich, three-pronged structure of the top decay, it is expected that combinations of masses and jet shapes will far outperform single observables in identifying boosted tops. However, a study of the top-tagging performance of single variables facilitates a direct comparison with the W tagging results in Section 6, and also allows a straightforward examination of the performance of each observable for different p_T and jet radius.

Fig. 25 shows the ROC curves for each of the top-tagging observables, with the bare (ungroomed) jet mass also plotted for comparison. The jet shape observables all perform substantially worse than jet mass, unlike W tagging for which several observables are competitive with or perform better than jet mass (see, for example, Fig. 11). To understand why this is the case, consider N-subjettiness. The W is two-pronged and the top is three-pronged; therefore, we expect τ_{21} and τ_{32} to be the best-performant N-subjettiness ratio, respectively. However, τ_{21} also contains an implicit cut on the denominator, τ_1, which is strongly correlated with jet mass. Therefore, τ_{21} combines both mass and shape information to some extent. By contrast, and as is clear in Fig.25(a), the best shape for top tagging is τ_{32}, which contains no information on the mass. Therefore, it is unsurprising that the shapes most useful for top tagging are less sensitive to the jet mass, and under-perform relative to the corresponding observables for W tagging.

Of the two top tagging algorithms, we can see from Figure 25 that the Johns Hopkins (JH) tagger outperforms the HEPTopTagger in terms of its signal-to-background separation power in both the top and W candidate masses. In Figure 26 we show the histograms for the top mass output from the JH and HEPTopTagger for different R in the p_T 1.5-1.6 TeV bin, and in Figure 27 for different p_T at at R =0.8, optimized at a signal efficiency of 30%. One can see from these figures that the likely reason for the better performance of the JH tagger is that, in the HEPTopTagger algorithm, the jet is filtered to select the five hardest subjets, and then three subjets are chosen which reconstruct the top mass. This requirement tends to shape a peak in the QCD background around m_t for the HEPTopTagger, while the JH tagger has no such requirement. It has been suggested by Anders *et al.* [**?**] that performance in the HEPTopTagger may be improved by selecting the three subjets reconstructing the top only among those that pass the W mass constraints, which somewhat reduces the shaping of the background. The discrepancy between the JH and HEPTopTaggers is more pronounced at higher p_T and larger jet radius (see Figs. 31 and 36). Note that both the JH tagger and the HEPTopTagger are superior to the grooming algorithms at using the W candidate inside of the top for signal discrimination; this is because the the pruning and trimming algorithms do not have inherent W-identification steps and are not optimized for this purpose.

In Figures 28 and 31 we directly compare ROC curves for jet shape observable performance and top mass performance respectively in the three different p_T bins considered whilst keeping the jet radius fixed at R=0.8. The input parameters of the taggers, groomers and shape variables are separately optimized in each p_T bin. One can see from Figure 28 that the tagging performance of jet shapes do not change substantially with p_T. The observables $\tau_{32}^{(\beta=1)}$ and Qjet volatility Γ have the most variation and tend to degrade with higher p_T, as can be seen in Figures 29 and 30). This makes sense, as higher-p_T QCD jets have more, harder emissions within the jet, giving rise to substructure that fakes the signal. By contrast, from Figure 31 we can see that most of the top mass observables have superior performance at higher p_T due to the radiation from the top quark becoming more collimated. The notable exception is the HEPTopTagger, which degrades at higher p_T, likely in part due to the background-shaping effects discussed earlier.

In Figures 32 and 36 we directly compare ROC curves for jet shape observable performance and top mass performance respectively for the three different jet radii considered within the p_T 1.5-1.6 TeV bin. Again, the input parameters of the taggers, groomers and shape variables are separately optimized for each jet radius. We can see from these figures that most of the top tagging variables, both shape and reconstructued top mass, perform best for smaller radius. This is likely because, at such high p_T, most of the radiation from the top quark is confined within $R = 0.4$, and having a larger jet radius makes the observable more susceptible to contamination from the underlying event and other uncorrelated radiation. In Figures 33, 34 and 35, we compare the individual top signal and QCD background distributions for each shape variable considered in the p_T 1.5-1.6 TeV bin for the various jet radii. One can see that the distributions for both signal broaden with increasing R, degrading the discriminating power. For $C_2^{(\beta=1)}$ and $C_3^{(\beta=1)}$, the background distributions are shifted upward as well. Therefore, the discriminating power generally gets worse with increasing R. The

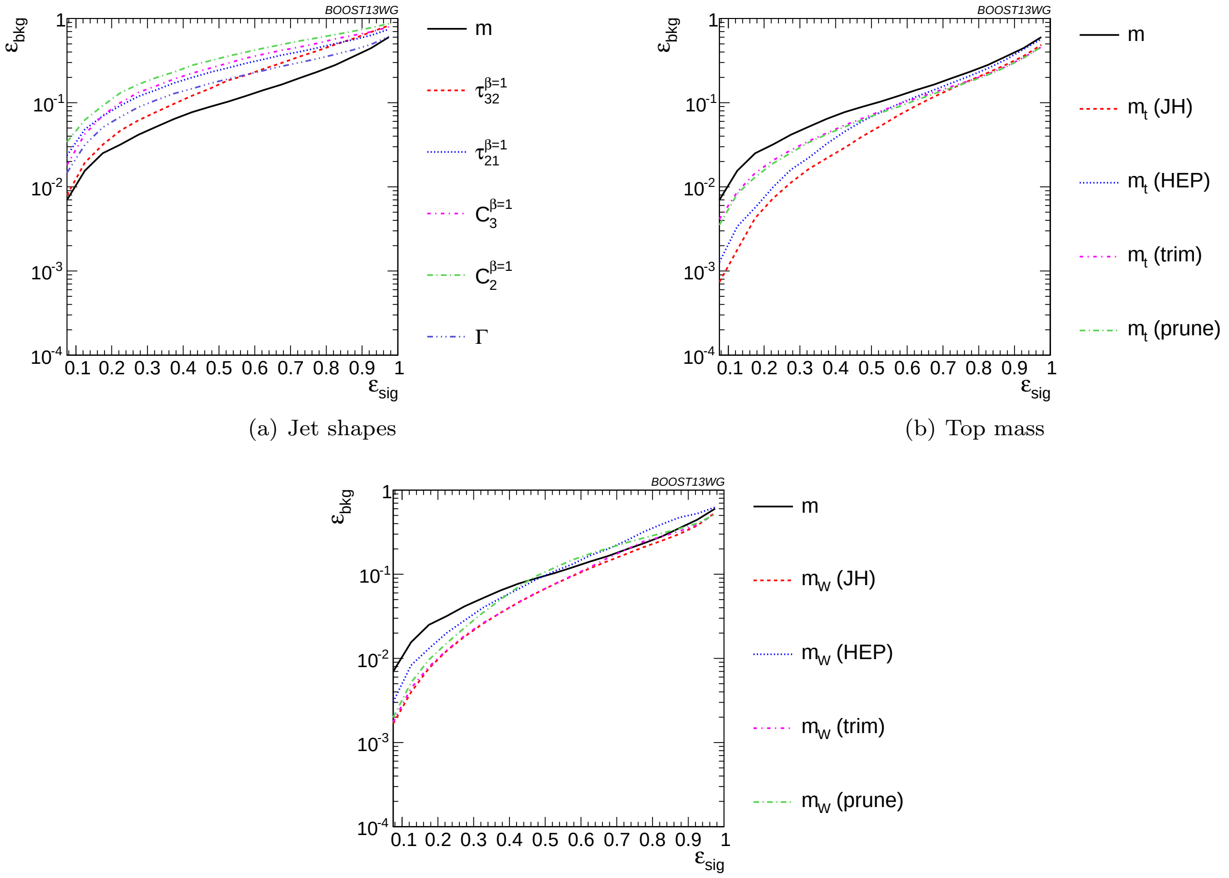

(a) Jet shapes

(b) Top mass

(c) W mass

Fig. 25 Comparison of single-variable top-tagging performance in the $p_T = 1 - 1.1$ GeV bin using the anti-k_T, R=0.8 algorithm.

main exception is for $C_3^{(\beta=1)}$, which performs optimally at $R = 0.8$; in this case, the signal and background coincidentally happen to have the same distribution around $R = 0.4$, and so $R = 0.8$ gives better discrimination. **ED: Should we also include 1-D plots comparing signal vs bkgd in the top mass, and how this varies with radius? Having said that, there a a lot of 1-D plots here already, might want to try and cut down.**

7.3 Performance of multivariable combinations

We now consider various BDT combinations of the observables from Section 7.2, using the techniques described in Section 4. In particular, we consider the performance of individual taggers such as the JH tagger and HEPTopTagger, which output information about the top and W candidate masses and the helicity angle; groomers, such as trimming and pruning, which remove soft, uncorrelated radiation from the top candidate to improve mass reconstruction, and to which we have added a W reconstruction step; and the combination of the outputs of the above taggers/groomers, both with each other, and with shape variables such as N-subjettiness ratios and energy correlation ratios. For all observables with tuneable input parameters, we scan and optimize over realistic values of such parameters, as described in Section 7.1.

In Figure 37, we directly compare the performance of the HEPTopTagger, the JH tagger, trimming, and pruning, in the $p_T = 1 - 1.1$ TeV bin using jet radius R=0.8, where both m_t and m_W are used in the groomers. Generally, we find that pruning, which does not naturally incorporate subjets into the algorithm, does not perform as well as the others. Interestingly, trimming, which does include a subjet-identification step, performs comparably to the HEPTopTagger over much of the range, possibly due to the background-shaping observed in Section 7.2. By contrast, the JH tagger outperforms the other algorithms. To determine whether there is complementary information in the mass outputs from different top taggers, we also consider in Figure 37 a

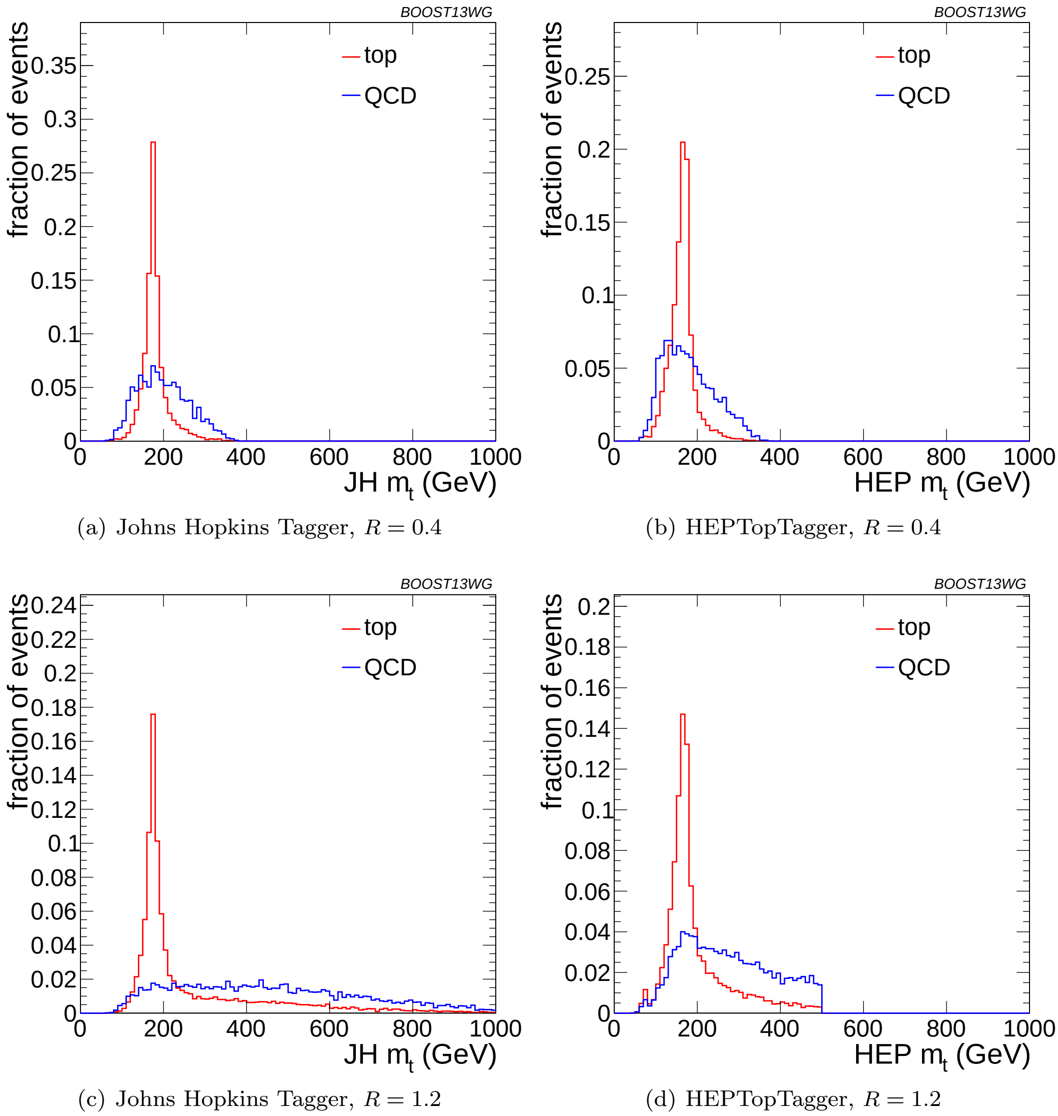

(a) Johns Hopkins Tagger, $R = 0.4$

(b) HEPTopTagger, $R = 0.4$

(c) Johns Hopkins Tagger, $R = 1.2$

(d) HEPTopTagger, $R = 1.2$

Fig. 26 Comparison of top mass reconstruction with the JH and HEPTopTaggers at different R using the anti-k_T algorithm, $p_\mathrm{T} = 1.5-1.6$ TeV. Each histogram is shown for the working point optimized for best performance with m_t in the 0.3−0.35 signal efficiency bin, and is normalized to the fraction of events passing the tagger. In this and subsequent plots, the HEPTopTagger distribution cuts off at 500 GeV because the tagger fails to tag jets with a larger mass.

multivariable combination of all of the JH and HEPTopTagger outputs. The maximum efficiency of the combined JH and HEPTopTaggers is limited, as some fraction of signal events inevitably fails either one or other of the taggers. We do see a 20-50% improvement in performance when combining all outputs, which suggests that the different algorithms used to identify the top and W for different taggers contains complementary information.

In Figure 38 we present the results for multivariable combinations of the top tagger outputs with and without shape variables. We see that, for both the HEPTopTagger and the JH tagger, the shape observables contain additional information uncorrelated with the masses and helicity angle, and give on average a factor 2-3 improvement in signal discrimination. We see that, when combined with the tagger outputs, both the energy correlation functions $C_2 + C_3$ and the N-subjettiness ratios $\tau_{21} + \tau_{32}$ give comparable performance, while the Qjet mass volatility is slightly worse; this is unsurprising, as Qjets accesses shape information in a more indirect way from other shape observables. Combining all shape observables with a single top tagger provides even greater enhancement in discrimination power. We directly compare the performance of the JH and HEPTopTaggers in Figure 38(c). Combin-

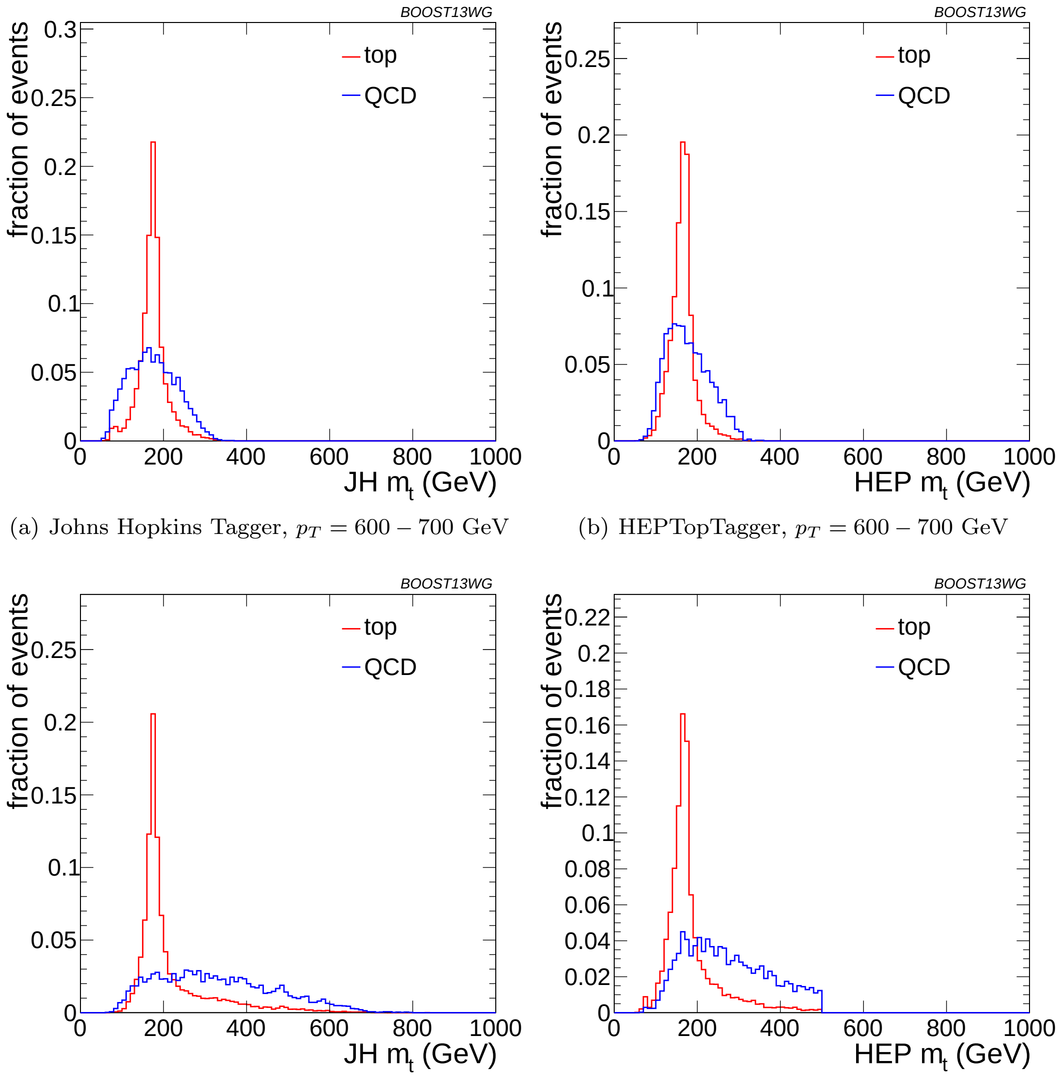

(a) Johns Hopkins Tagger, $p_T = 600 - 700$ GeV (b) HEPTopTagger, $p_T = 600 - 700$ GeV

(c) Johns Hopkins Tagger, $p_T = 1.5 - 1.6$ TeV (d) HEPTopTagger, $p_T = 1.5 - 1.6$ TeV

Fig. 27 Comparison of top mass reconstruction with the JH and HEPTopTaggers at different p_T using the anti-k_T algorithm, $R = 0.8$. Each histogram is shown for the working point optimized for best performance with m_t in the $0.3 - 0.35$ signal efficiency bin, and is normalized to the fraction of events passing the tagger.

ing the taggers with shape information nearly erases the difference between the tagging methods observed in Figure 37; this indicates that combining the shape information with the HEPTopTagger identifies the differences between signal and background missed by the tagger alone. This also suggests that further improvement to discriminating power may be minimal, as various multivariable combinations are converging to within a factor of 20% or so.

In Figure 39 we present the results for multivariable combinations of groomer outputs with and without shape variables. As with the tagging algorithms, combinations of groomers with shape observables improves their discriminating power; combinations with $\tau_{32} + \tau_{21}$ perform comparably to those with $C_3 + C_2$, and both of these are superior to combinations with the mass volatility, Γ. Substantial improvement is further possible by combining the groomers with all shape observables. Not surprisingly, the taggers that lag behind in performance enjoy the largest gain in signal-background discrimination with the addition of shape observables. Once again, in Figure 39(c), we find that the differences between pruning and trimming are erased when combined with shape information.

Finally, in Figure 40, we compare the performance of each of the tagger/groomers when their outputs are combined with all of the shape observables considered. One can see that the discrepancies between the perfor-

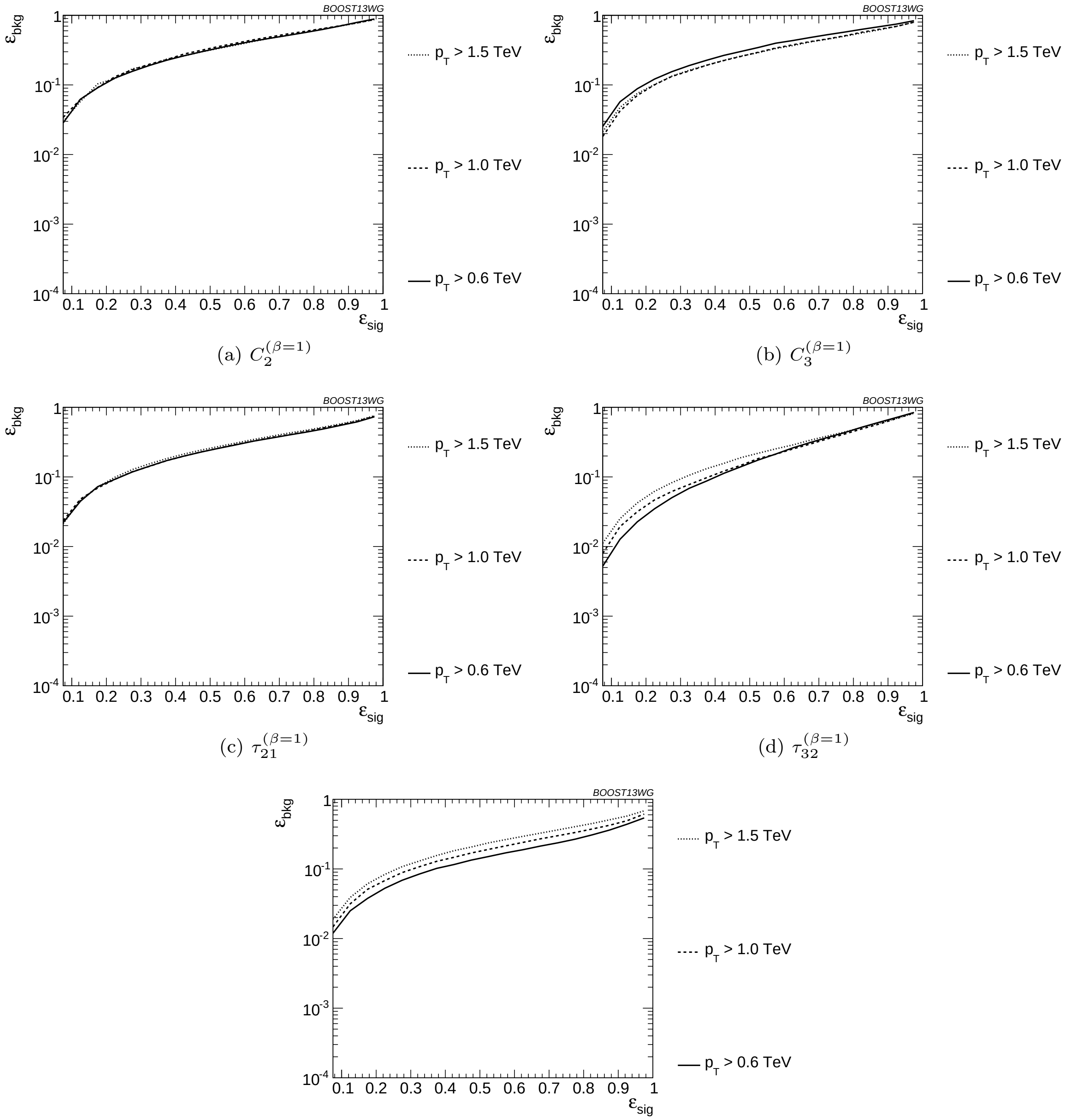

(a) $C_2^{(\beta=1)}$

(b) $C_3^{(\beta=1)}$

(c) $\tau_{21}^{(\beta=1)}$

(d) $\tau_{32}^{(\beta=1)}$

(e) Qjet mass volatility

Fig. 28 Comparison of individual jet shape performance at different p_T using the anti-k_{T} R=0.8 algorithm.

mance of the different taggers/groomers all but vanishes, suggesting perhaps that we are here utilising all available signal-background discrmination information, and that this is the optimal top tagging performance that could be achieved in these conditions.

Up to this point we have just considered the combined multivariable performance in the p_T 1.0-1.1 TeV bin with jet radius R=0.8. We now compare the BDT combinations of tagger outputs, with and without shape variables, at different p_T. The taggers are optimized over all input parameters for each choice of p_T and signal efficiency. As with the single-variable study, we consider anti-k_{T} jets clustered with $R = 0.8$ and compare the outcomes in the $p_T = 500-600$ GeV, $p_T = 1-1.1$ TeV, and $p_T = 1.5-1.6$ TeV bins. The comparison of the taggers/groomers is shown in Figure 41. The be-

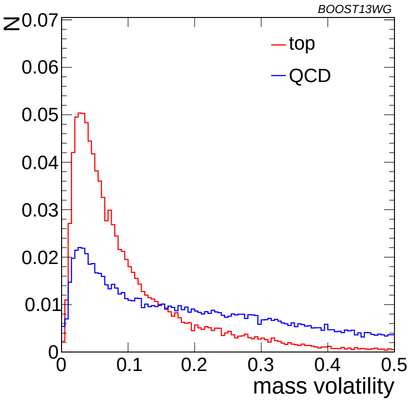

(a) $\Gamma_{\rm Qjet}$, $p_T = 600 - 700$ GeV

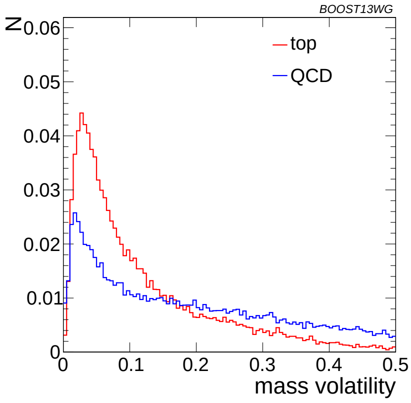

(b) $\Gamma_{\rm Qjet}$, $p_T = 1 - 1.1$ TeV

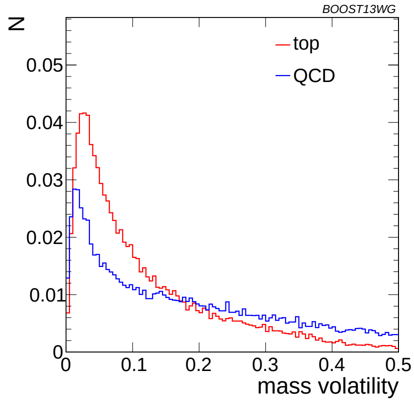

(c) $\Gamma_{\rm Qjet}$, $p_T = 1.5 - 1.6$ TeV

Fig. 29 Comparison of $\Gamma_{\rm Qjet}$ at $R = 0.8$ and different values of the p_T.

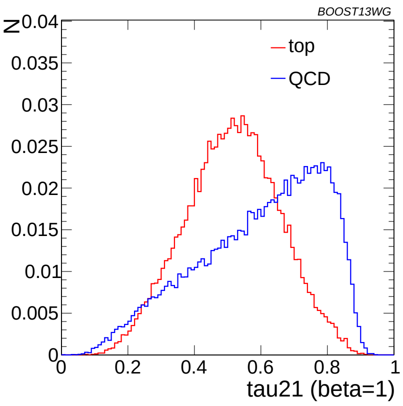

(a) $\tau_{21}^{(\beta=1)}$, $p_T = 600 - 700$ GeV

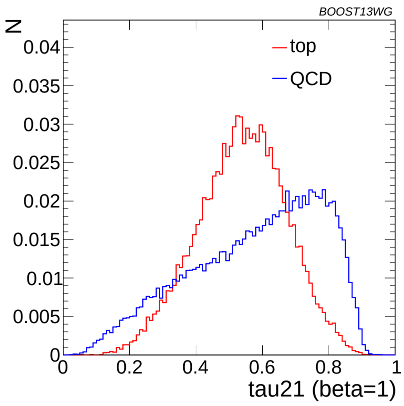

(b) $\tau_{21}^{(\beta=1)}$, $p_T = 1 - 1.1$ TeV

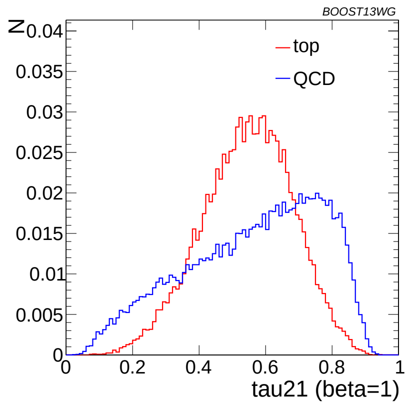

(c) $\tau_{21}^{(\beta=1)}$, $p_T = 1.5 - 1.6$ TeV

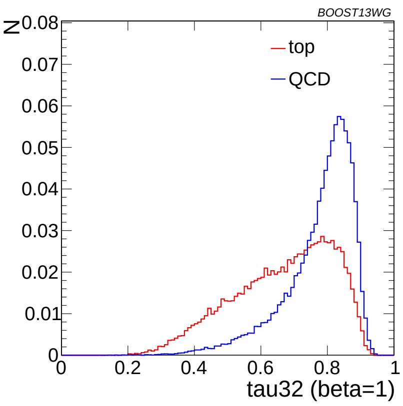

(d) $\tau_{32}^{(\beta=1)}$, $p_T = 600 - 700$ GeV

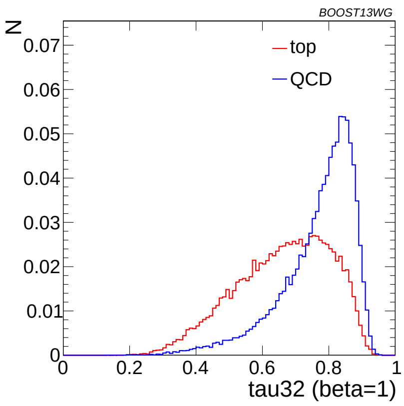

(e) $\tau_{32}^{(\beta=1)}$, $p_T = 1 - 1.1$ TeV

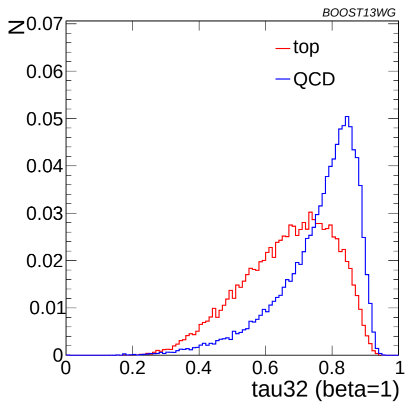

(f) $\tau_{32}^{(\beta=1)}$, $p_T = 1.5 - 1.6$ TeV

Fig. 30 Comparison of $\tau_{21}^{\beta=1}$ and $\tau_{32}^{\beta=1}$ with $R = 0.8$ and different values of the p_T.

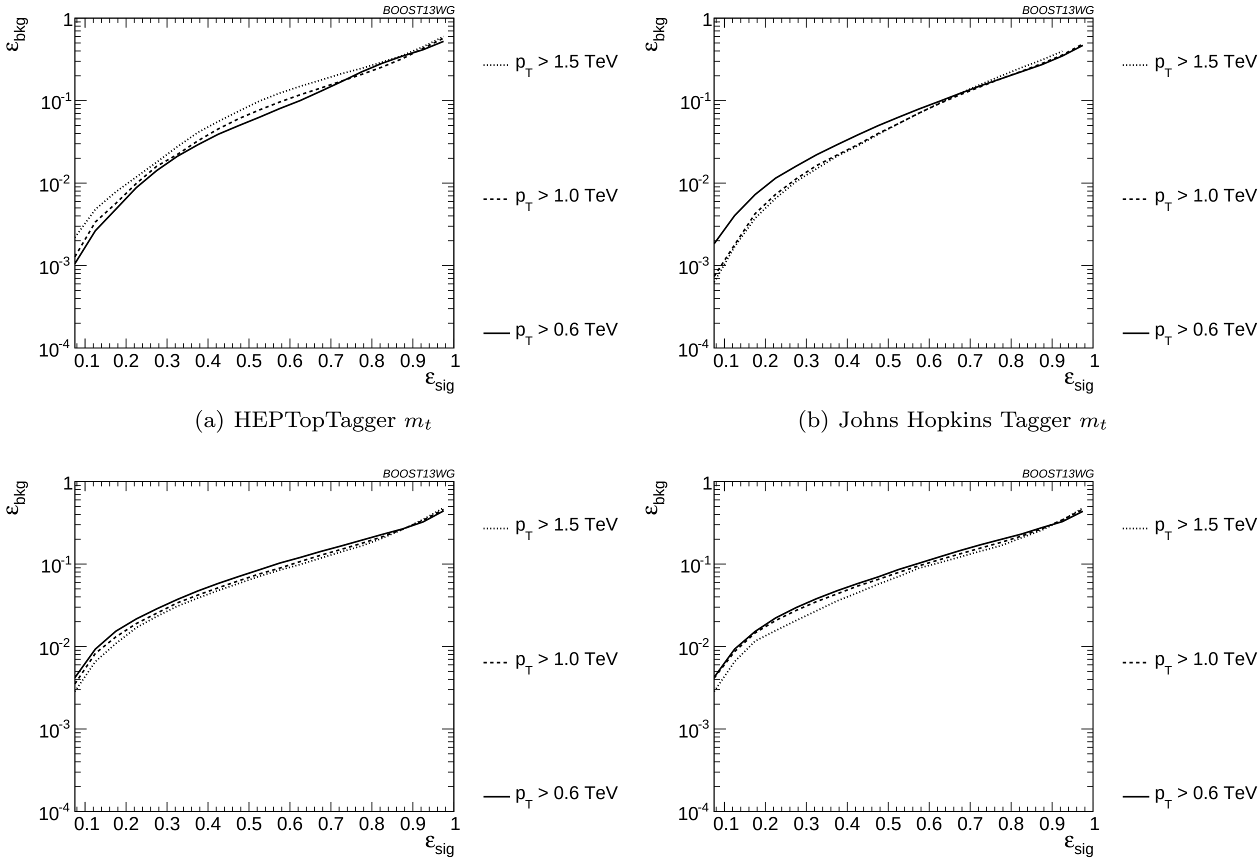

(a) HEPTopTagger m_t (b) Johns Hopkins Tagger m_t

(c) Pruning m_t (d) Trimming m_t

Fig. 31 Comparison of top mass performance of different taggers at different p_T using the anti-k_T R=0.8 algorithm.

haviour with p_T is qualitatively similar to the behaviour of the $m_t$observable for each tagger/groomer shown in Figure 31; this suggests that the p_T behaviour of the taggers is dominated by the top mass reconstruction. As before, the HEPTopTagger performance degrades slightly with increased p_T due to the background shaping effect, while the JH tagger and groomers modestly improve in performance.

In Figure 42, we show the p_T dependence of BDT combinations of the JH tagger output combined with shape observables. We find that the curves look nearly identical: the p_T dependence is dominated by the top mass reconstruction, and combining the tagger outputs with different shape observables does not substantially change this behaviour. The same holds true for trimming and pruning. By contrast, HEPTopTagger ROC curves, shown in Figure 43, do change somewhat when combined with different shape observables; due to the suboptimal performance of the HEPTopTagger at high p_T , we find that combining the HEPTopTagger with $C_3^{(\beta=1)}$, which in Figure 28(b) is seen to have some modest improvement at high p_T , can improve its performance. Combining the HEPTopTagger with multiple shape observables gives the maximum improvement in performance at high p_T relative to at low p_T .

In Figure 44 we compare the BDT combinations of tagger outputs, with and without shape variables, at different jet radius R in the $p_T = 1.5-1.6$ TeV bin. The taggers are optimized over all input parameters for each choice of R and signal efficiency. We find that, for all taggers and groomers, the performance is always best at small R; the choice of R is sufficiently large to admit the full top quark decay at such high p_T , but is small enough to suppress contamination from additional radiation. This is not altered when the taggers are combined with shape observable. For example, in Figure 45 is shown the depedence on R of the JH tagger when combined with shape observables, where one can see that the R-dependence is identical for all combinations. The same holds true for the HEPTopTagger, trimming, and pruning.

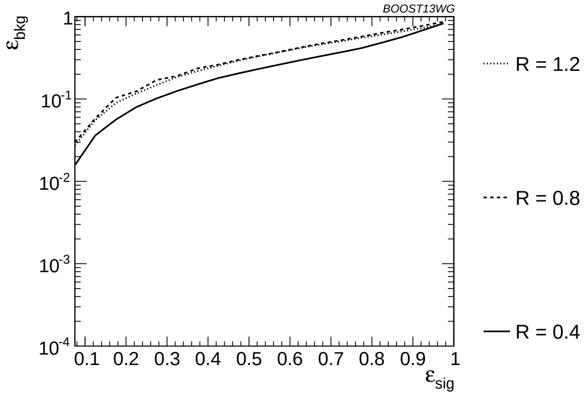

(a) $C_2^{(\beta=1)}$

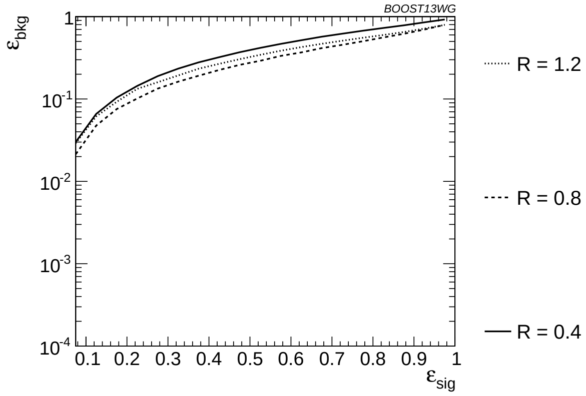

(b) $C_3^{(\beta=1)}$

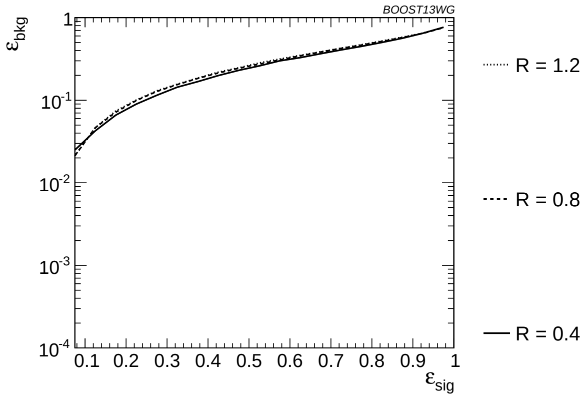

(c) $\tau_{21}^{(\beta=1)}$

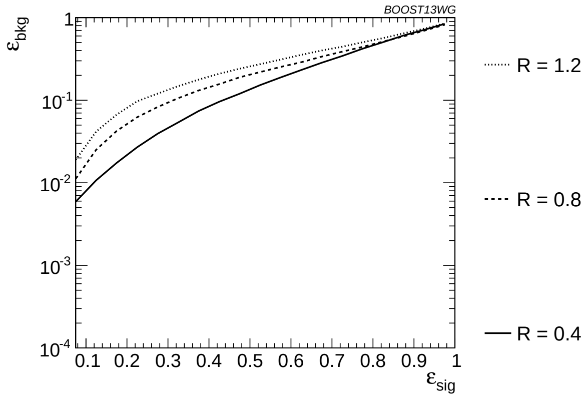

(d) $\tau_{32}^{(\beta=1)}$

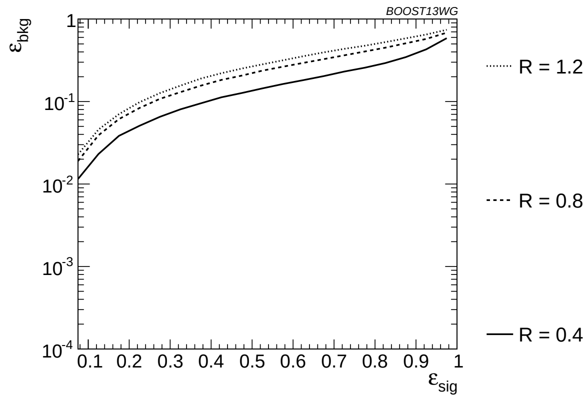

(e) Qjet mass volatility

Fig. 32 Comparison of individual jet shape performance at different R in the $p_T = 1.5 - 1.6$ TeV bin.

7.4 Performance at Sub-Optimal Working Points

Up until now, we have re-optimized our tagger and groomer parameters for each p_T, R, and signal efficiency working point. In reality, experiments will choose a finite set of working points to use. How do our results hold up when this is taken into account? To address this concern, we replicate our analyses, but only optimize the top taggers for a particular $p_T/R/$efficiency and apply the same parameters to other scenarios. This allows us to determine the extent to which re-optimization is necessary to maintain the high signal-background discrimination power seen in the top tagging algorithms we study. The shape observables typically do not have any input parameters to optimize. Therefore, we focus

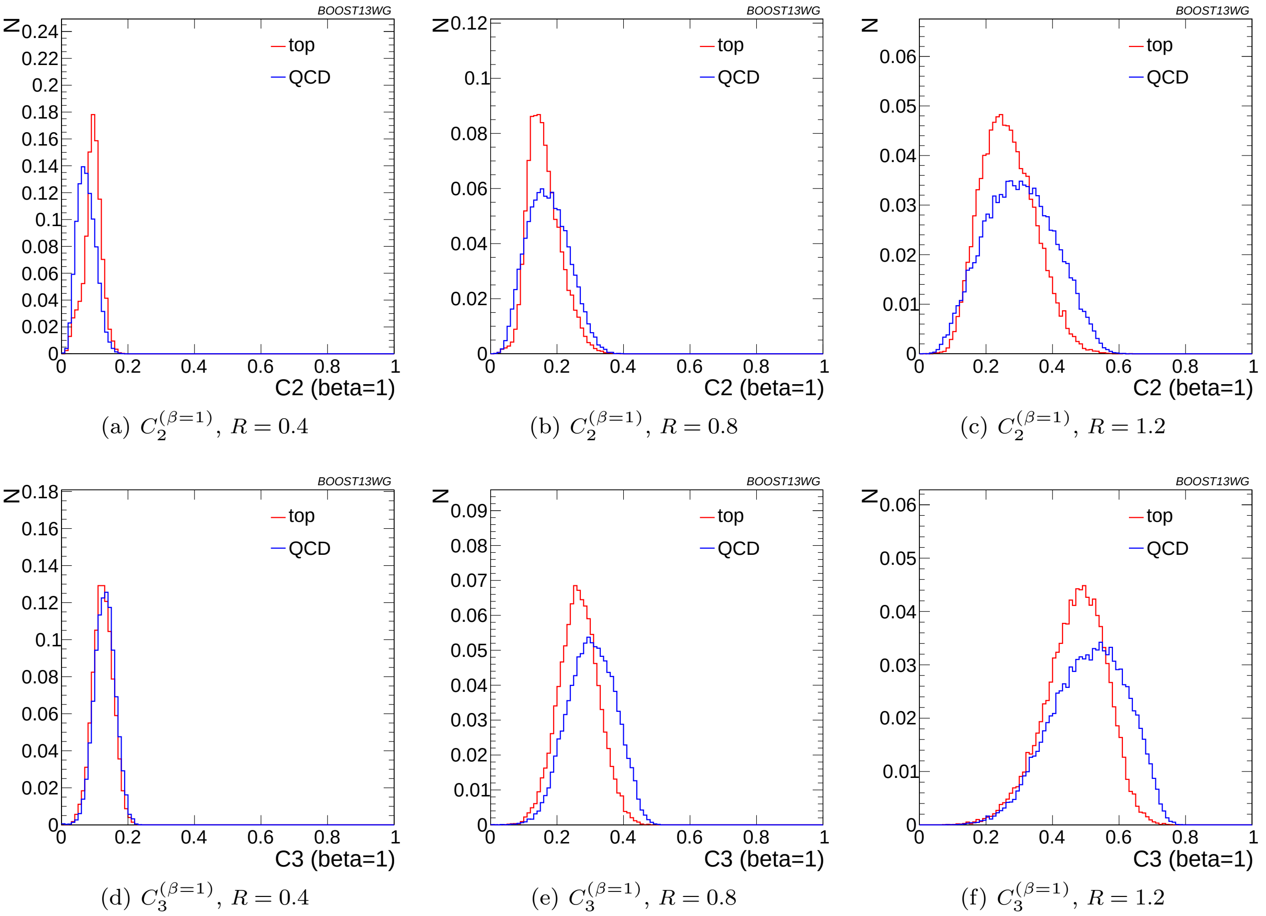

(a) $C_2^{(\beta=1)}$, $R = 0.4$ (b) $C_2^{(\beta=1)}$, $R = 0.8$ (c) $C_2^{(\beta=1)}$, $R = 1.2$

(d) $C_3^{(\beta=1)}$, $R = 0.4$ (e) $C_3^{(\beta=1)}$, $R = 0.8$ (f) $C_3^{(\beta=1)}$, $R = 1.2$

Fig. 33 Comparison of $C_2^{\beta=1}$ and $C_3^{\beta=1}$ in the $p_T = 1.5 - 1.6$ TeV bin and different values of the anti-k_T radius R.

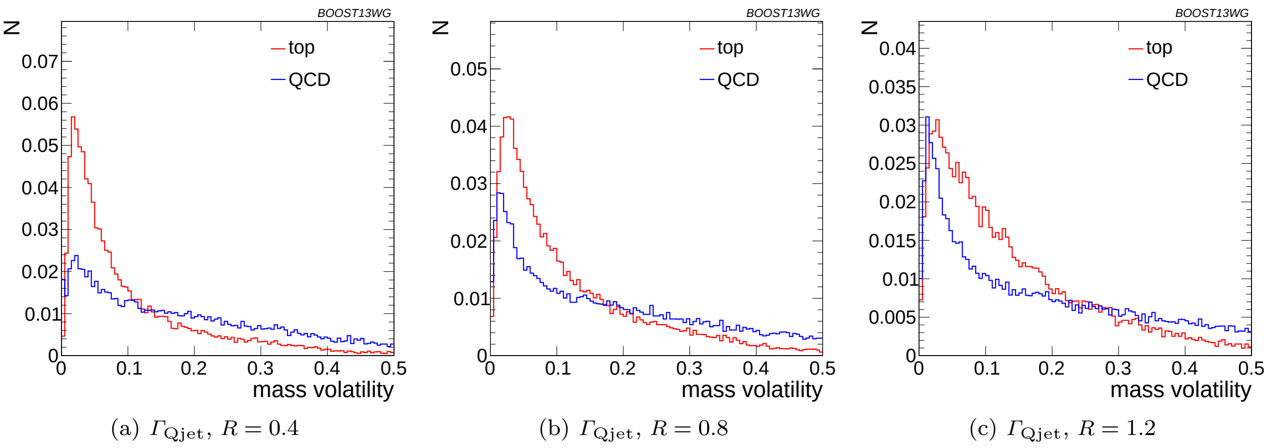

(a) Γ_{Qjet}, $R = 0.4$ (b) Γ_{Qjet}, $R = 0.8$ (c) Γ_{Qjet}, $R = 1.2$

Fig. 34 Comparison of Γ_{Qjet} in the $p_T = 1.5 - 1.6$ TeV bin and different values of the anti-k_T radius R.

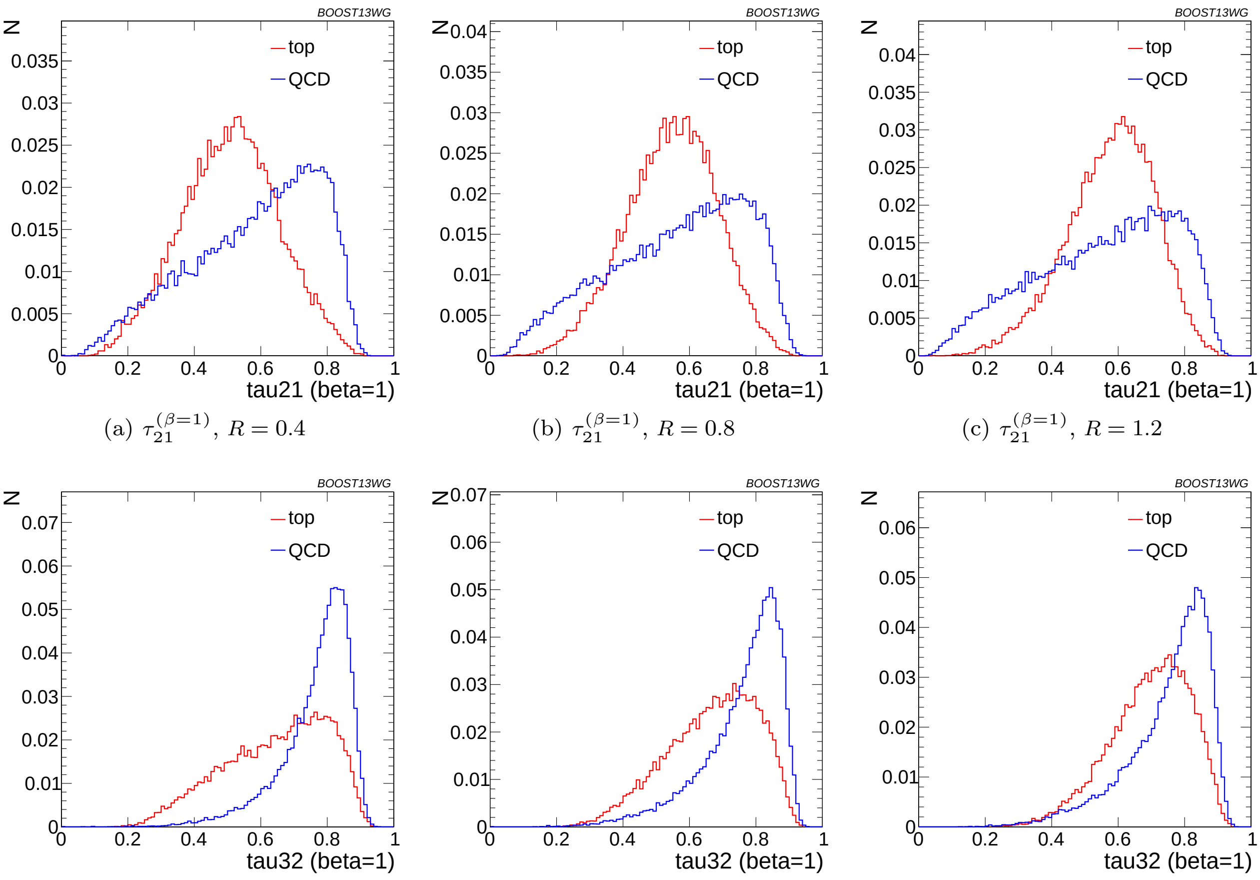

(a) $\tau_{21}^{(\beta=1)}$, $R = 0.4$ (b) $\tau_{21}^{(\beta=1)}$, $R = 0.8$ (c) $\tau_{21}^{(\beta=1)}$, $R = 1.2$

(d) $\tau_{32}^{(\beta=1)}$, $R = 0.4$ (e) $\tau_{32}^{(\beta=1)}$, $R = 1.8$ (f) $\tau_{32}^{(\beta=1)}$, $R = 1.2$

Fig. 35 Comparison of $\tau_{21}^{\beta=1}$ and $\tau_{32}^{\beta=1}$ in the $p_T = 1.5 - 1.6$ TeV bin and different values of the anti-k_{T} radius R.

on the taggers and groomers, and their combination with shape observables, in this section.

Optimizing at a single p_T : We show in Figure 46 the performance of the top taggers, using just the reconstructed top mass as the discriminating variable, with all input parameters optimized to the $p_T = 1.5 - 1.6$ TeV bin, relative to the performance optimized at each p_T. We see that while the performance degrades by about 50% when the high-p_T optimized points are used at other momenta, this is only an $O(1)$ adjustment of the tagger performance **ED: what does $O(1)$ mean?**, with trimming and the Johns Hopkins tagger degrading the most. The jagged behaviour of the points is due to the finite resolution of the scan. We also observe a particular effect associated with using suboptimal taggers: since taggers sometimes fail to return a top candidate, parameters optimized for a particular efficiency ε_S at $p_T = 1.5 - 1.6$ TeV may not return enough signal candidates to reach the same efficiency at a different p_T. Consequently, no point appears for that p_T value. This is not often a practical concern, as the largest gains in signal discrimination and significance are for smaller values of ε_S, but it is something that must be considered when selecting benchmark tagger parameters and signal efficiencies.

The degradation in performance is more pronounced for the BDT combinations of the full tagger outputs, shown in Figure 47), particularly at very low signal efficiency where the optimization picks out a cut on the tail of some distribution that depends precisely on the p_T/R of the jet. Once again, trimming and the Johns Hopkins tagger degrade more markedly. Similar behaviour holds for the BDT combinations of tagger outputs plus all shape observables.

Optimizing at a single R: We perform a similar analysis, optimizing tagger parameters for each signal efficiency at $R = 1.2$, and then use the same parameters for smaller R, in the p_T 1.5-1.6 TeV bin. In Figure 48 we show the ratio of the performance of the top taggers, using just the reconstructed top mass as the discriminating variable, with all input parameters

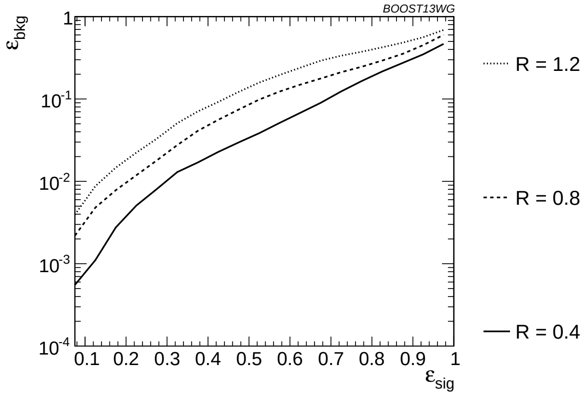

(a) HEPTopTagger m_t

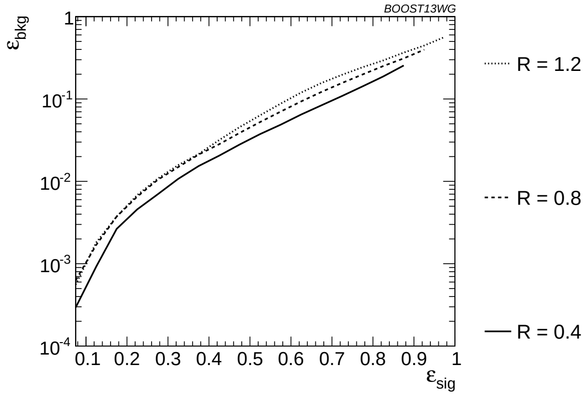

(b) Johns Hopkins Tagger m_t

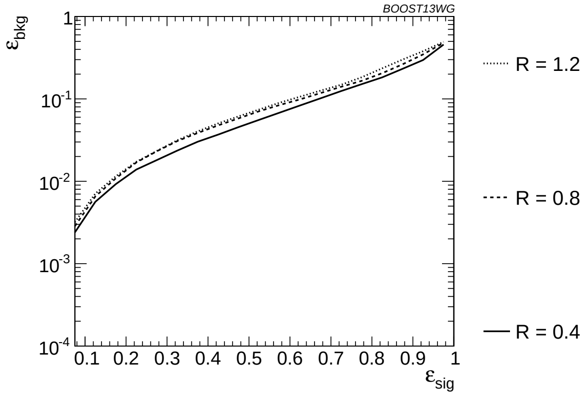

(c) Pruning m_t

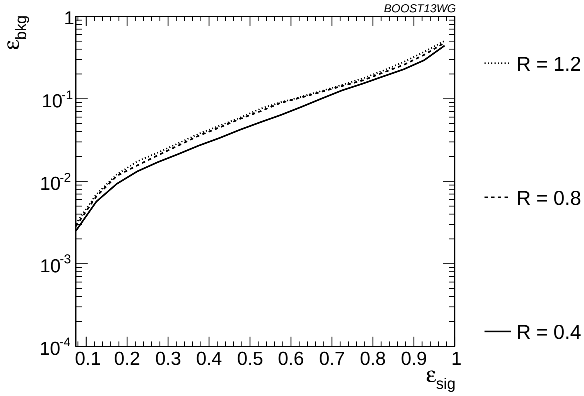

(d) Trimming m_t

Fig. 36 Comparison of top mass performance of different taggers at different R in the $p_T = 1.5 - 1.6$ TeV bin.

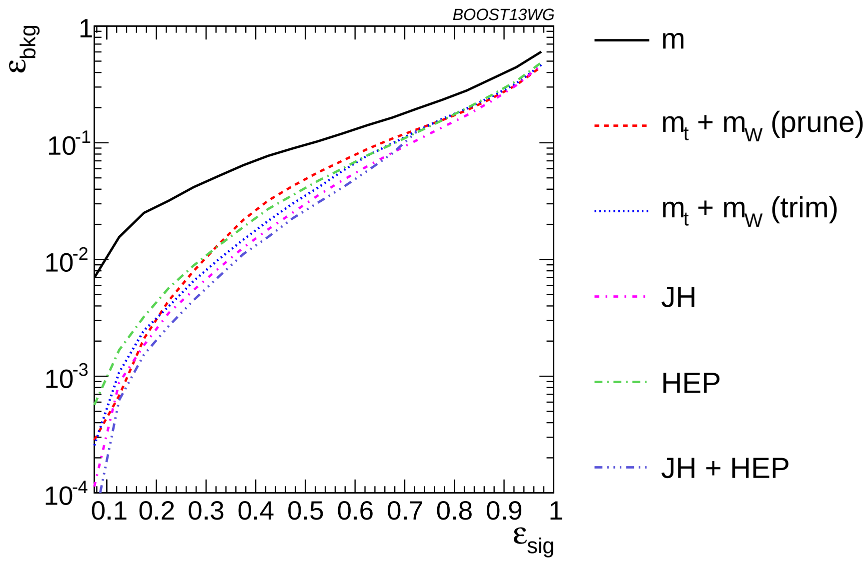

Fig. 37 The performance of the various taggers in the $p_T = 1 - 1.1$ TeV bin using the anti-k_T R=0.8 algorithm. For the groomers a BDT combination of the reconstructed $m_t$and $m_W$are used. Also shown is a multivariable combination of all of the JH and HEPTopTagger outputs. The ungroomed mass performance is shown for comparison.

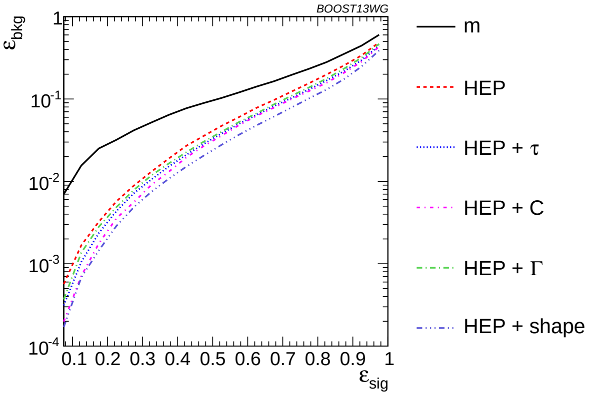

(a) HEPTopTagger + Shape

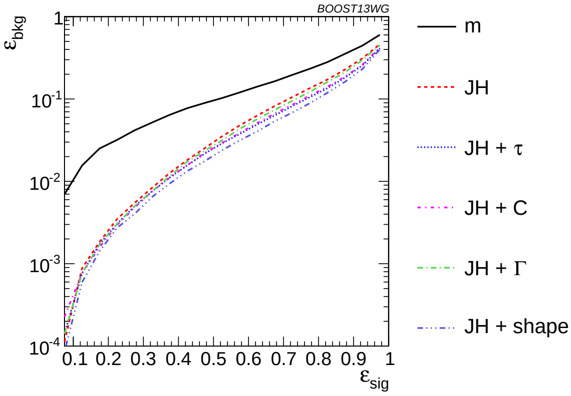

(b) Johns Hopkins Tagger + shape

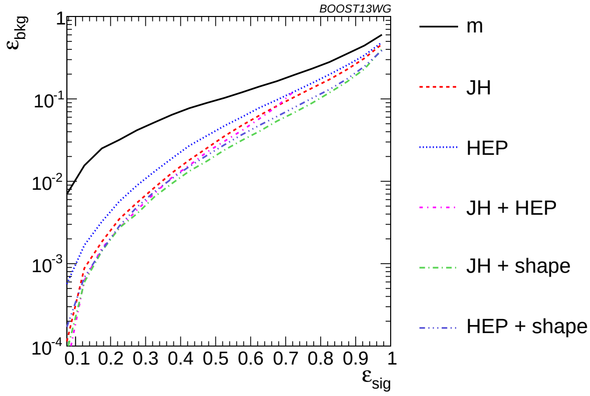

(c) HEP vs. JH comparison (incl. shape)

Fig. 38 The performance of BDT combinations of the JH and HepTopTagger outputs with various shape observables in the $p_T = 1 - 1.1$ TeV bin using the anti-k_{T} R=0.8 algorithm. Taggers are combined with the following shape observables: $\tau_{21}^{(\beta=1)} + \tau_{32}^{(\beta=1)}$, $C_2^{(\beta=1)} + C_3^{(\beta=1)}$, Γ_{Qjet}, and all of the above (denoted "shape").

optimized to the $R = 1.2$ values compared to input parameters optimized separately at each radius. While the performance of each observable degrades at small ϵ_{sig} compared to the optimized search, the HEPTopTagger fares the worst as the observed is quite sensitive to the selected value of R. It is not surprising that a tagger whose top mass reconstruction is susceptible to background-shaping at large R and p_T would require a more careful optimization of parameters to obtain the best performance.

The same holds true for the BDT combinations of the full tagger outputs, shown in Figure 49). The performance for the sub-optimal taggers is still within an $O(1)$ factor of the optimized performance, and the HEPTopTagger performs better with the combination of all of its outputs relative to the performance with just m_t. The same behaviour holds for the BDT combinations of tagger outputs and shape observables.

Optimizing at a single efficiency: The strongest assumption we have made so far is that the taggers can be reoptimized for each signal efficiency point. This is useful for making a direct comparison of the power of different top tagging algorithms, but is not particularly practical for the LHC analyses. We now consider the effects when the tagger inputs are optimized once, in the $\varepsilon_S = 0.3 - 0.35$ bin, and then used to determine the full ROC curve. We do this in the $p_T 1 - 1.1$ TeV bin and with $R = 0.8$.

The performance of each tagger, normalized to its performance optimized in each bin, is shown in Figure 50 for cuts on the top mass and W mass, and in Figure 51 for BDT combinations of tagger outputs and shape variables. In both plots, it is apparent that optimizing the taggers in the 0.3-0.35 efficiency bin gives comparable performance over efficiencies ranging from 0.2-0.5, although performance degrades at small and large signal efficiencies. Pruning appears to give especially robust signal-background discrimination without

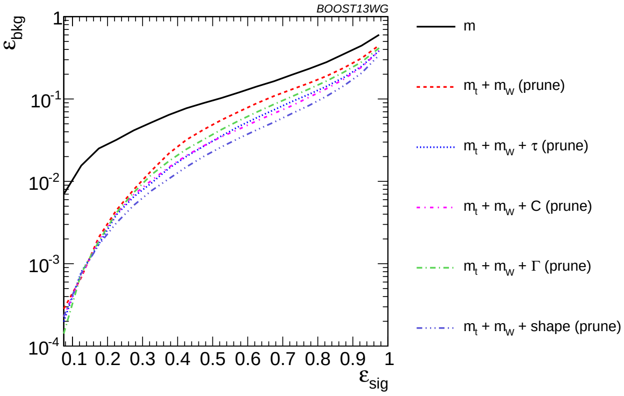

(a) Pruning + Shape

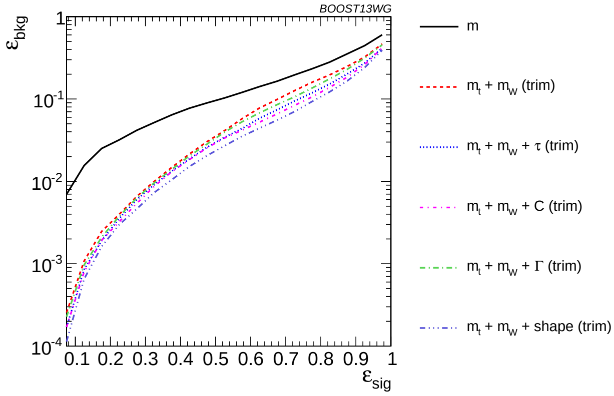

(b) Trimming + Shape

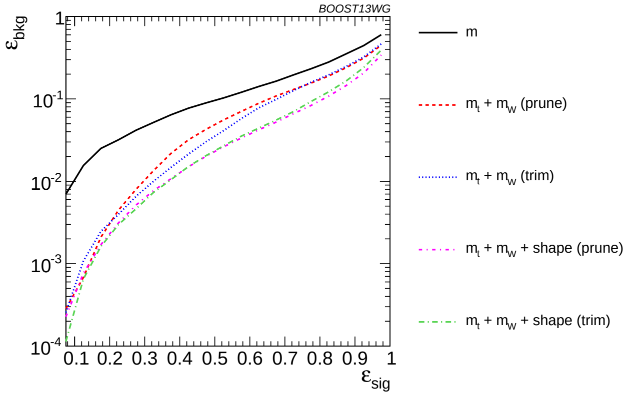

(c) Trim vs. Prune comparison (incl. shape)

Fig. 39 The performance of the BDT combinations of the trimming and pruning outputs with various shape observables in the $p_T = 1 - 1.1$ TeV bin using the anti-k_T R=0.8 algorithm. Groomer mass outputs are combined with the following shape observables: $\tau_{21}^{(\beta=1)} + \tau_{32}^{(\beta=1)}$, $C_2^{(\beta=1)} + C_3^{(\beta=1)}$, $\Gamma_{\rm Qjet}$, and all of the above (denoted "shape").

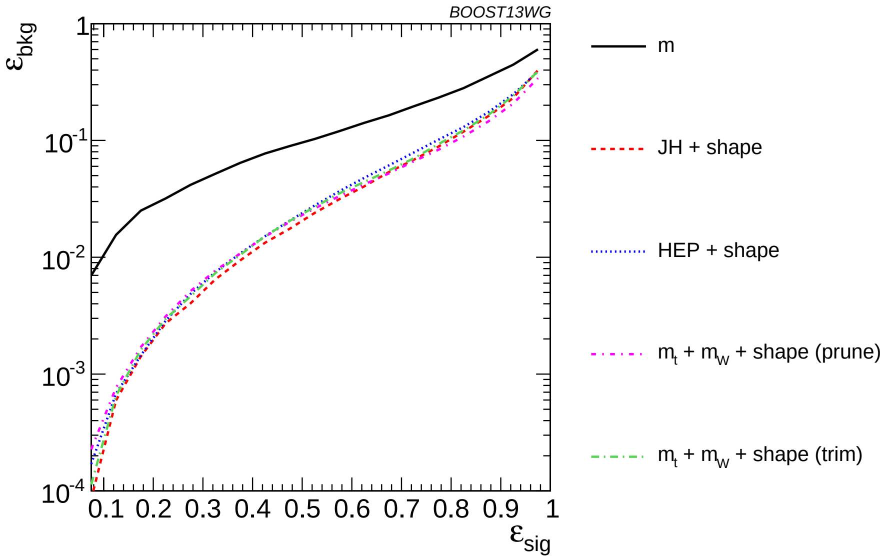

Fig. 40 Comparison of the performance of the BDT combinations of all the groomer/tagger outputs with all the available shape observables in the $p_T = 1 - 1.1$ TeV bin using the anti-k_T R=0.8 algorithm. Tagger/groomer outputs are combined with all of the following shape observables: $\tau_{21}^{(\beta=1)} + \tau_{32}^{(\beta=1)}$, $C_2^{(\beta=1)} + C_3^{(\beta=1)}$, $\Gamma_{\rm Qjet}$.

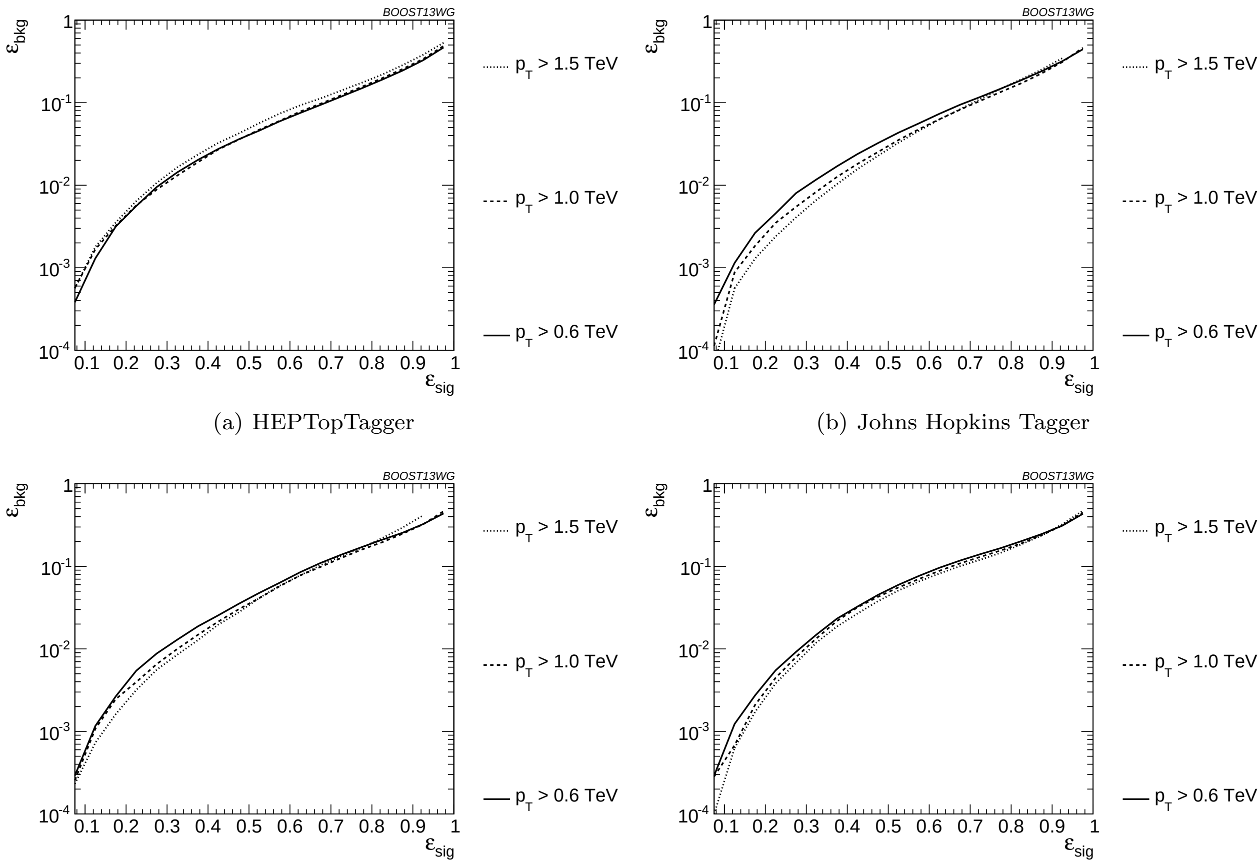

(a) HEPTopTagger (b) Johns Hopkins Tagger

(c) Trimming (d) Pruning

Fig. 41 Comparison of BDT combination of tagger performance at different p_T using the anti-k_T R=0.8 algorithm.

re-optimization, possibly due to the fact that there are no absolute distance or p_T scales that appear in the algorithm. Figures 50 and 51 suggest that, while optimization at all signal efficiencies is a useful tool for comparing different algorithms, it is not crucial to achieve good top-tagging performance in experiments.

7.5 Conclusions

ED: Conclusions to be added

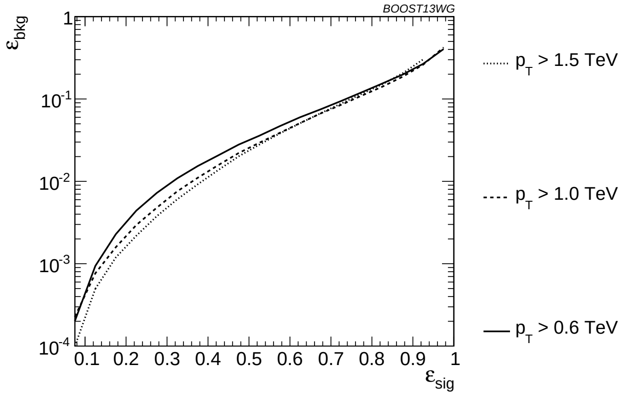

(a) JH+$C_2^{(\beta=1)}$+$C_3^{(\beta=1)}$

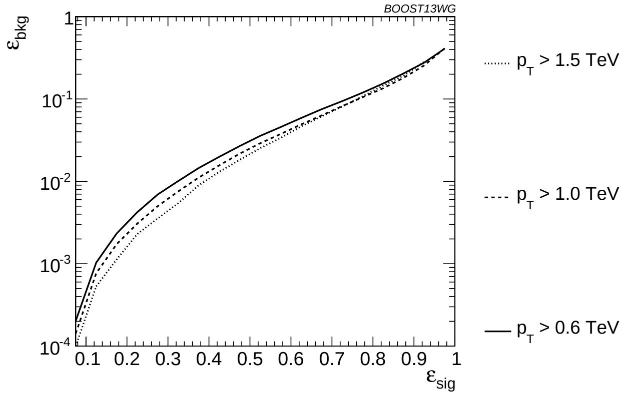

(b) JH+$\tau_{21}^{(\beta=1)}$+$\tau_{32}^{(\beta=1)}$

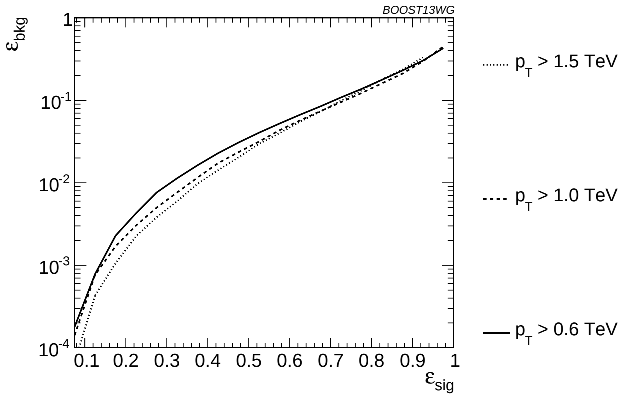

(c) JH + Qjet mass volatility

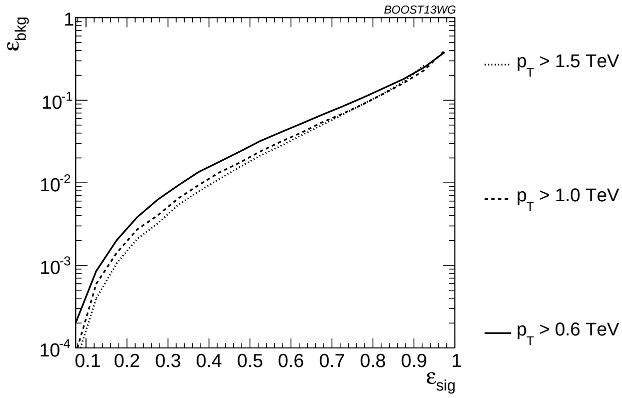

(d) JH + all

Fig. 42 Comparison of BDT combination of JH tagger + shape at different p_T using the anti-k_T R=0.8 algorithm.

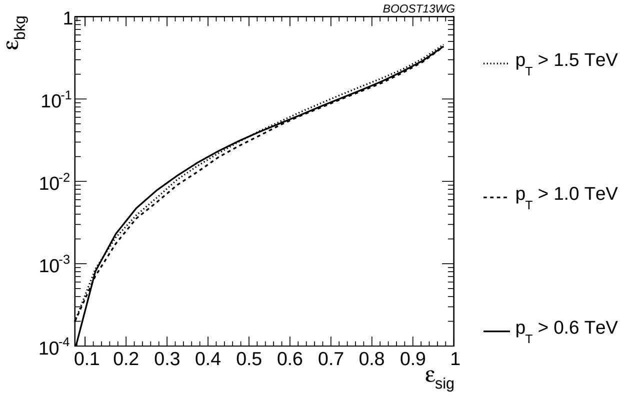

(a) HEP+$C_2^{(\beta=1)}$+$C_3^{(\beta=1)}$

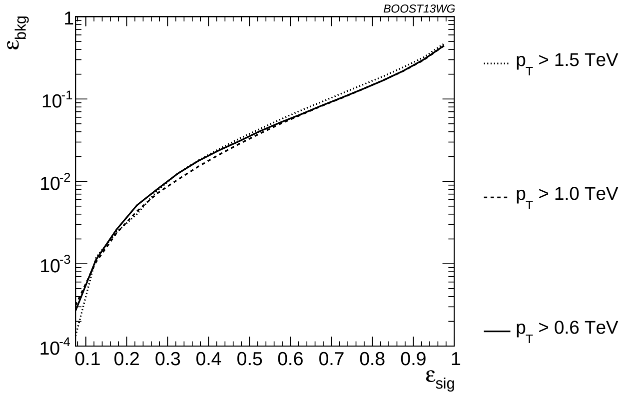

(b) HEP+$\tau_{21}^{(\beta=1)}$+$\tau_{32}^{(\beta=1)}$

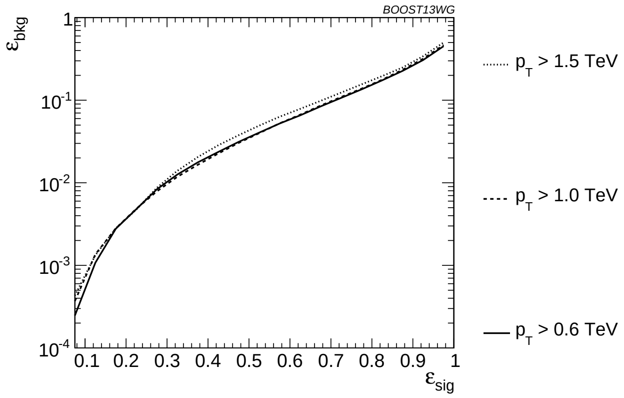

(c) HEP + Qjet mass volatility

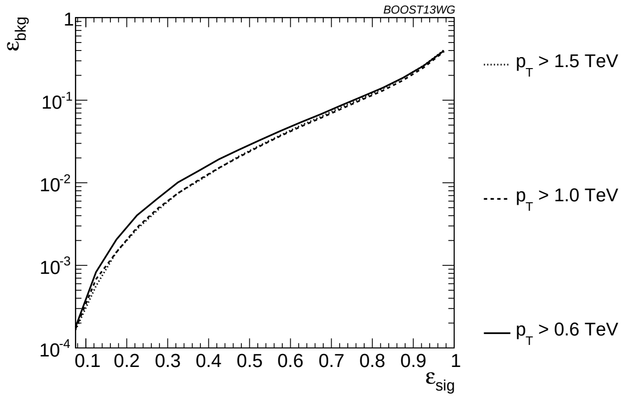

(d) HEP + all

Fig. 43 Comparison of BDT combination of HEP tagger + shape at different p_T using the anti-k_{T} R=0.8 algorithm.

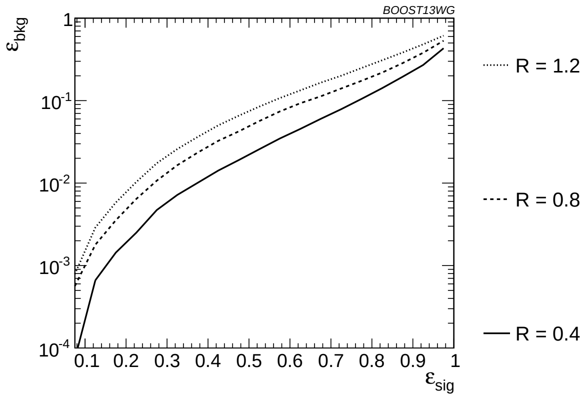

(a) HEPTopTagger

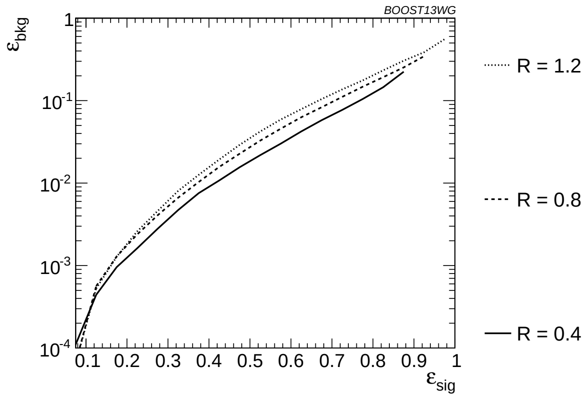

(b) Johns Hopkins Tagger

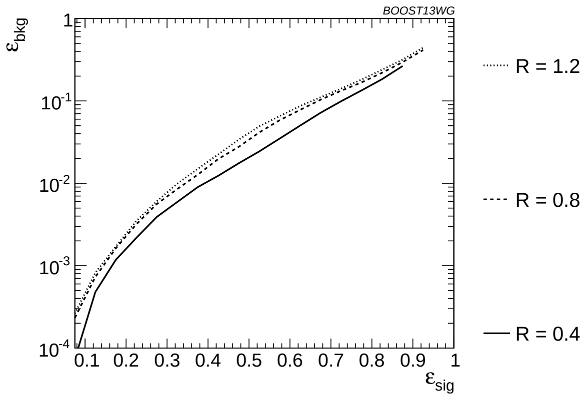

(c) Trimming

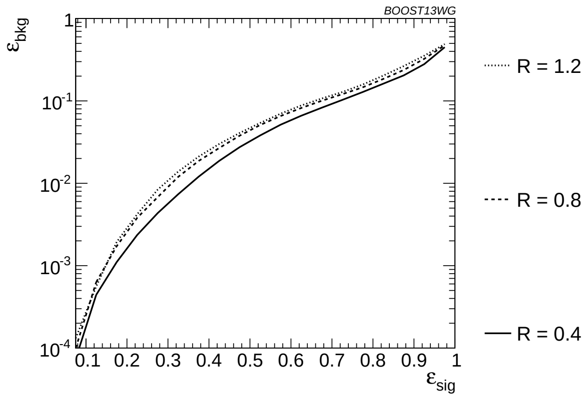

(d) Pruning

Fig. 44 Comparison of tagger and jet shape performance at different radius at p_T = 1.5-1.6 TeV.

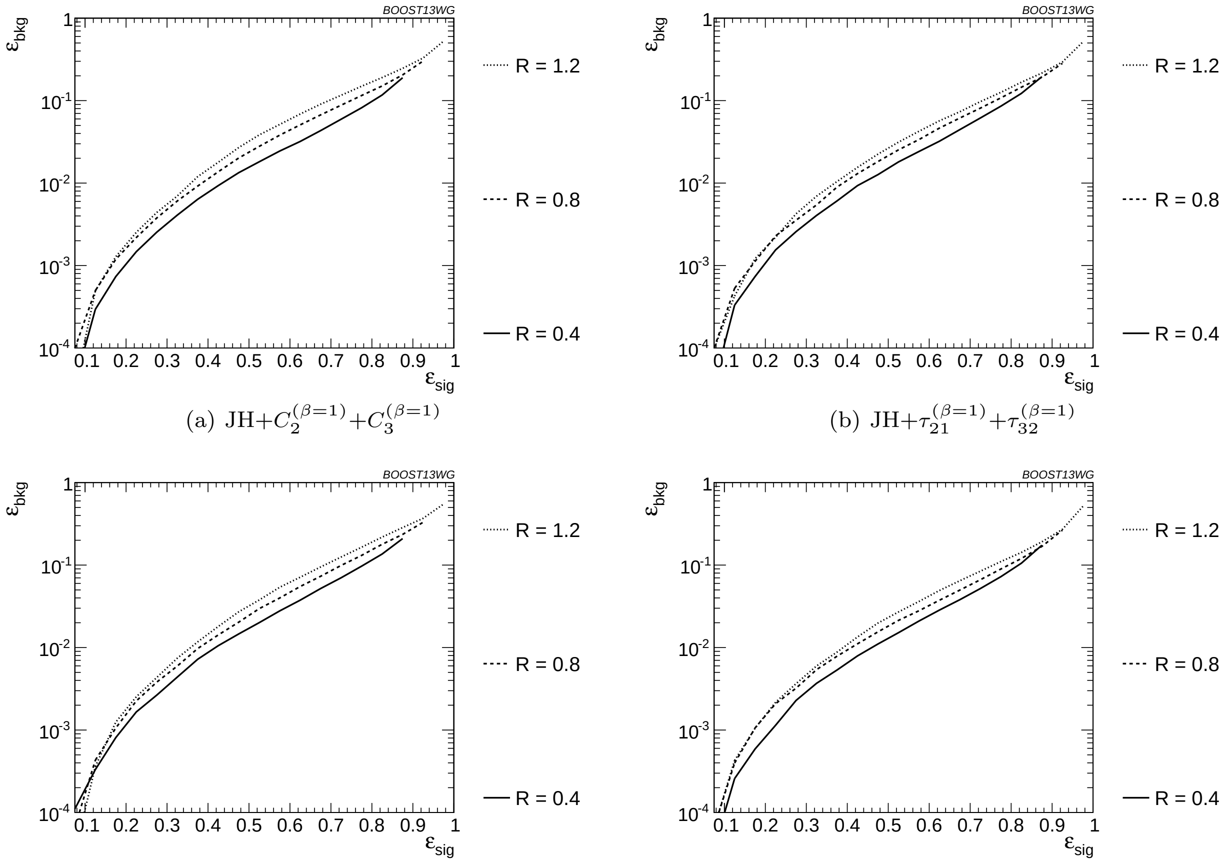

(a) JH+$C_2^{(\beta=1)}$+$C_3^{(\beta=1)}$

(b) JH+$\tau_{21}^{(\beta=1)}$+$\tau_{32}^{(\beta=1)}$

(c) JH + Qjet mass volatility

(d) JH + all

Fig. 45 Comparison of BDT combination of JH tagger + shape at different radius at p_T = 1.5-1.6 TeV.

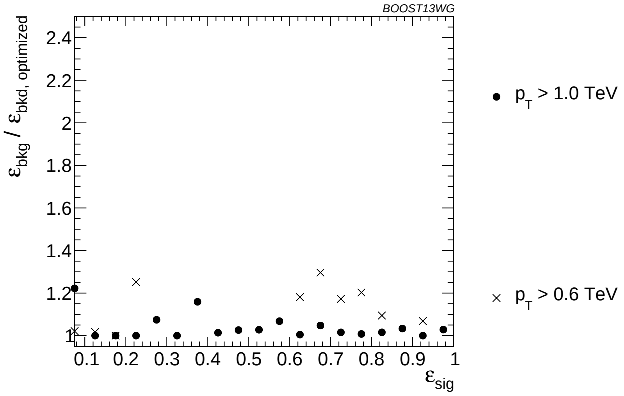

(a) HEPTopTagger m_t

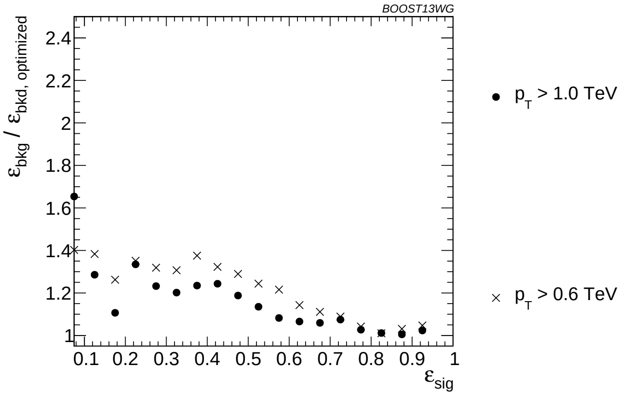

(b) Johns Hopkins Tagger m_t

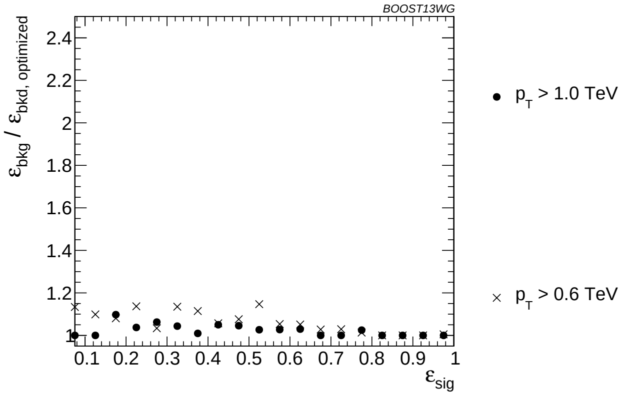

(c) Pruning m_t

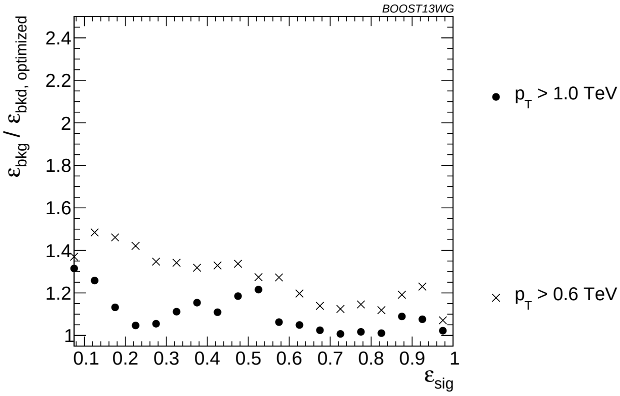

(d) Trimming m_t

Fig. 46 Comparison of top mass performance of different taggers at different p_T using the anti-k_{T} R=0.8 algorithm; the tagger inputs are set to the optimum value for $p_T = 1.5 - 1.6$ TeV.

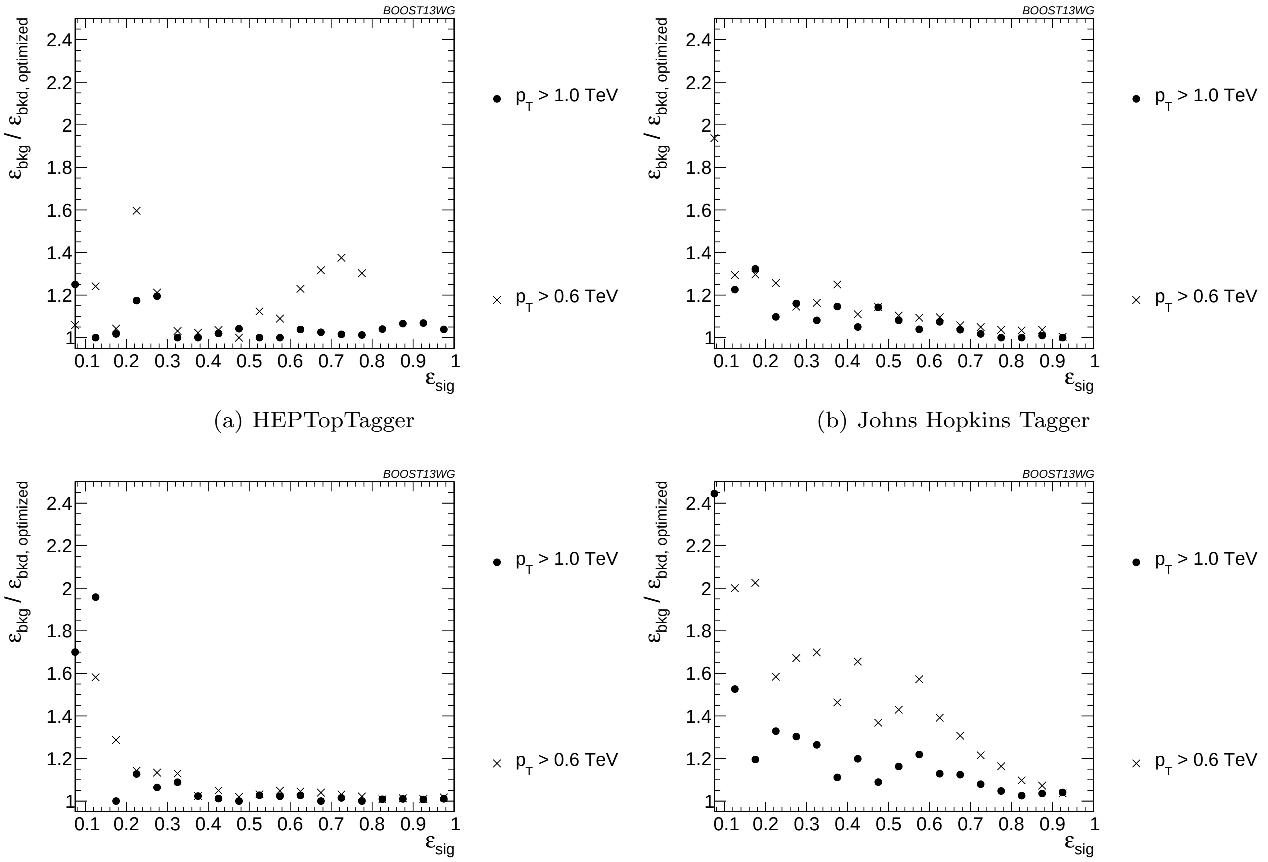

(a) HEPTopTagger

(b) Johns Hopkins Tagger

(c) Pruning

(d) Trimming

Fig. 47 Comparison of BDT combination of tagger performance at different p_T using the anti-k_{T} R=0.8 algorithm; the tagger inputs are set to the optimum value for $p_T = 1.5 - 1.6$ TeV.

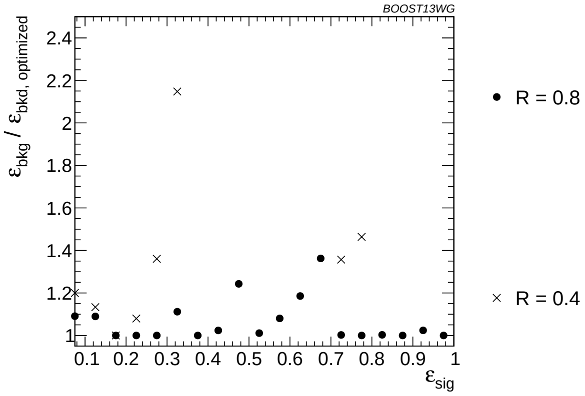

(a) HEPTopTagger m_t

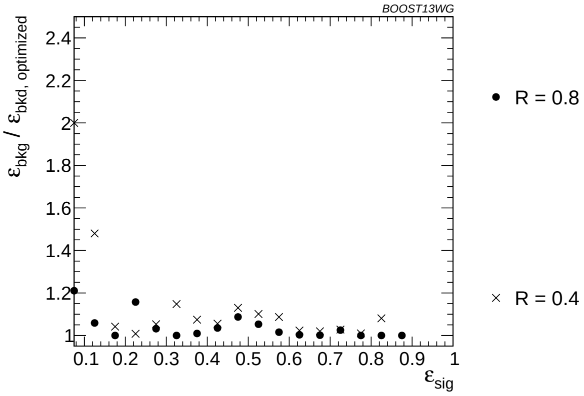

(b) Johns Hopkins Tagger m_t

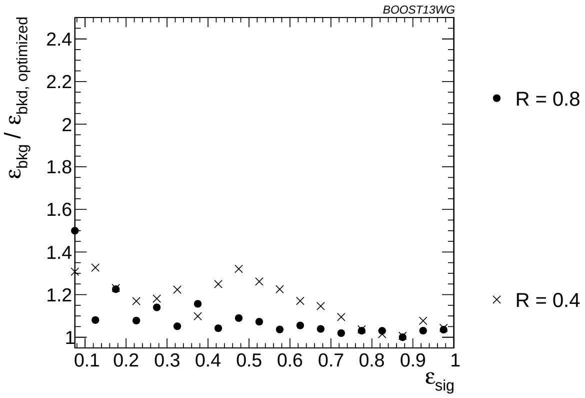

(c) Pruning m_t

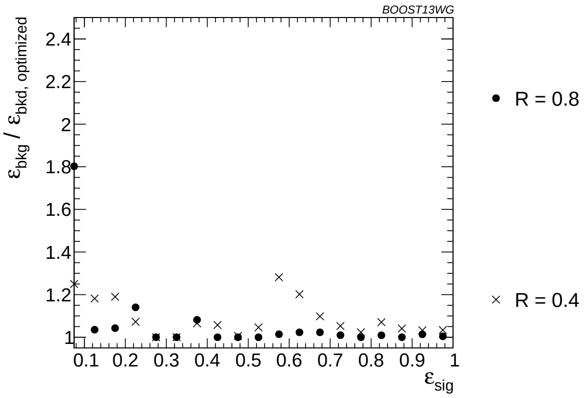

(d) Trimming m_t

Fig. 48 Comparison of top mass performance of different taggers at different R in the $p_T = 1500 - 1600$ GeV bin; the tagger inputs are set to the optimum value for $R = 1.2$.

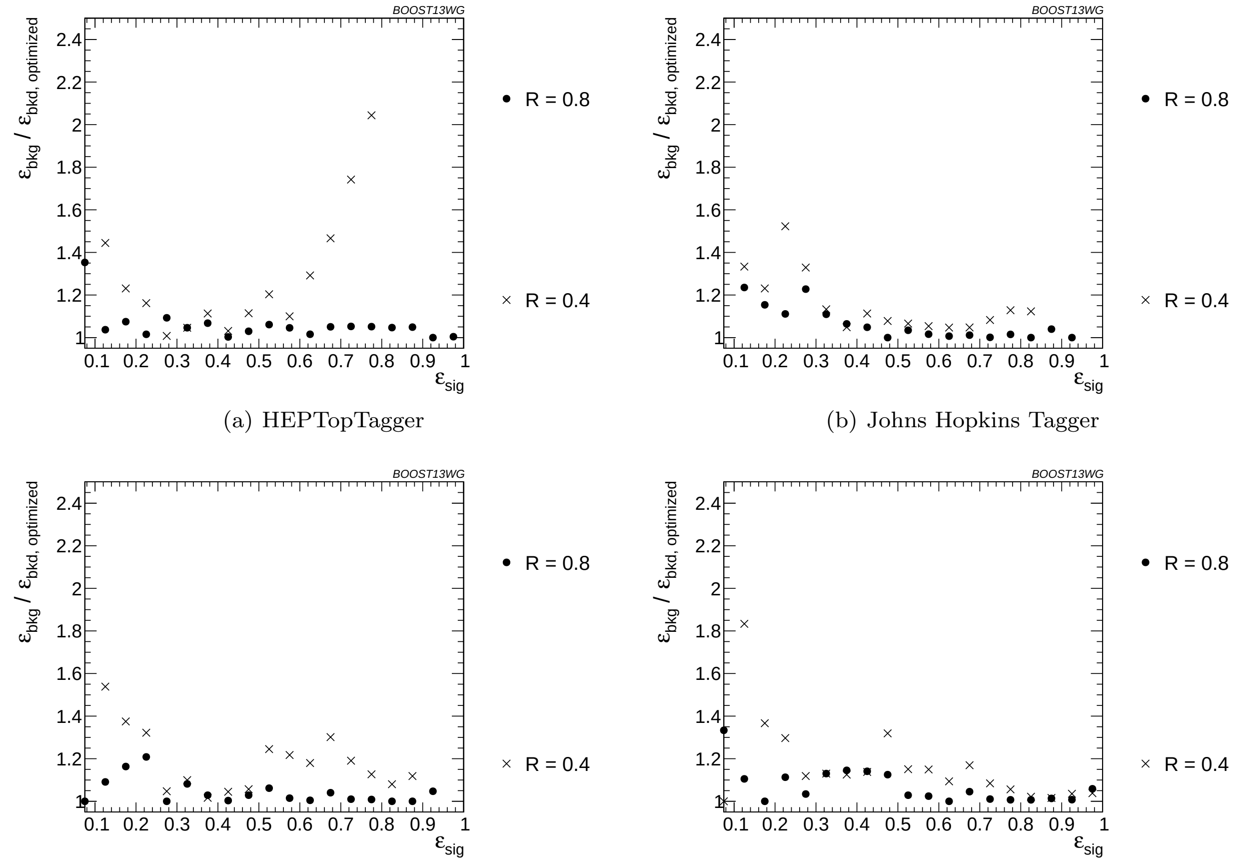

(a) HEPTopTagger (b) Johns Hopkins Tagger

(c) Trimming (d) Pruning

Fig. 49 Comparison of BDT combination of tagger performance at different radius at $p_T = 1.5$-1.6 TeV; the tagger inputs are set to the optimum value for $R = 1.2$.

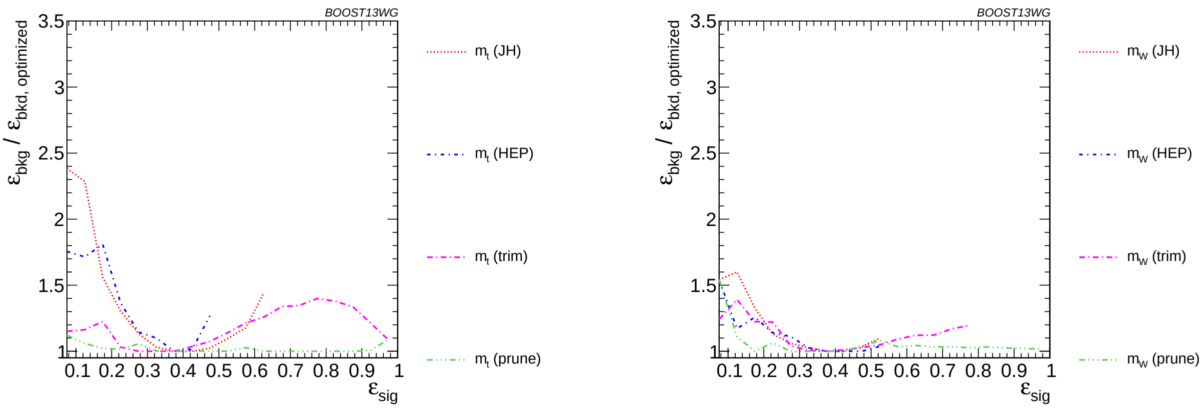

(a) Top mass (b) W mass

Fig. 50 Comparison of single-variable top-tagging performance in the $p_T = 1-1.1$ GeV bin using the anti-k_{T}, R=0.8 algorithm; the inputs for each tagger are optimized for the $\varepsilon_{\mathrm{sig}} = 0.3 - 0.35$ bin.

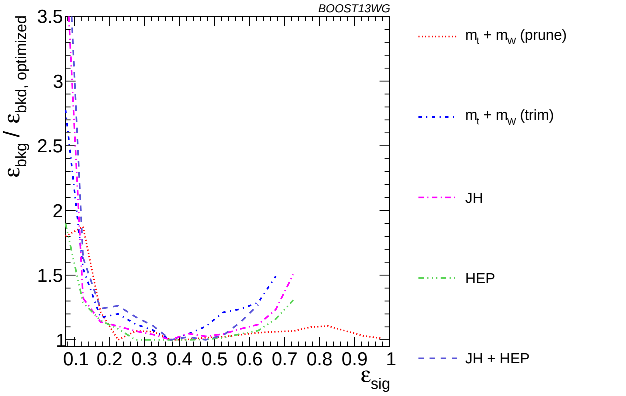

(a) Tagger-Groomer comparison

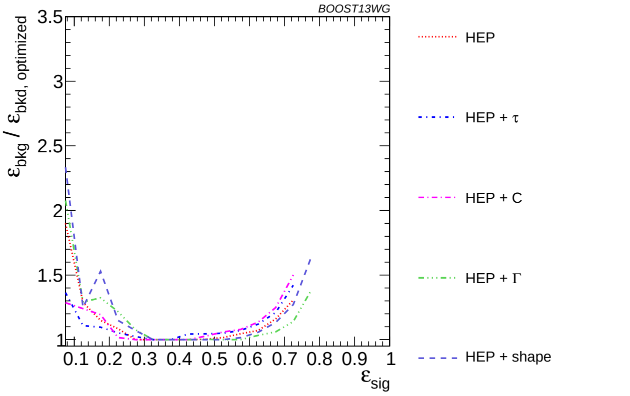

(b) HEPTopTagger + Shape

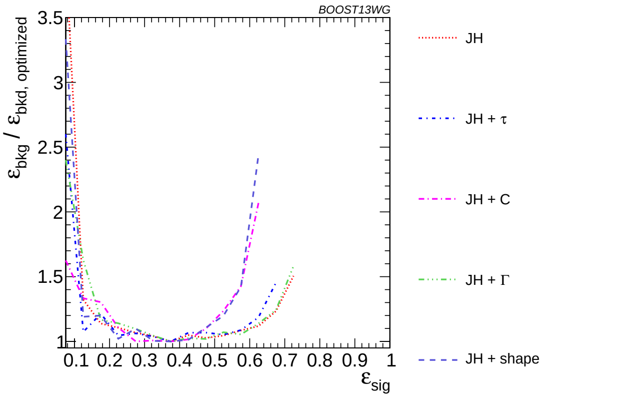

(c) Johns Hopkins Tagger + shape

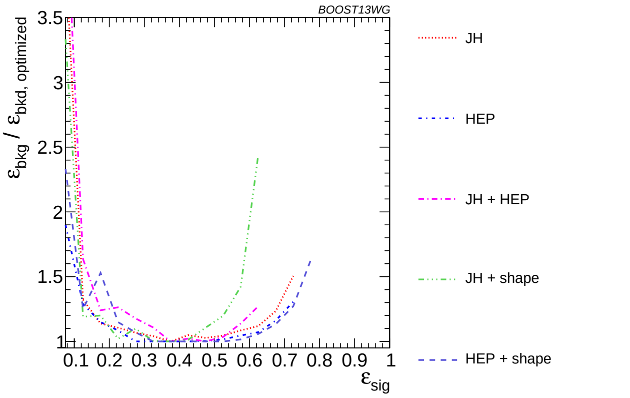

(d) HEP vs. JH comparison (incl. shape)

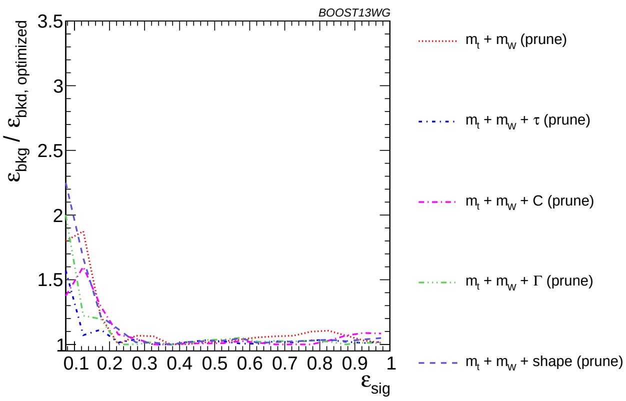

(e) Pruning + Shape

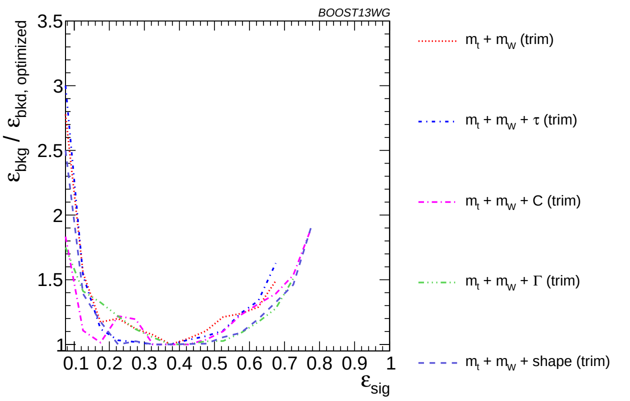

(f) Trimming + Shape

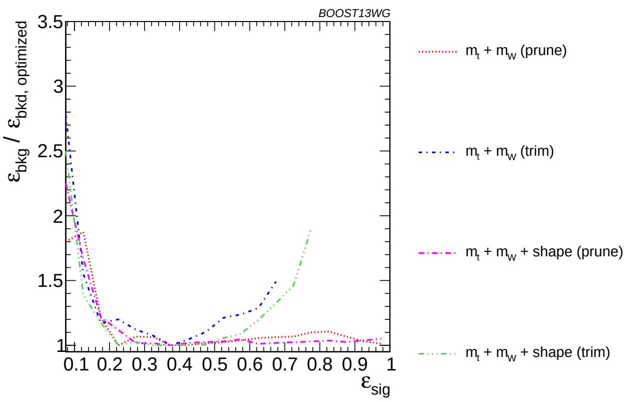

(g) Trim vs. Prune comparison (incl. shape)

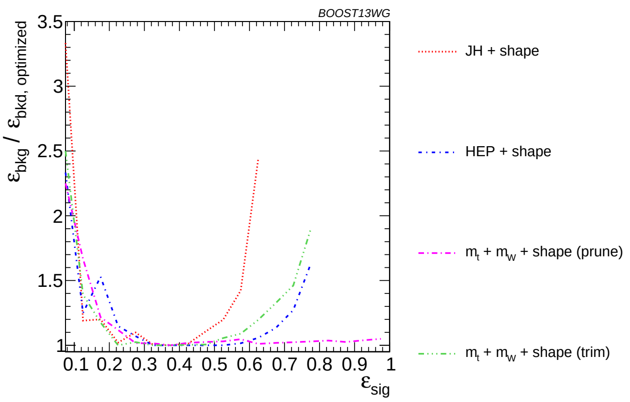

(h) Comparison of all Tagger+Shape

Fig. 51 The BDT combinations in the $p_T = 1 - 1.1$ TeV bin using the anti-k_{T} R=0.8 algorithm. Taggers are combined with the following shape observables: $\tau_{21}^{(\beta=1)} + \tau_{32}^{(\beta=1)}$, $C_2^{(\beta=1)} + C_3^{(\beta=1)}$, Γ_{Qjet}, and all of the above (denoted "shape"). The inputs for each tagger are optimized for the $\varepsilon_{\mathrm{sig}} = 0.3 - 0.35$ bin.

8 Summary & Conclusions

This report discussed the correlations between observables and looked forward to jet substructure at Run II of the LHC at 14 TeV center-of-mass collisions eneergies.

Acknowledgements

We thank the Department of Physics at the University of Arizona and for hosting the conference at the Little America Hotel. We also thank Harvard University for hosting the event samples used in this report. This work was made possible in part by the facilities of the Shared Hierarchical Academic Research Computing Network (SHARCNET) and Compute/Calcul Canada. We also thank Hallie Bolonkin for the BOOST2013 poster design and Jackson Boelts' ART465 class (fall 2012) at the University of Arizona School of Arts VisCom program. (NEED TO ASK PETER LOCH FOR MORE ACKNOWLEDGEMENTS)

References

1. A. Abdesselam, E. B. Kuutmann, U. Bitenc, G. Brooijmans, J. Butterworth, et al., *Boosted objects: A Probe of beyond the Standard Model physics*, *Eur.Phys.J.* **C71** (2011) 1661, [`arXiv:1012.5412`].
2. A. Altheimer, S. Arora, L. Asquith, G. Brooijmans, J. Butterworth, et al., *Jet Substructure at the Tevatron and LHC: New results, new tools, new benchmarks*, *J.Phys.* **G39** (2012) 063001, [`arXiv:1201.0008`].
3. A. Altheimer, A. Arce, L. Asquith, J. Backus Mayes, E. Bergeaas Kuutmann, et al., *Boosted objects and jet substructure at the LHC*, `arXiv:1311.2708`.
4. A. Hoecker, P. Speckmayer, J. Stelzer, J. Therhaag, E. von Toerne, and H. Voss, *TMVA: Toolkit for Multivariate Data Analysis*, *PoS* **ACAT** (2007) 040, [`physics/0703039`].
5. C. Anders, C. Bernaciak, G. Kasieczka, T. Plehn, and T. Schell, *Benchmarking an Even Better HEPTopTagger*, *Phys.Rev.* **D89** (2014) 074047, [`arXiv:1312.1504`].